UCRL-LR-138667

Cooling of Highly Charged Ions in a Penning Trap

Lukas Gruber

U.S. Department of Energy
Lawrence Livermore National Laboratory

March 31, 2000

DISCLAIMER

Work performed under the auspices of the U. S. Department of Energy by the University of California Lawrence Livermore National Laboratory under Contract W-7405-Eng-48.

UCRL-LR-138667
Distribution Category UC-71

Cooling of Highly Charged Ions in a Penning Trap

Lukas Gruber

Manuscript date: March 31, 2000

LAWRENCE LIVERMORE NATIONAL LABORATORY
University of California • Livermore, California • 94551

Cooling of Highly Charged Ions in a Penning Trap

Dissertation

Lukas Gruber

Technische Universität Graz

2000

The research to this work was performed entirely
under the auspices of the U.S. Dept. of Energy by University of California
Lawrence Livermore National Laboratory under contract #W-7405-ENG-48
and under the local supervision of

Dr. Dieter Schneider
Lawrence Livermore National Laboratory

and the academic supervision of

Prof. Dr. Helmut Jäger
Institut für Experimentalphysik
Technische Universität Graz, Austria

Hochgeladene Ionen werden aus einer Elektronenstrahlionenfalle extrahiert und zu Retrap, einer kalten Penningfalle gebracht, wo sie mit lasergekühlten Be^+ Ionen gemischt werden. Die Be^+ Ionen stellen ein Kältebad für die heißen hochgeladenen Ionen dar, deren Temperatur auf diese Weise in wenigen Sekunden um etwa acht Größenordnungen gesenkt wird. Diese kalten, hochgeladenen Ionen bilden ein stark gekoppeltes, nicht-neutrales Plasma, das unter diesen Bedingungen zu Coulomb Clustern und Kristallen kondensiert. Mit der richtigen Mischung an Ionensorten können derartige Plasmen als Analogon für die extrem dichten Plasmen in Weißen Zwergen gesehen werden. Solche Plasmen können möglicherweise auch zur Entwicklung von kalten Ionenstrahlen für Anwendungen in der Nanotechnologie beitragen. Bedingt durch die verschwindende kleine Dopplerverbreiterung bei solchen Temperaturen kann Laserspektroskopie mit bisher nicht gekannter Genauigkeit betrieben werden.

Die Dichte und die Temperatur der Be^+ Plasmen wuden gemessen und die hochgeladenen Ionen wurden erstmals *sympathetisch*, auf ähnliche Temperaturen gekühlt. Molekulardynamische Simulationen konnten die Aggregationsform, Temperatur und die Dichte der hochgeladenen Ionen bestätigen, wobei sich geordnete Strukturen in den Simulationen zeigten.

Fachgebiete: Atomphysik, Plasma, Kristall, Cluster, Optik;

Schlagwörter: Hochgeladene Ionen, Elektronenstrahlionenfalle, EBIT, Penning Falle, Retrap, dichtes Plasma, kaltes Plasma, stark gekoppeltes Plasma, nicht-neutrales Plasma, Coulomb Kristall, Coulomb Cluster, Ionenstrahlen, Laserkühlung, Laserinduzierte Fluoreszenz, Molekulardynamik-Computer-Simulationen, Weißer Zwerg, Phasenübergang, Ladungsaustausch, Xenon, Beryllium;

Highly charged ions are extracted from an electron beam ion trap and guided to Retrap, a cryogenic Penning trap, where they are merged with laser cooled Be^+ ions. The Be^+ ions act as a coolant for the hot highly charged ions and their temperature is dropped by about 8 orders of magnitude in a few seconds. Such cold highly charged ions form a strongly coupled nonneutral plasma exhibiting, under such conditions, the aggregation of clusters and crystals. Given the right mixture, these plasmas can be studied as analogues of high density plasmas like white dwarf interiors, and potentially can lead to the development of cold highly charged ion beams for applications in nanotechnology. Due to the virtually non existent Doppler broadening, spectroscopy on highly charged ions can be performed to an unprecedented precision.

The density and the temperature of the Be^+ plasma were measured and highly charged ions were sympathetically cooled to similar temperatures. Molecular dynamics simulations confirmed the shape, temperature and density of the highly charged ions. Ordered structures were observed in the simulations.

Subject(s): atomic physics, plasma, crystal, cluster, optics;

Keywords: highly charged ions, electron beam ion trap, EBIT, Penning trap, Retrap, dense plasma, cold plasma, strongly coupled plasma, non-neutral plasma, Coulomb crystal, Coulomb cluster, ion beam, laser cooling, laser induced fluorescence, molecular dynamics simulation, white dwarf, phase transition, charge exchange, xenon, beryllium;

Contents

List of Figures

List of Tables

1 Introduction

1.1 Historical Introduction

The physics of nonneutral plasmas has become part of many different areas in physics. The first experimental investigation was the effort of Frans Michel Penning in 1936 to realize a vacuum gauge [1]. He developed the basic field configuration used to confine charged particles with a single sign of charge. In World War II similar field configurations were used in magnetrons to produce high-frequency electro-magnetic waves for radar applications. Pursuing new techniques in atomic physics, Hans Dehmelt [2] and Wolfgang Paul refined single ion trapping techniques in the 1960's, for which they were awarded the Nobel Prize in 1989. At the same time, in the plasma physics community the publication of the monograph [3] of Ronald C. Davidson reflected the significance and the upcoming broader interest in a variety of different fields. He coined the expression 'nonneutral plasma'. Already in 1977 John Malmberg and O'Neil published their thoughts about the possibility of cooling a pure electron plasma so that it would crystallize [4]. The experimental work to the proposed crystallization was successful about a decade later. However, in 1980 W. Neuhauser [5] had most likely produced a ion crystal already, but it was not possible for them to image it. Joining the knowledge of atomic physics and plasma physics, Dave Wineland and collaborators began to trap and cool singly charged ions in Penning traps and demonstrated crystallization in 1987 [6]. At the same time a group of researchers at the Max Planck Institut für Quantenoptik in Garching, led by Herbert Walther demonstrated crystallization in a Paul trap [7].

Since then, several different groups around the world were able to demonstrate crystallization of singly charged nonneutral ion plasmas and the research on such plasmas diversified drastically [8]. Some of the research topics with nonneutral plasmas are fluid dynamics [9], transport mechanisms [10], mode excitation [11], particle beams [12], strongly coupled plasmas [13], and dusty plasmas [14, 15] and colloidal

suspensions [16], fusion research [17, 18] and production of antimatter [19, 20, 21].

1.2 Structure of Present Work

In the present work, the first attempt of capturing and cooling highly charged ions in a Penning trap was made. Ions of charge states up to Xe^{44+} were produced by an electron beam ion trap, extracted, recaptured in Retrap, a cryogenic Penning trap, and cooled to temperatures as low as a few K. Under these conditions the ion plasma in the trap – even for the lowest possible densities – is expected to crystallize. This crystallization is due to the mutual high Coulomb potential energy between the ions, offering possibilities to investigate phase transitions in such matter at higher temperatures than singly charged ions. An additional advantage of highly charged ions is that it is feasible to produce mixtures of different highly charged ion plasmas with matching mass to charge ratios. Such plasmas are one of the cleanest laboratory analogues of White Dwarf star interiors, and the investigation of phase transitions can provide, so far unaccessible, experimental data on such systems.

For atomic physics these cold plasmas are of interest since fine and hyperfine transitions in highly charged ions can potentially be measured to an unprecedented accuracy due to the virtually nonexistent Doppler broadening. And finally, nuclear physics can benefit from such research on highly charged ions. Some of the most accurate mass measurements are done in traps and binding energies can potentially be measured with such mass measurements.

The work presented here is concerned with showing the feasibility of such research on cold highly charged ion plasmas. A brief introduction of how an electron beam ion trap works and a more detailed description of the ion transport system and the Penning trap, Retrap, are given in Chapter (2). The laser system necessary for the chosen cooling scheme is described therein as well. Chapter (3) gives a brief overview of the significance of strongly coupled plasmas in nature and technology, as well as some useful theoretical background on such plasmas in Penning traps. Chapter (4)

is dedicated to possible cooling mechanisms and the chosen cooling scheme, and in the main Chapter (5) most of the measurement techniques and the acquired data are presented. It was possible to measure the density of the highly charged ions, but the temperature could only be measured for Be^+ ions, which were in the trap at the same time. This made some simulations necessary to estimate the temperature of the highly charged ions. Such molecular dynamics simulations and their results are presented in Chapter (6). These simulations give the necessary link to find an estimate for the highly charged ion temperature, which shows that the production of cold strongly coupled, highly charged ion plasmas in a Penning trap was achieved.

2 The EBIT-Retrap Facility

Since its conception and realization in 1986 [22] the electron beam ion trap (EBIT) has contributed as an essential tool to the study of highly charged ions in many ways [23]. The EBIT – a spin-off device from the electron beam ion source (EBIS) [24] – was originally developed for in-situ x-ray spectroscopy on low density, high temperature plasmas. The unprecedented ability of an EBIT to produce highest charge states [25] triggered the use of EBIT as an ion source. After the first extraction experiments in 1990 [26] the ion beamline was improved and now connects to a scattering chamber for surface physics studies and to Retrap, a cryogenic Penning trap [see Figure (2.1)]. In the 'surface chamber' ions extracted from EBIT are brought onto surfaces and ion-surface interaction processes are studied [27]. HCI show a very different interaction with surfaces than lower charge state ions due to the dominating potential energy compared to the kinetic energy. In Retrap specific ion species can be trapped and studied as the ions interact with each other, the residual gas and other injected ions, making a variety of interesting research possibilities viable:

- Ion-atom collisions with HCIs at low and ultra-low energies can be performed to study multi-electron transfer and recombination processes [28, 29, 30].

- Laser spectroscopy and fluorescence lifetime measurements can be performed with highest precision in cold plasmas on fine-structure transitions of multiply charged as well as on ground state hyperfine-structure transitions in high Z ions. The later allows one to deduce precision data for the g-factor of a bound electron.

- Precision mass spectroscopy (cyclotron resonance spectroscopy) can be used to perform measurements of binding energies, isotopic masses, and Lamb shift measurements in H-like high Z ions (e.g. U^{91+}).

- Condensed matter studies can be carried out with non-neutral strongly coupled

plasmas. Cooling of HCI to temperatures such that their kinetic energies are far less than their mutual electrostatic potential energies leads to the formation of crystalline structures (Coulomb crystals). This can be achieved with HCIs at much higher temperatures than for singly charged ions. Confinement of ionic mixtures allows for the study of the physics of crystallized binary plasmas which are of particular astrophysical interest to understand the aging of white dwarf stars.

- Schemes of coherent quantum control can be tested. Such schemes might be needed for applications in nanotechnology and might be beneficial to the development of quantum computers.

2.1 EBIT

A schematic of the LLNL EBIT II device[1] is shown in Figure (2.2). The electron beam originates in an electron gun at ground potential. The bucking coil counteracts the main magnet to cancel the magnetic field at the electron gun cathode in order to minimize the electron beam diameter in the high magnetic field. The beam is accelerated into the drift tubes by voltages up to 30 kV and compressed by a factor of $\approx$ 60 by the magnetic field[2] B (B = 3 T in the drift tubes) to a diameter of $d_{\mathrm{e-beam}} \approx 60$ μm. The path of the electrons terminates in a radial collector at a voltage of 1.5 kV. The magnetic field is substantially reduced at the collector, allowing the beam to expand and the electrons to be collected on the walls. The electron beam is collected with an efficiency of about 99.99 %: only about 20 μA out of 200 mA electron beam current are lost. A suppressor electrode between the drift tubes and collector prevent secondary electrons emitted in the collector from entering the drift tube region.

[1]For this work exclusively EBIT II was used. Therefore, the number II is omitted in the following.

[2]The correct denomination of this quantity is *magnetic induction*. However it is noted that frequently the term *magnetic field* is used as an equivalent.

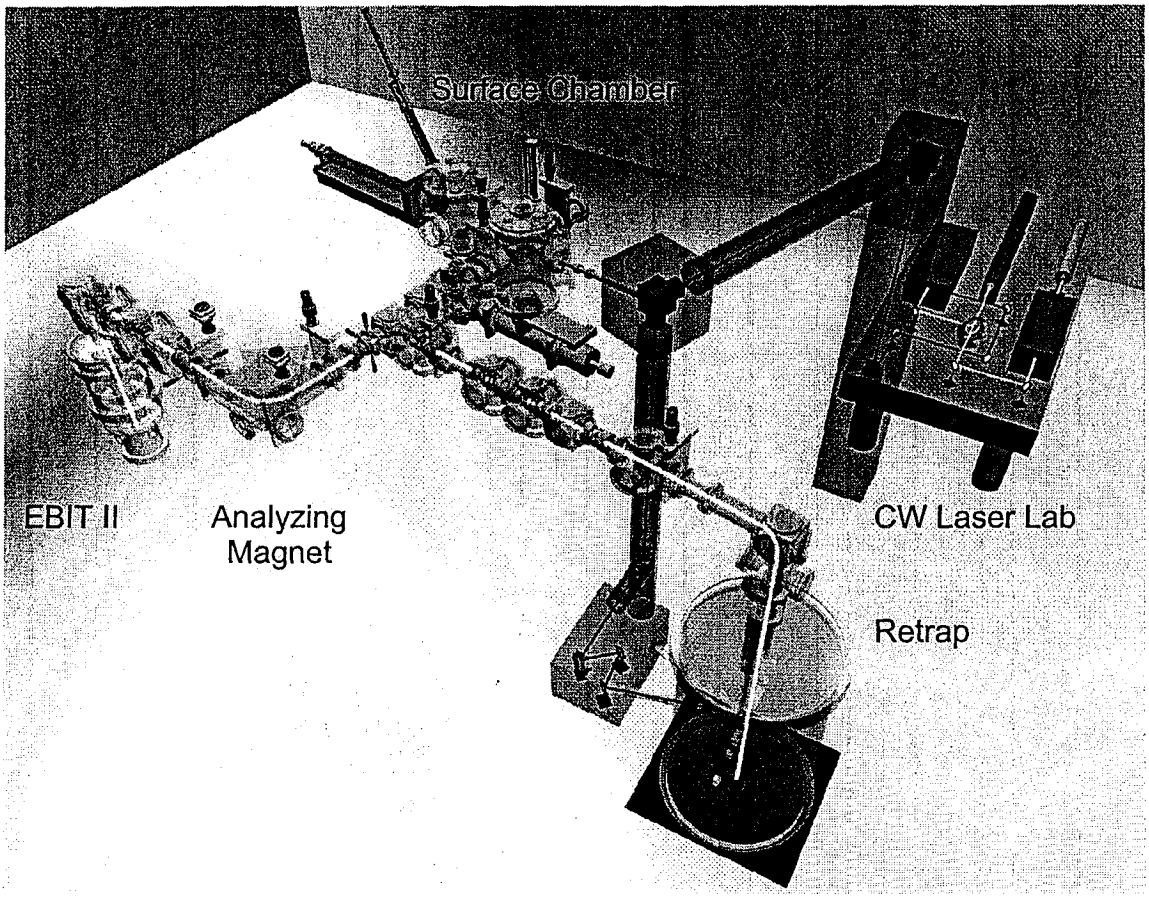

Figure 2.1: The EBIT facility. Shown are: EBIT II, the surface chamber, Retrap, the cw-laser laboratory and both ion- and laser beam line.

The voltages on the three drift tubes (bottom, middle and top drift tubes) are set to form an axial potential minimum in the center of the middle drift tube to confine positive charges. In the radial direction the confinement is given by the potential due to the space charge of the electron beam. The current density of the beam can reach values as high as 4000 A/cm^2. Ions confined in this region will be further ionized by sequential electron impact ionization. The highest achievable charge state depends on the beam energy. The abundance of a charge state depends on the ionization rates and the recombination rates with the beam and the residual gas [31].

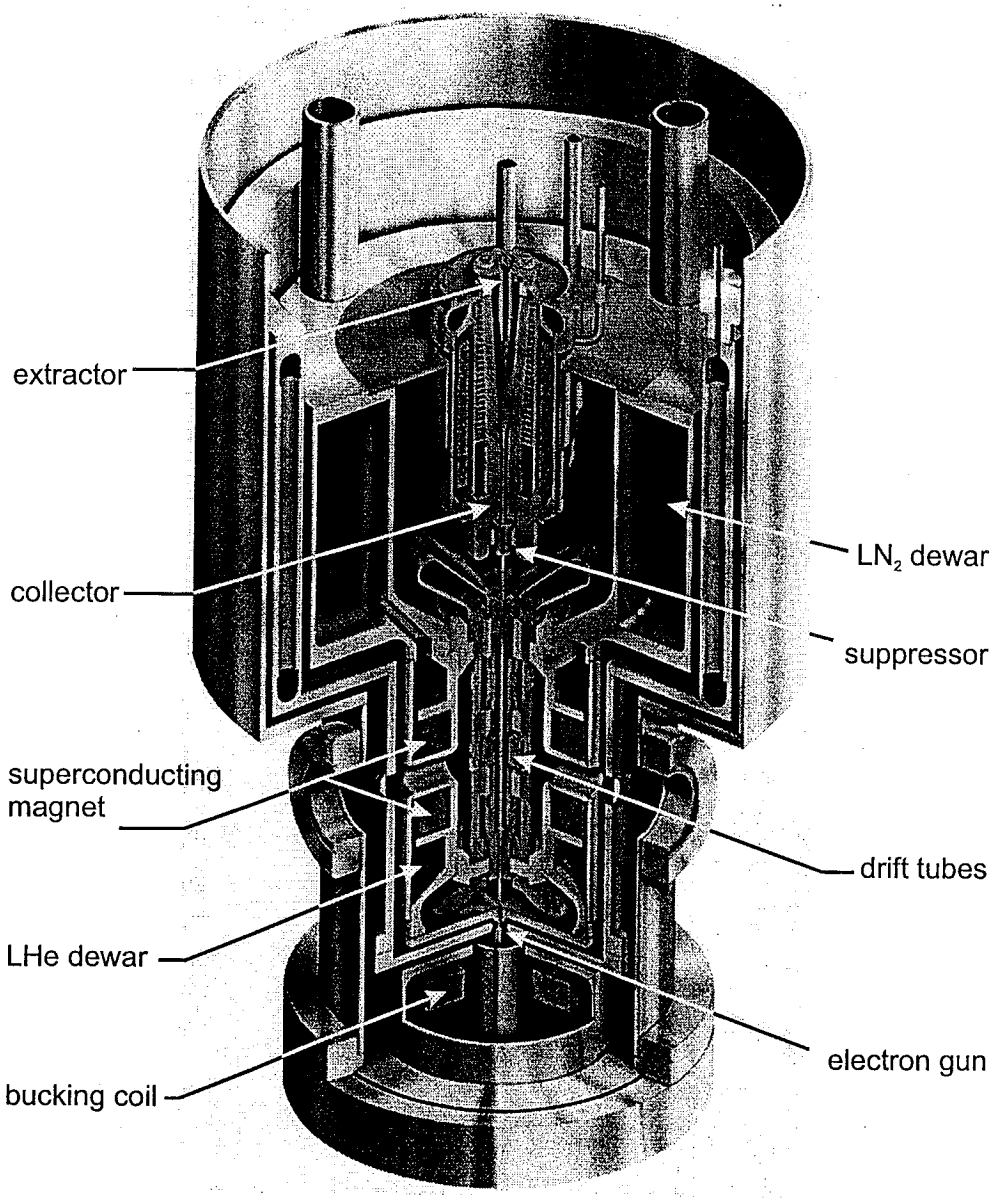

Figure 2.2: An cut out view of EBIT: The electron beam starts from the electron gun at ground potential on the bottom of the figure and is compressed by the superconducting Helmholtz coils as it is accelerated towards the drift tubes. The bucking coil cancels the magnetic field of the main coils at the electron gun in order to minimize the electron beam diameter. The maximum electron energy is 30 keV. Ions generated in the center of the drift tubes are confined axially by the drift tube potentials and radially by the space charge of the electron beam. The electron beam terminates in the collector and a positively biased suppressor inhibits secondary electrons from traveling back to the drift tubes.

2.1.1 Ion Injection

There are four different ways to introduce the desired element into an EBIT:

- through a gas injector,
- with a Metal Vapor Vacuum Arc (MEVVA),
- with a wire probe, and
- by accumulating ions originating from the electron gun.

The first two are the most commonly used methods. The gas injector is a differentially pumped vacuum system with two chambers separated by two small apertures from the main vacuum system of EBIT [31]. The apertures are lined up in such a way that they form a collimator for the gas molecules entering EBIT. Therefore, most of the molecules which make it through the apertures are ballistic and intersect the electron beam. The gas supply to the first chamber is regulated by a thermo-valve on a feedback circuit keeping the pressure in the chamber constant. The molecules entering the main vacuum chamber will intersect the electron beam and some of them will be ionized and therefore trapped. This method is a efficient method for elements in a gas phase. However the use of a gas injector can significantly deteriorate the vacuum in the main chamber since there is a high gas load causing a higher residual gas pressure which leads to a higher charge exchange rate therefore, making it more difficult to achieve high charge states.

The MEVVA injection method is applied if the desired ion is a metal[3]. The MEVVA itself consists of five electrodes, an anode, a cathode, a trigger electrode, a focus electrode and a ground casing [32, 33]. Either the trigger electrode or the cathode is made of the material which is to be injected. Between the anode and the cathode a voltage of 50 V - 450 V is applied and a high voltage spike is induced on the

[3]It is also possible to introduce solid others than metals with a MEVVA, but they need to be mixed with a metal to provide electrical conductivity.

trigger electrode to start a vacuum spark. This spark starts a discharge between the cathode and the anode, creating mostly singly and doubly charged ions, which are extracted from the MEVVA assembly by a biasing voltage of a few kV with respect to ground. These ions are decelerated as they enter EBIT by the biasing potential of the drift tubes and are then caught in the axial trap by switching the potential on the top drift tube to the middle drift tube potential for a brief instant (1 ms). Some of the ions are thereafter confined in the trap and further ionized by the impact of the energetic electron beam.

The wire probe method [34] is used if only a small amount of the desired element (e.g. rare isotopes or extremely dangerous materials) is available. The material is affixed to a tip of a needle and is brought through one of the side ports very close to the electron beam. Some electrons will sputter off atoms and the process of ionization can start. The fourth method is a method with a very restricted use since it only applies to materials originating in the electron gun cathode. It takes some time until the ions eventually get to the trap and are confined. Therefore, long ion production times ('cooking times') are necessary and this restricts the usage to rather heavy ions [see evaporative cooling in Chapter (4.1)]. Barium is the only element successfully and with sufficient amounts introduced in such a way into EBIT.

2.1.2 Cooling

Due to the impact of the electron beam the ions are heated at a rate which would cause them to be ejected from the trap on a timescale on the order of milliseconds. To prevent this, the ions need to be cooled. The evaporative cooling technique applied generally is to introduce a low Z cooling element into the trap, which if fully stripped would still have a lower charge state than the desired ion. Provided the different ion species are collisionally coupled, the temperature of both species will tend to be the same but the potential energy each species can have while still being confined, is proportional to the charge state. Therefore, the low Z-ions will be ejected from the

trap thereby reducing the energy content of the trapped mixture. In the experiments described in this paper Xe^{44+} was used as a highly charged ion (HCI). To cool Xe^{44+} it is not necessary to additionally introduce a low Z element. The residual gas consisting of C, N, and O is light enough to act as a cooling gas and is present in a large enough quantity (Xe^{44+} can assume a temperature 5.5 times as high as fully stripped O^{8+} and therefore, oxygen ions will constantly be ejected from the trap). Since the impact of the electron beam is the most prominent heat source in EBIT, the temperature can also be reduced by keeping the electron beam current as low as possible. However, there is a trade-off between produced number of ions and temperature.

2.1.3 Extraction

To extract the ions from EBIT the biasing potential of the drift tube assembly is brought to the desired extraction potential and the voltage on the middle drift tube is suddenly raised over the voltage of the top drift tube. To avoid the ejection of the ions towards the electron gun, the bottom drift tube potential is higher than the top drift tube potential. An extractor electrode [see Figure (2.2)] helps to guide the ions out of the magnetic field and an einzel lens focuses the beam into an electrostatic bender deflecting the ions path by 90° into the horizontal plane.

For this work EBIT is considered an ion source and to characterize a source the parameters emittance and brightness are of importance. To estimate these quantities for EBIT we take a closer look at the phase space of particles in a beam. According to Liouville's theorem the phase space volume stays constant for canonical transformations. A special case of a canonical transformation is the propagation of a charged particle beam in static electromagnetic fields. For an ion beam propagating in the z-direction, the six-dimensional phase space $\{x, y, z, p_x, p_y, p_z\}$ can be broken down into two two-dimensional spaces $\{x, p_x\}$ and $\{y, p_y\}$. If the beam occupies the volumes $S_x = \Delta x \cdot \Delta p_x$ and $S_y = \Delta y \cdot \Delta p_y$, then the beam emittance ϵ_i is defined by

normalizing these volumes to the momentum in the direction of propagation $p_{z,0}$:

$$\begin{aligned} \epsilon_x \equiv \frac{S_x}{p_{z,0}} &\equiv \Delta x \, \frac{\Delta p_x}{p_{z,0}} \text{ and} \\ \epsilon_y \equiv \frac{S_y}{p_{z,0}} &\equiv \Delta y \, \frac{\Delta p_y}{p_{z,0}} . \end{aligned} \tag{2.1}$$

If $\Delta p_x \ll p_{z,0}$ then $\frac{\Delta p_x}{p_{z,0}} = \tan(\alpha) \approx \alpha$, where α is the angle of the envelope of the beam with respect to the z-axis in the x-z-plane. The emittance is therefore a measure of beam divergence.

An estimate for the emittance of EBIT beams can be attempted by calculating S_y and S_x in the trap. Assuming a temperature of 500 eV for Xe^{44+} ions and a diameter of 60 μm for the ion volume in the trap, yields $S_x = S_y = 7.2 \cdot 10^{-25} \frac{\text{kgm}^2}{s}$. For an extraction voltage of 5000 V the longitudinal momentum becomes $p_{z,0} = 1.3 \cdot 10^{-19} \frac{\text{kgm}}{s}$. This yields an estimate for the emittance: $\epsilon_x = \epsilon_y = 1.8 \cdot \pi$ mm mrad. This coincides with the measured value of $\epsilon = 0.7 \cdot \pi$ mm mrad in [35], which was measured for Ar^{18+}.

The validity of Liouville's theorem breaks down if the particles in the beam interact with each other (i.e. space charge effects). Therefore, the estimate for the emittance might be systematically too low since the ions initially are affected by their space charge.

2.2 Beamline

EBIT is built vertically and the first electrostatic bender brings the beam into the horizontal part of the beamline [Figure (2.3)]. The ion beam transport line consists of 2 inch diameter electro-optical elements like einzel lenses, deflectors, electrostatic benders, and quadrupole lenses: these elements are shown in Figure (2.4). Retractable Faraday cups are used to optimize the beam transport throughout the system. An einzel lens has the ability to convert a divergent beam into a convergent beam just

like an optical lens. Typically the values of the potential on a lens in this system is anywhere from a few hundred volts to a few kilovolts. The deflectors consist of two tubes: the end of each tube facing the other is cut with an angle of 45°. If the two tubes are biased with the same voltage but different sign, charged particles passing through them are deflected. By placing two of these assemblies in series, one rotated 90° around the axis of the beam propagation, a complete steering element is realized. Electrostatic benders consist of a quarter of two concentric hollow cylinders. As in the case of the deflectors each cylinder is biased with the same voltage but opposite sign. If the outer cylinder is positive it will repel positive charges and the inner cylinder will attract them, causing the positive charge to be bent by 90°, given the potential is chosen corresponding to the particle's kinetic energy. Such benders have a focusing property in the bending direction [36]. In the direction perpendicular to that the beam is not affected at all. To compensate for this introduced astigmatism quadrupole lenses were installed after each bender. A quadrupole lens consists of four rods along the beam propagation direction. The two rods facing each other have the same potential and the rods 90° from those have also the opposite potential. This electrode configuration will spread the beam out in one direction and compress it in the other. By choosing the right potentials a beam converging in only one direction can be transformed into a collimated beam.

With these installed electro-optical elements, about 10^6 Xe^{44+} ions per second are brought from EBIT to Retrap in a continuous extraction mode. If the extraction is pulsed, about $3 \cdot 10^4$ ions are detected in a 5.5μs pulse.

All ion species follow the same exact trajectory, as long as they are extracted by the same potential. To make this clear we take a look at a particle's motion. The equation of motion for a particle with charge q and mass m in a static electric field $\vec{E}$ is given by

$$m \frac{\mathrm{d}^2\vec{r}}{\mathrm{d}t^2} = q\,\vec{E}. \tag{2.2}$$

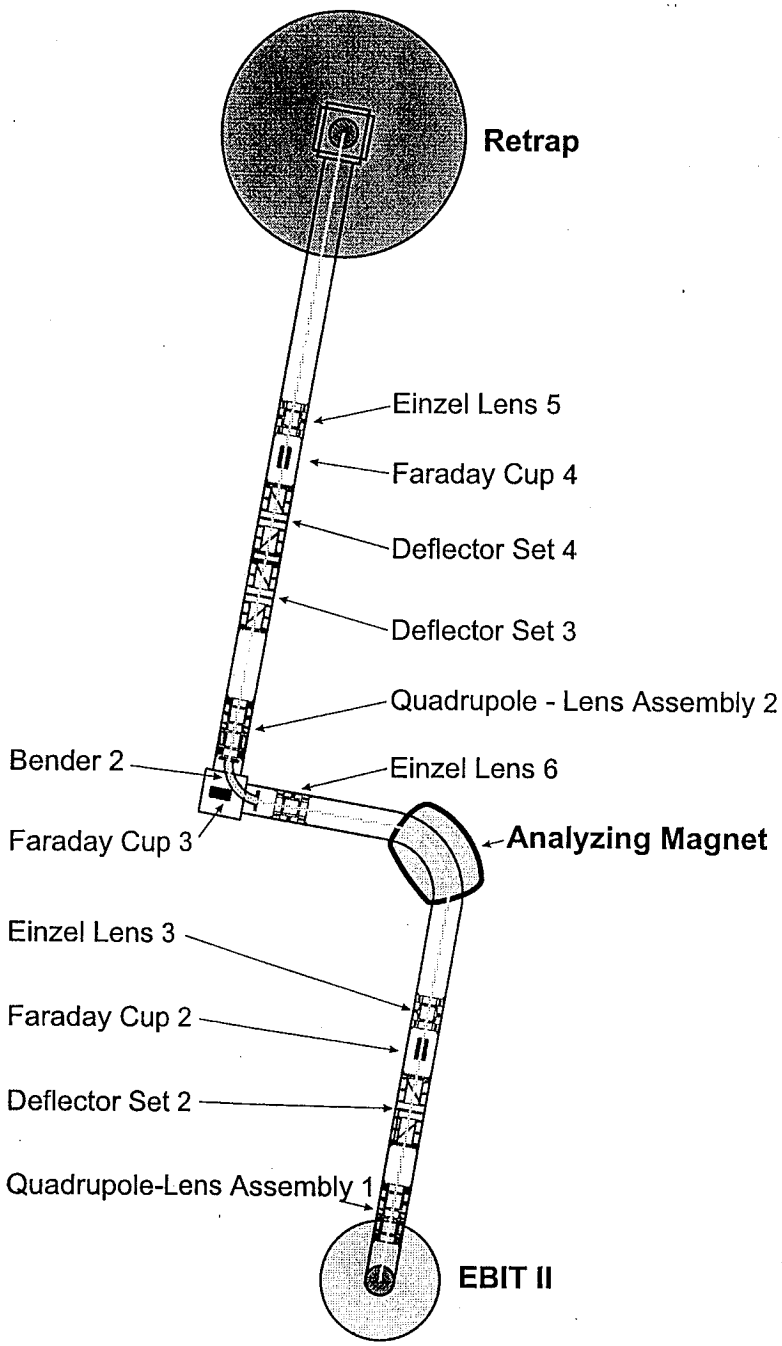

Figure 2.3: The horizontal part of the EBIT-Retrap ion beam line transports the ions from EBIT to Retrap. At EBIT the beam comes out of the paper plane and at Retrap it is bent back into it by electrostatic benders (not shown). The analyzing magnet allows a charge selection while the ion trajectories through all the other elements in the beamline are the same for all the ions as long as they are accelerated by the same potential.

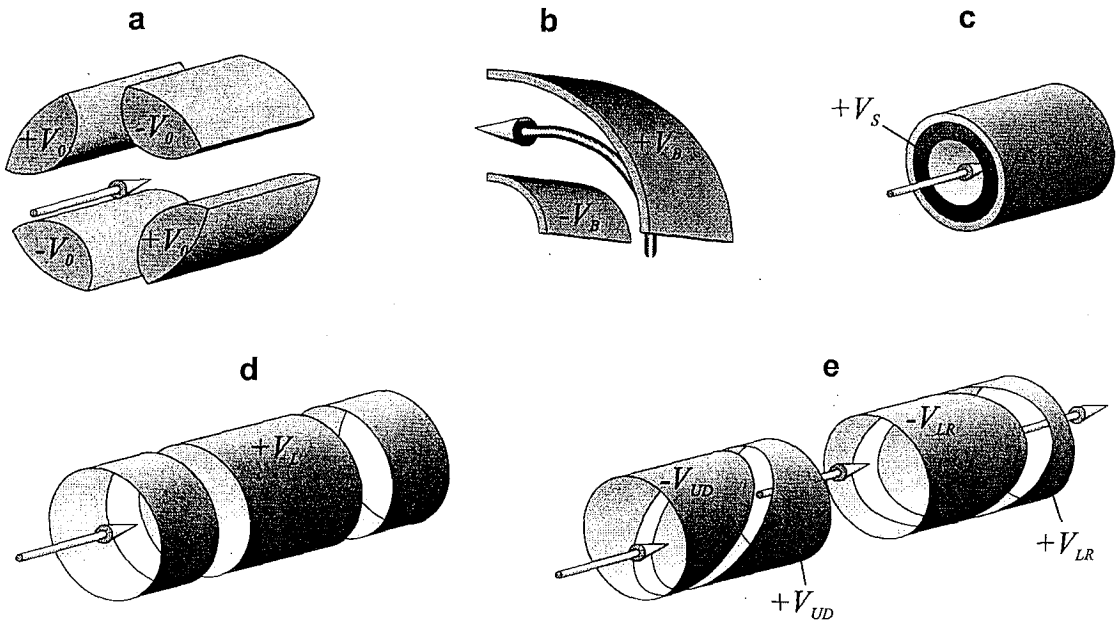

Figure 2.4: Beam line electro-optical elements. The beam is indicated with an arrow. a: A *quadrupole lens* compensates for the astigmatism introduced by the bending elements in the beam. For positive ions the positive electrodes are perpendicular to the bending direction. b: An *electrostatic bender* bends the trajectory of the beam by 90°. The larger of the two plates is sometimes made of a high transparency mesh to allow a different beam to pass straight through the bender while the benders electrodes are grounded. c: *Faraday cup*: the cup itself is used to detect the total collected charge of a beam pulse. In order to prevent secondary electrons from escaping the Faraday cup, a suppressing voltage V_S is applied to the suppressor ring. d: The outer electrodes of an *einzel lens* are typically grounded and the inner electrode is biased with a positive voltage V_L. e: The signs of the voltages V_{UD} and V_{LR} on the *deflectors* can be reversed, depending on the need to bend the beam.

If time t is substituted by

$$t' = t\left(\frac{q}{m}\right)^{\frac{1}{2}} \tag{2.3}$$

Equation (2.2) takes the following shape:

$$\frac{\mathrm{d}^2\vec{r}}{\mathrm{d}t'^2} = \vec{E}. \tag{2.4}$$

This new equation of motion is neither dependent on the mass nor the charge. Thus,

the solution $\vec{r}(t')$ is not dependent on these two variables either. All particles with an initial velocity proportional to $\left(\frac{q}{m}\right)^{\frac{1}{2}}$ [equivalent to the time transformation in Equation (2.3)] follow the same trajectory in space. A special case fulfilling the condition for the time transformation are particles accelerated from rest by the same extraction potential. This is the case in the EBIT extraction if the initial velocity spread is neglected.

Particles going through magnetic fields have generally different trajectories since the Lorentz force is proportional to the particle velocity. The analyzing magnet is the element in the beamline which sorts the particles by their mass to charge ratios. This can be derived by setting the centrifugal force equal to the Lorentz force for ions on a circular trajectory with radius R:

$$\frac{m\,v^2}{R} = q\,v\,B_A \tag{2.5}$$

(the magnetic field $\vec{B}_A$ is perpendicular to the particle velocity $\vec{v}$). The velocity of a particle accelerated by the extraction potential U is:

$$v = \sqrt{\frac{2\,q\,U}{m}}\,. \tag{2.6}$$

From Equations (2.5) and (2.6) we get

$$B_A = \frac{1}{R}\sqrt{2\,U\,\frac{m}{q}}\,. \tag{2.7}$$

For a fixed radius of curvature of the trajectory and extraction potential U, the magnetic field squared is proportional to the mass to charge ratio of the selected ion species. This fact is a helpful tool to interpret the spectra obtained by scanning the magnetic field and measuring the particle throughput of the magnet. An optical property of this 90° analyzing magnet is that it focuses the ion beam in the bending direction and it leaves the beam mostly undisturbed in the perpendicular direction. This introduces an astigmatism into the optics, which can be corrected with a quadrupole lens. Since bender 2, right after the analyzing magnet, introduces

more astigmatism in the same dimension, the correction of the beam is done after the bender. A last electrostatic bender, bender 3, steers the beam into the magnetic field of Retrap, where two einzel lenses, E6 and E8 [see Figure (5.1)] can be adjusted such that the trajectory of the beam coincides as closely as possible with the magnetic field lines. This assures the least conversion of axial kinetic energy into transversal cyclotron energy, keeping the beam as small in diameter as possible.

2.2.1 Ion Deceleration Process

Upon entering the strong magnetic field of Retrap, the ion bunch enters the deceleration tube, which is biased at approximately the extraction potential of EBIT. This slows the ions down to a few tens of volts times q of kinetic energy. Before the ions emerge from the tube, the voltage on the tube is switched rapidly to approximately ground. This prevents the ions from being reaccelerated, keeping their axial kinetic energy low. However, the transverse energy can be significantly higher, resulting in a cyclotron motion on large orbits if the ions trajectories cross the magnetic field lines at a large angle.

The concept of the adiabatic invariant of action angle variables provides a more general view of the injection process. This concept can be introduced by looking at the action integrals $J_i(p_i, q_i)$ of a mechanical system with the canonical momenta p_i and coordinates q_i:

$$J_i = \oint p_i \, \mathrm{d}q_i \; . \tag{2.8}$$

It can be shown that the action integral is constant not only for a mechanical system with static properties, but also to a good approximation for a system who's properties are changed slowly ('adiabatically') compared to the relevant periods of motion [37, 38]. Any quantity which is conserved in such slow processes is called 'adiabatic invariant'. In the case of a particle with charge q and mass m entering a magnetic field $B(z)$ it is the magnetic field which changes slowly with respect to the cyclotron motion of the particle. We look therefore at the transverse cyclotron motion of that

particle. The action integral is:

$$J = \oint \vec{P}_\perp \cdot \mathrm{d}\vec{l}\,, \tag{2.9}$$

where $\mathrm{d}\vec{l}$ is the line element along the cyclotron orbit and $\vec{P}_\perp$ is the transverse momentum of the particle. By using $\vec{P}_\perp = m\vec{v}_\perp + q\vec{A}$ Equation (2.9) can be rewritten as

$$J = \oint m\,\vec{v}_\perp \cdot \mathrm{d}\vec{l} + \oint q\,\vec{A} \cdot \mathrm{d}\vec{l}\,, \tag{2.10}$$

where $\vec{v}_\perp$ is the transverse velocity and $\vec{A}$ is the vector potential. The first integral can be simplified by using the fact that $\vec{v}_\perp$ and $\mathrm{d}\vec{l}$ are parallel and the second integral can be rewritten by applying Stokes's theorem and taking into account that $\vec{B}$ has the opposite direction of the vector $\mathrm{d}\vec{f}$ of the circular surface F:

$$J = m\,\omega_C\,r_C^2 \oint \mathrm{d}\varphi - q\,B \int_F \mathrm{d}f\,, \tag{2.11}$$

where ω_C is the cyclotron angular frequency and is defined in (2.27) and φ is the angle coordinate in a cylindrical coordinate system (r, φ, z). Equation (2.11) can be evaluated and yields:

$$J = r_C^2\,\pi\,B\,q = \text{const.} \tag{2.12}$$

This equation can be written in different ways, giving practical quantities, which are adiabatic invariants: The magnetic flux Φ included by the particle trajectory is constant:

$$\Phi = B\,r_C^2\,\pi = \text{const.} \tag{2.13}$$

The ratio of the transverse energy to the magnetic field is constant:

$$\frac{E_\perp}{B} = \text{const.} \tag{2.14}$$

And the magnetic moment μ of the current loop of the particle in orbit is constant as well:

$$\mu = \frac{1}{2}\,q\,\omega_C\,r_C^2 = \text{const.} \tag{2.15}$$

The condition for the validity of Equation (2.12) is that the rate with which the external field B changes needs to be small compared to the cyclotron angular frequency:

$$\frac{1}{B}\frac{\mathrm{d}B}{\mathrm{d}t} \ll \frac{\omega_C}{2\pi} . \tag{2.16}$$

The cyclotron angular frequency ω_C is now substituted by it's definition [Equation (2.27)], $\frac{\mathrm{d}B}{\mathrm{d}t}$ is substituted by $\frac{\partial B}{\partial z} \cdot \frac{\mathrm{d}z}{\mathrm{d}t} = \frac{\partial B}{\partial z} \cdot v_z$, and the velocity in the z-direction is expressed by the ion extraction potential U:

$$v_z = \sqrt{\frac{2\,q\,U}{m}} . \tag{2.17}$$

With Equation (2.17), Equation (2.16) becomes

$$2\,\pi\sqrt{\frac{m}{q}}\frac{\partial B}{\partial z}\frac{1}{B^2}\sqrt{2\,U} \ll 1 . \tag{2.18}$$

If the magnetic field as a function of z and the potential U are known, Equation (2.18) gives a useful relation to determine when the motion of the ion becomes adiabatic.

For Xe^{44+} the motion becomes adiabatic approximately 15 cm from the point where the magnetic field is the highest. The field at that point is 15% of the maximum value.

2.3 Retrap

Retrap is a cryogenic (the trap is at liquid He temperature of $\approx$ 4.2 K) Penning trap. The trap configuration used in the described experiments was a trap with hyperbolic electrodes as shown in Figure (2.5). A hyperbolic trap creates a quadratic electric potential along the z and r axis, while having a compact design. The magnet is a persistent magnet in a 50 l liquid helium dewar and is able to produce a field of up to 6 T inside its 3" diameter bore. Between the helium dewar and the 100 l liquid nitrogen dewar as well as between the nitrogen dewar and the main vacuum chamber there are passive heat shields to prevent radiative heat loss [see Figure (5.1)]. The pressure is about $7{\cdot}10^{-10}$ mbar close to the warm surface of the vacuum vessel and is considerably better within the trap due to cryogenic pumping.

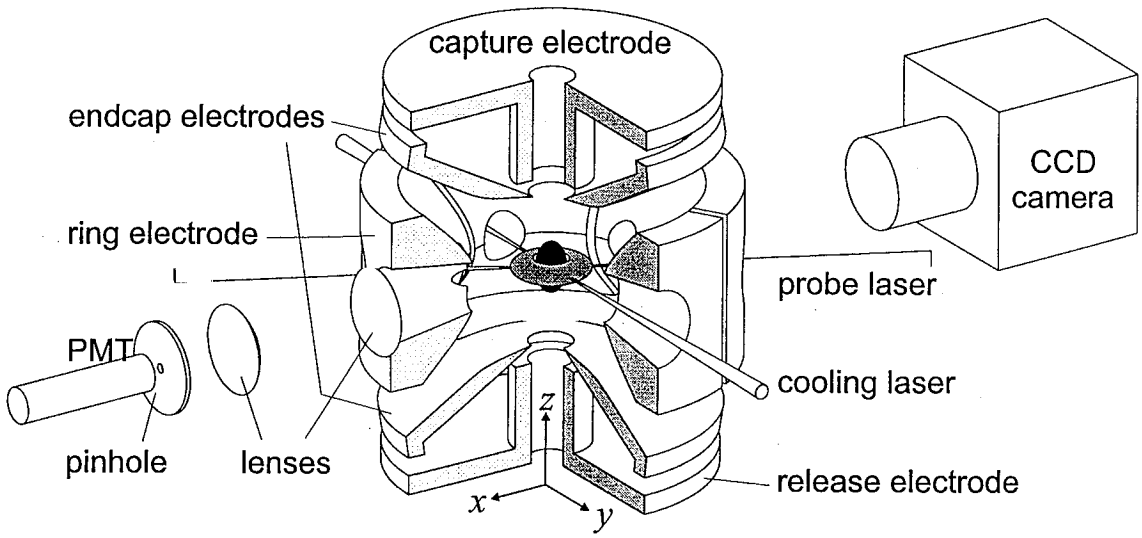

Figure 2.5: The hyperbolic trap configuration provides an electric quadrupole potential and allows for a compact design. In addition to the trap, two laser beams, a CCD camera and a photomultiplier tube with imaging optics are shown. In the center of the trap a schematic cloud of two different species is drawn (sizes of the clouds are not to scale). The top electrode is the catch electrode and the bottom is the release electrode. The ring electrode is split into four sectors enabling the cyclotron excitation of the ions.

2.3.1 Ion Capture

The ions enter the trap with low kinetic energies after they have been slowed down by the deceleration tube and are reflected by a potential of a few hundred volts on the release electrode. Before the ions leave the volume of the trap, the potential on the capture electrode is raised to the confining potential, thereby trapping the ions axially between the two electrodes. The radial confinement is provided by the magnetic field and is discussed in Chapter (2.3.2). The other electrodes [ring, compensation and endcap electrodes; see Figure (2.6)] are at ground potential. However, for certain purposes (e.g. time of flight measurements) it is advantageous to bias the whole trap assembly with a higher potential.

2.3.2 Ion Confinement

Once the ions are confined between the capture and the release electrodes a voltage difference V_0 between the ring electrode and the endcap electrode is applied. This potential difference together with the magnetic field determines the ion motion in the trap. The electric quadrupole potential $\phi_T(x, y, z)$ inside the trap is given by:

$$\phi_T(x, y, z) = V_0 \frac{2\,z^2 - x^2 - y^2}{d_0^2} \tag{2.19}$$

where d_0 is a geometrical trap parameter given by

$$d_0^2 = 2\,z_0^2 + \rho_0^2 = 2 \cdot [5.17(3)\text{mm}]^2 + [5.82(3)\text{mm}]^2 = [9.34(10)\text{mm}]^2, \tag{2.20}$$

In Equation (2.20) z_0 is the half length of the trap and ρ_0 is the radius [see Figure (2.6)]. Ideally the ring electrode and the endcap electrodes are infinite hyperboloids of revolution. In reality the electrodes need to be truncated at a finite size, introducing small imperfections which can be minimized with compensation electrodes [39].

The motion of a particle with charge q and mass m is determined by the electric and magnetic fields inside the trap. The Lagrange function for such a system is given by:

$$L = \frac{1}{2}\,m\,\dot{\vec{r}}^{\,2} + \dot{\vec{r}}\,\vec{A} - q\,\phi_T(\vec{r})\,. \tag{2.21}$$

The constant magnetic field points in the z-direction, $\vec{B} = (0, 0, B)$, and the vector potential can be chosen to be $\vec{A} = \frac{1}{2}\,\vec{B} \times \vec{r}$. Substituting this into Equation (2.21) yields:

$$L = \frac{1}{2}\,m\left(\dot{x}^2 + \dot{y}^2 + \dot{z}^2\right) + \frac{1}{2}\,q\,B\,(x\,\dot{y} - y\,\dot{x}) - q\,\phi(x, y, z). \tag{2.22}$$

With the Lagrange equation

$$\frac{\mathrm{d}}{\mathrm{d}t}\frac{\partial\,L}{\partial\dot{q}_k} - \frac{\partial\,L}{\partial q_k} = 0\,, \tag{2.23}$$

where q_k and $\dot{q}_k$ are the Cartesian coordinates and velocities, respectively ($k = x, y, z$) and Equation (2.22) the following coupled differential equations are obtained:

$$\ddot{x} - \omega_C\,\dot{y} - \frac{1}{2}\,\omega_z^2\,x \;=\; 0 \qquad . \tag{2.24}$$

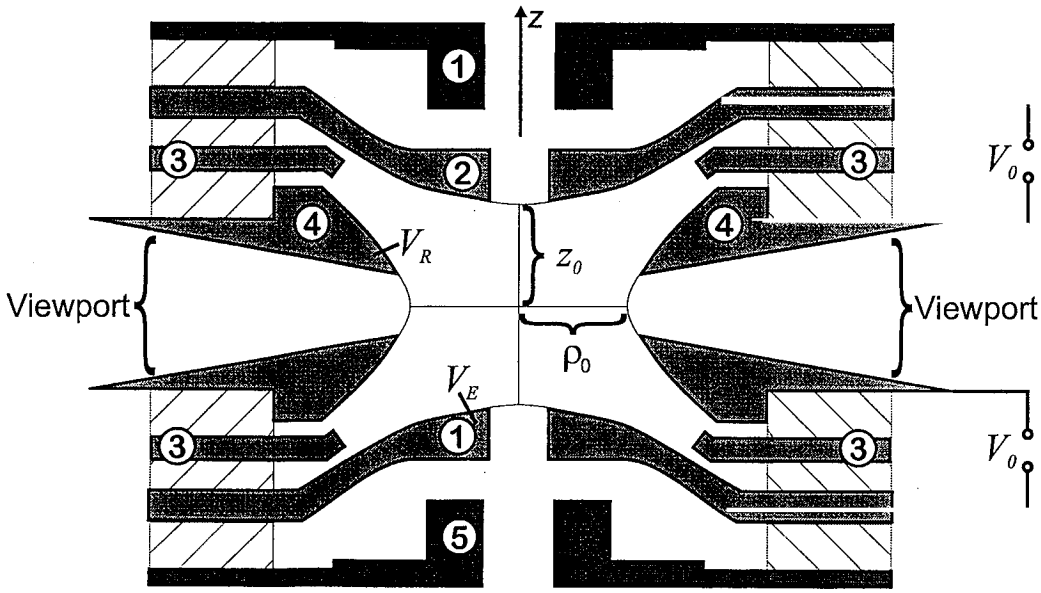

Figure 2.6: Cross-section of the hyperbolic trap. The trap has rotational symmetry about the z-axis (only the view-ports in the ring electrode (4) are not cylindrically symmetric). The endcap electrodes (2) are at a potential V_E and the ring electrode is at V_R. Compensation electrodes (3) were installed to minimize field imperfections due to the finite size of the endcap and ring electrodes. The capture (1) and release electrodes (5) are for ion capture and release, respectively.

$$\ddot{y} + \omega_C \dot{x} - \frac{1}{2}\omega_z^2 y = 0 \tag{2.25}$$

$$\ddot{z} - \omega_z^2 z = 0 \tag{2.26}$$

with

$$\omega_C = \frac{q\,B}{m} \tag{2.27}$$

and

$$\omega_z = \sqrt{\frac{4\,q\,V_0}{m\,d_0^2}}\,. \tag{2.28}$$

The solution for Equation (2.26) is a harmonic oscillation in the z-direction with the angular frequency ω_z, often called the axial angular frequency. Equations (2.24) and (2.25) describe two independent oscillations with angular frequencies

$$\omega_\pm = \frac{\omega_C}{2} \pm \sqrt{\left(\frac{\omega_C}{2}\right)^2 - \frac{\omega_z^2}{2}}\,. \tag{2.29}$$

Therefore, the motion of a single ion in a Penning trap is described by three independent harmonic oscillations: the axial oscillation with the angular frequency ω_z, a fast oscillation in the x-y-plane with the modified cyclotron angular frequency ω_+ and a slow oscillation in the x-y-plane due to the $\vec{E} \times \vec{B}$ drift with magnetron angular frequency ω_-. Note that these solutions are only valid for a single particle in the trap, neglecting its image charge on the walls of the trap. This is a good approximation if the trap dimensions are much bigger than the orbits of the particle. If more particles are in the trap, the space charge created by the trapped particles modifies the electric potential and has to be taken into account. This will be discussed in Chapter (3.3.3).

Equation (2.29) provides a possibility to estimate the mass to charge ratio particles can have and still be trapped. The term in the square root needs to be positive in order to describe an oscillation. With this condition the mass to charge ratio for trapped ions can be derived:

$$\frac{m}{q} \leq \frac{B^2 d_0^2 e}{8 V_0 m_p} \approx 80 \,, \tag{2.30}$$

where m_p is the proton mass, e is the electron charge and the last part of Equation (2.30) was obtained by setting $B = 6$ T and $V_0 = 500$ V. This condition holds for many trapped ions as well.

2.3.3 Ion Detection

For ion detection both destructive and nondestructive techniques have been applied. Destructive techniques destroy the cloud and a new cloud needs to be loaded to repeat the measurement. Nondestructive techniques do not destroy the cloud and it is possible to use the same ions for repeated measurements. The nondestructive techniques used are

- pick-up of induced electronic signals generated by the motion of the ions,
- weak excitation of resonant motions and pick-up of the generated electronic signals, and

- laser scattering techniques.

All destructive techniques required ion ejection from the trap. Then different detectors were used for counting and imaging these ions:

- electron multiplier tube (EMT) or micro-channel plate (MCP) in counting mode, allows for time of flight measurements
- image intensifier (MCP with phosphor screen) for visualizing the cloud shape
- Faraday cup or a simple metallic plate like the front electrode of an EMT or MCP ('Faraday mode' of EMT or MCP) for current measurement
- UHV-compatible cryogenically cooled, charge coupled device (CCD) camera, making the detection of the position of each ion feasible. The CCD integrates all impacts over time in contrast to the MCP with phosphor screen, where single impacts still can be counted. However the CCD has the better spatial resolution.

2.3.3.1 Passive Tuned Circuit Noise Detection One nondestructive technique is to measure the current flowing back and forth between the two endcap electrodes due to the axial center of mass motion of the ions. To detect this motion the endcap electrodes are connected by an inductor [see Figure (2.8)]. These elements form a LRC-circuit. With some diligence the resonance of the circuit can be made narrow and the dimensionless quality factor

$$Q = \frac{R}{\omega_{z,0} L} \tag{2.31}$$

of the circuit becomes large. R is the Ohmic resistance, L is the inductance of the coil and $\omega_{z,0}$ is the angular frequency at resonance. In Retrap Q was measured to be typically ≈ 550. The motion in the z-direction of a trapped ion can be modeled as an ion moving between two plates of a capacitor of distance $2\,z_0$ with the velocity v_z

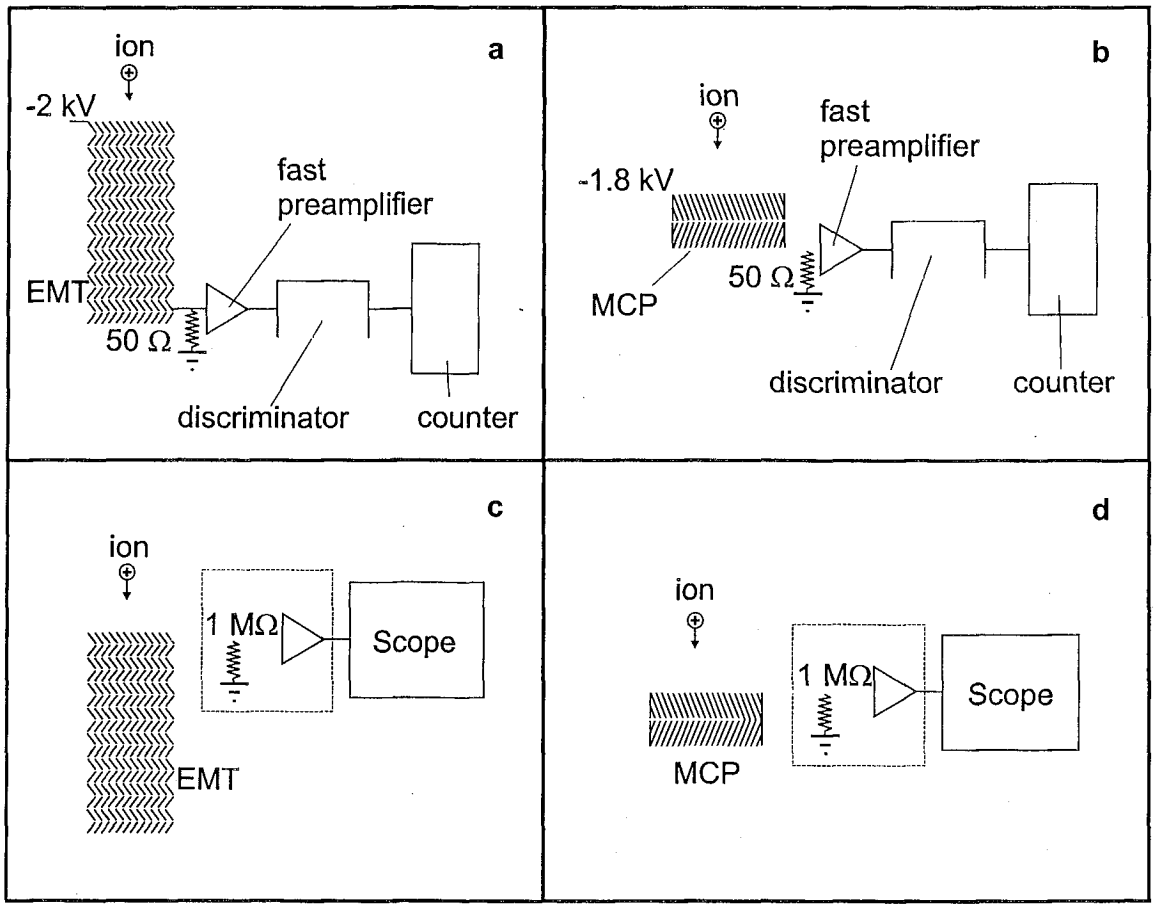

Figure 2.7: Different detector modes. a: The electron multiplier (EMT) in counting mode. An ion impact is amplified and creates a current pulse, which can be counted. b: The micro channel plate (MCP) in the counting mode. c: The EMT in the Faraday mode, where the incoming charge is collected on the first plate and discharged over the 1 MΩ input resistor of the amplifier. If the ion pulse is big, the amplifier can be omitted and the input resistor of the scope can be used to discharge the front plate of the detector. d: The MCP in the Faraday mode. The setup is the same as with the EMT.

[39]. This causes a current I to flow through the resistor R, giving rise to a voltage drop across the resistor of IR and causes an electric force f at the particle position of

$$f = -q\frac{\beta I R}{2 z_0} \tag{2.32}$$

opposing its motion (if the endcap electrodes were infinitely large plains and the ring were missing the constant β would equal unity; here: $\beta \approx 0.8$). The axial kinetic energy of the charged particle is therefore decreasing at the rate $v_z f$ which is dissipated in the resistor:

$$-v_z f = I^2 R. \tag{2.33}$$

With the Equations.(2.32) and (2.33) the current can be given:

$$I = \frac{\beta q v_z}{2 z_0}. \tag{2.34}$$

Thus, the power P_{ion} dissipated in the resistor can be expressed as:

$$P_{ion} = \frac{\omega_z L Q \beta^2}{2 z_0^2} \frac{q^2}{m} E_{kin,ion}\ , \tag{2.35}$$

by using Equation (2.31) and introducing the axial kinetic energy $E_{kin,ion} = \frac{m v_z^2}{2}$ of a particle. If N ions are trapped Equation (2.35) needs to be summed over all particles. Writing the total energy in terms of the average axial kinetic energy and calling the dissipated power the signal S_{TC} of the tuned circuit, yields:

$$S_{TC} = \frac{\omega_z L Q \beta^2}{2 z_0^2} \frac{q^2}{m} N \langle E_{kin} \rangle . \tag{2.36}$$

From Equation (2.36) it can be seen that the detected signal on the tuned circuit is proportional to the average kinetic energy of the ions and therefore, their temperature T, the total number N of the ions on resonance with the tuned circuit and the ratio of the charge state q^2 to the mass m of the ions:

$$S \propto \frac{q^2}{m} N T . \tag{2.37}$$

This is an important relation to keep in mind since the interpretation of the tuned circuit noise signal can often be misleading: i.e. an increase in signal can mean an increase in number or an increase in temperature.

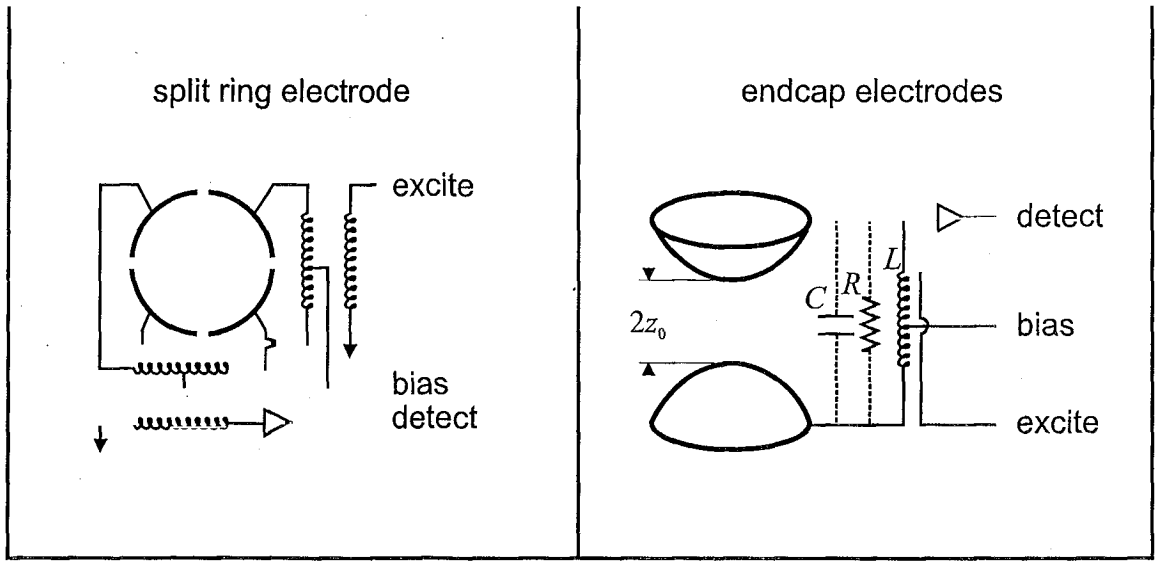

Figure 2.8: Electronic excitation and detection circuits for trapped ions. The ring electrode is displayed as a top view and the endcap electrodes as a side view. The dashed lines indicate how the electric circuit can be modeled. The detected signal is amplified with an amplifier at cryogenic temperatures.

2.3.3.2 Active Tuned Circuit Noise Detection The same basic relations as discussed above are valid for the active detection of particles in the trap. Just the experimental technique is different: a rf voltage at the resonance frequency of the tuned circuit is applied to the endcap electrodes while the axial potential well is changed. If the axial oscillation frequency of an ion matches the resonance frequency of the tuned circuit, the ion will absorb some power of the excitation. If the excitation power is monitored carefully, dips in the voltage scan will indicate the ion content.

2.3.3.3 Current Measurement of Released Ions This destructive technique is mostly used to measure the beam current of the main extracted beam from EBIT. However, if enough ions are trapped it could be used to detect ions released from Retrap as well.

The detector can be any metallic plate. Three different detectors were used here: A Faraday cup, a MCP, and an EMT. The detector setup is shown in Figure (2.7). Only

the front electrodes of the MCP and the EMT are used to collect all the charge hitting the detector. Due to secondary electron emission with each ion impact, the collected charge is amplified unless the electrode is biased properly to prevent electrons from escaping. The collecting electrode has a capacitance C discharged by the resistor R with a time constant of $\tau = R \cdot C$. The collected charge is given by:

$$\begin{aligned} Q &= U_C C \\ &= U_C \frac{\tau}{R}, \end{aligned} \tag{2.38}$$

where U_C is the voltage on the capacitance. To calculate the detected charge Equation (2.38) is used since it is easier to measure τ and R than to measure C.

2.3.3.4 Counting of Released Ions For low beam currents the EMT and the MCP are used in counting mode. The front electrode is biased at a negative voltage and the back electrode is connected to the input of a fast amplifier. If an ion hits the front plate, secondary electrons are emitted and amplified by the dynodes in the EMT and the channels in the MCP. On the back electrode a current pulse can be detected for each[4] ion impact, which is discriminated, amplified and connected to a counter. The time resolution for this counting technique is given by the dead time of the detectors, which is typically in the order of 5 ns. Therefore, a flux of about $2 \cdot 10^8$ particles per second starts to saturate the detector.

2.3.3.5 Imaging of Released Ions A MCP or a CCD provide for spatial resolution. Both detectors have different advantages and disadvantages.

A MCP needs a imaging device after the back electrode, like a 'wedge and strip' electrode or a phosphor screen. It is sensitive enough to detect singly and multiply charged ions. The CCD measures the location of the impact inherently. However,

[4]The term 'each' is used to indicate that it is possible to count single ions. However the detector has an efficiency of about 20%–80%, depending on the detected ion species. For high rates ion impacts within the dead time of the detector become more likely and the detection efficiency drops.

it's detection efficiency for singly charged ions is very low. It was found, that the CCD detects ions only if the kinetic energy is above a few keV·q. The CCD is useful to monitor the main beam from EBIT while the MCP can image the trap content. However, it is not possible to differentiate between the different species, which is important for the detection of HCIs in a multiple component plasma cloud.

2.3.3.6 Ion Detection by Laser Induced Fluorescence Laser induced fluorescence (LIF) makes use of an atomic transition in the ion. The laser is directed through the ion cloud. Perpendicular to the laser beam photon detectors, like a photomultiplier tube (PMT) (time resolution) or CCD camera (spatial information), are placed. When the laser is tuned close to an ion transition photons from the laser beam are absorbed and reemitted. A fraction of these photons is detected. The transition in the ion must be a cycling transition, i.e. the upper (excited by the laser) level must decay only into the ground state.[5] If a decay into a third state is possible which does not have an allowed transition into the ground state, all ions would eventually be pumped into that third state and therfore be unavailable for further resonant scattering processes with the laser. The detected rate $\frac{\mathrm{d}N_{\mathrm{LIF}}}{\mathrm{d}t}$ of scattered photons from a cloud of N ions is given by:

$$\frac{\mathrm{d}N_{\mathrm{LIF}}}{\mathrm{d}t} = N \frac{I}{h\,\nu_L}\,\sigma(T,\nu_L)\,\frac{\Omega}{4\,\pi}\,\epsilon_{LC}\,\epsilon_{\mathrm{loss}}\,\epsilon_{\mathrm{eff}}\ . \tag{2.39}$$

Here $\epsilon_{LC} \approx 3 \cdot 10^{-3}$ describes the overlap of the cloud with the laser beam, $\epsilon_{\mathrm{loss}} \approx 0.6$ is the detection efficiency for photons due to reflection on glass surfaces, $\epsilon_{\mathrm{eff}} \approx 0.2$ is the detection efficiency of the photomultiplier tube and $\Omega \approx 0.033 \cdot \pi$ is the detection solid angle.

If the transition is saturated Equation (2.39) changes to

$$N_{\mathrm{LIF}} = N \frac{1}{\tau}\,\frac{\Omega}{4\,\pi}\,\epsilon_{LC}\,\epsilon_{\mathrm{loss}}\,\epsilon_{\mathrm{eff}}\ , \tag{2.40}$$

[5]In Retrap the temperature of the background radiation is 4.2 K and the collisional coupling to the different energy levels is very weak. Therefore, all the ions will eventually be in the ground state and no excited state is populated and no transitions from an excited state can be driven.

where τ is the life time of the upper level. In the case of Be^+ such cycling transitions exist, e.g. 2s $^2S_{1/2}$ ($m_J = -\frac{1}{2}$) $\rightarrow$ 2p $^2P_{3/2}$ ($m_J = -\frac{3}{2}$) [40] [see Figure (4.5)]. The life time of the upper level is 51.5 ns (natural line width γ = 19.4 MHz). In the above equations the overlap with the laser beam ϵ_{LC} is a parameter which changes depending on the density, number of ions and laser beam diameter. The given value was calculated for a rather large cloud (10^6 ions) and a beam diameter of about 180 μm, and is therefore a lower estimate.

2.4 Laser

The laser system used consists of an argon ion laser (*COHERENT Sabre*) capable of delivering 15 W at 514.5 nm and two dye ring lasers (*COHERENT 899-21*). As an alternative a diode pumped solid state (DPSS) laser (*COHERENT VERDI-V10*) was used as a pump laser. This system delivered 10 W at 532 nm. Kiton Red was used as a dye to produce the wavelength of $\lambda \approx 626$ nm. The resulting light was frequency doubled by an intra-cavity frequency doubler ($LiIO_3$) to reach $\lambda \approx 313$ nm. With fresh dye and optimal tuning of the dye lasers, power levels of up to 20 mW at $\lambda \approx 313$ nm could be achieved, but 5 mW was enough to perform laser cooling. The system as it was used is shown in Figure (2.9). Both the UV beams pass through a beam expander and are then steered, with a system of mirrors, to the experiment. At Retrap the beams are separated from each other and sent on different paths through the system. The optical setup at Retrap is shown in Figure (2.10). Each beam is focused in the center of the trap by a lens. A $\frac{\lambda}{2}$-plate guarantees the horizontal polarization.

The red, fundamental laser beam was used for wavelength measurement and frequency stability check. To determine the wavelength of dye laser #1 [the probe laser; see Chapter (5.3.4)], the beam was split into three: the first passing through an iodine cell, the second through a marker etalon, and the third entered the wavelength meter. The wavelength meter provided for a rough measurement of λ

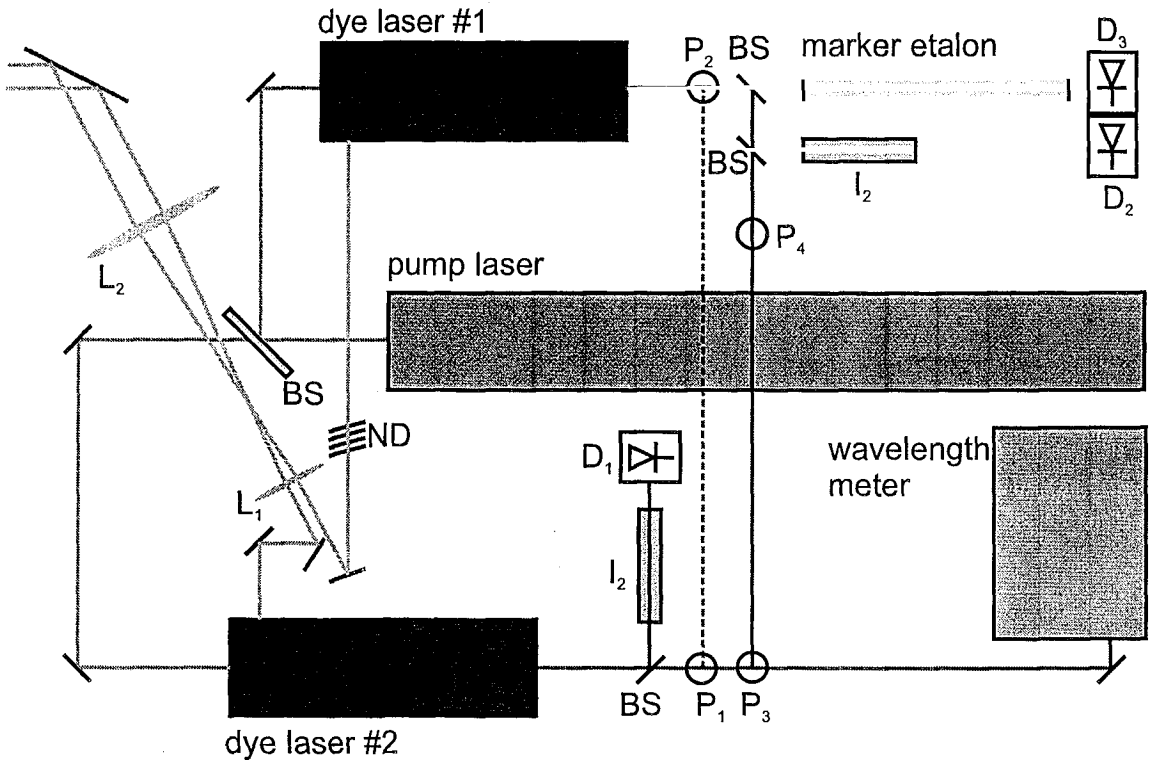

Figure 2.9: Set-up of the lasers. The pump laser (either Ar^+ or diode pumped solid state laser) pumps two dye-ring lasers with internal frequency doubling crystals. The fundamental light exits to the right, the doubled light on the side of the dye lasers. Laser #1 is optically connected to the marker etalon. Laser #2 (cooling laser) can be connected by installing periscopes P_1 and P_2. Periscopes P_3 and P_4 lead the light of laser #1 (probe laser) to the wavelength meter, which can take the input of either of the lasers. Lenses L_1 and L_2 form a telescope to widen the UV-beam, so it can be transported better to the experiment. The iodine cells (I_2) determine the absolute wavelengths of the two dye lasers. D_1, D_2 and D_3 are photo diodes, BS are beam splitters, and ND are neutral density filters to attenuate the probe beam.

($\frac{\Delta\lambda}{\lambda} = 3.2 \cdot 10^{-6}$). For later experiments a different wavelength meter with a higher resolution ($\frac{\Delta\lambda}{\lambda} = 1.6 \cdot 10^{-7}$) was used. A Marker etalon measures λ much more precise. The free spectral range of 150 MHz allowed a relative wavelength measurement of $\frac{\Delta\lambda}{\lambda} = 3 \cdot 10^{-9}$ (1/100 of the free spectral range). Since only relative measurements are possible, the absorption lines in I_2 were used to get the absolute wavelength. These lines are known with a precision of $\frac{\Delta\lambda}{\lambda} = 6.3 \cdot 10^{-9}$ (10^{-4} cm^{-1}) and are frequently used

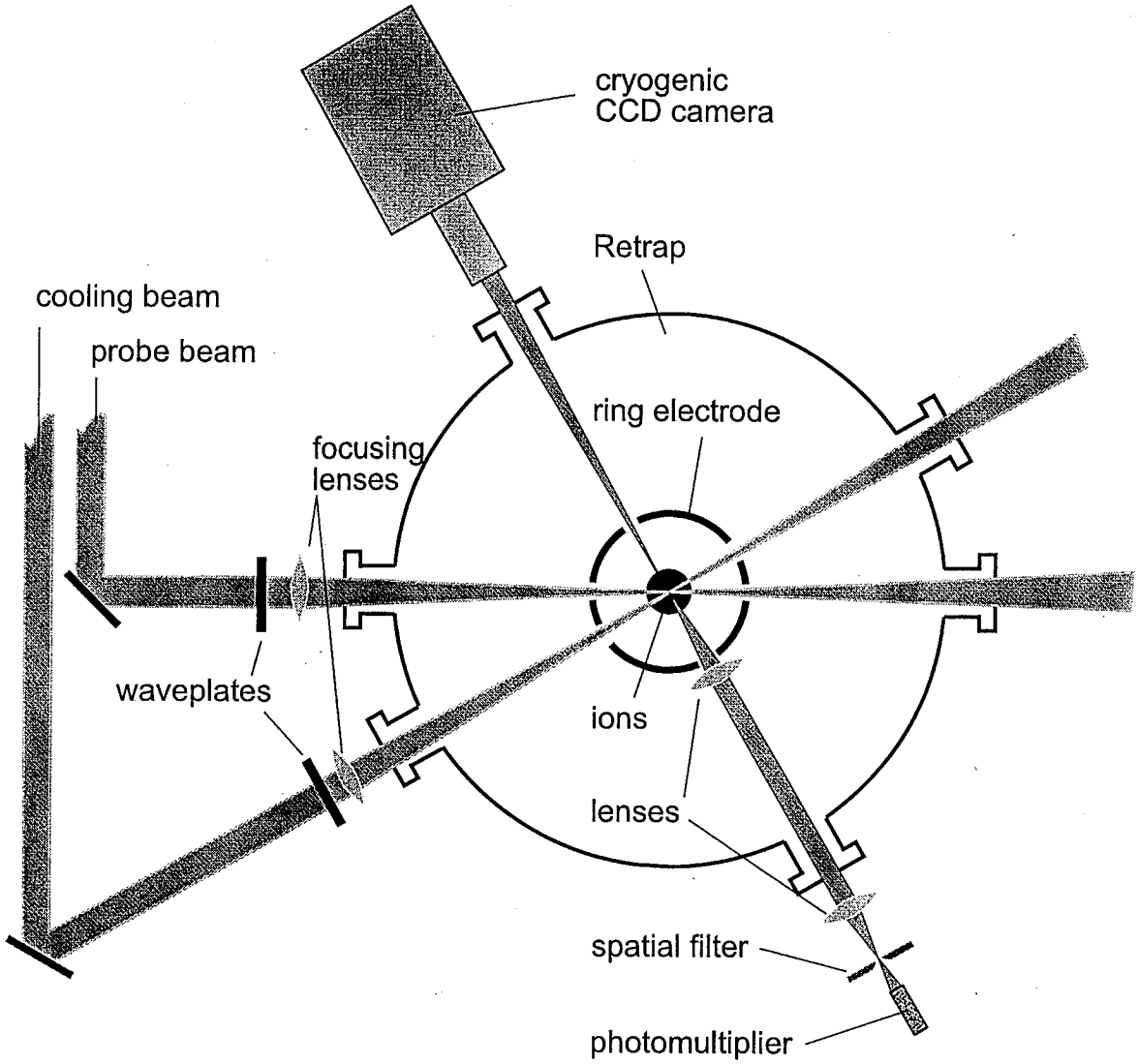

Figure 2.10: Optical setup at Retrap in a top view. Both beams are focused into the trap center through holes in the ring. Perpendicular to the cooling beam, photons are detected with either a CCD camera or a PMT.

as an easily available laboratory wavelength standard. Due to temperature broadening these lines could be measured with a precision of $\frac{\Delta\lambda}{\lambda} \approx 2 \cdot 10^{-7}$, which was sufficient for use in the described experiments. The dye laser line width is ≤ 500 kHz and the frequency stability for short times is $\approx 2-4$ MHz but a long time drift of up to 30 MHz over several hours was observed. This drift can be overcome by actively locking the laser frequency to one of the iodine lines. Such a stabilization has to be

implemented for precision measurements or precision control of the plasma. However, both ring lasers are actively stabilized to a heated reference cavity. Dye laser #2, used as the cooling laser, has the same setup for the wavelength diagnostic, but it is not connected to the marker etalon. The frequency calibration with the marker etalon was performed after the experiment. The spatial stability of the UV beams at Retrap depends extremely on the beam transport and is difficult to quantify. It is stable enough to perform rough experiments, but this as well as the frequency stabilization needs to be improved by adding active feedback loops in order to perform high precision spectroscopy or high precision ion cloud manipulation.

3 Strongly Coupled Plasmas and Coulomb Crystals

3.1 Definition

In a *strongly coupled plasma* the Coulomb interaction between particles with charge q is equal to or larger than the thermal energy $k_B T$ of the particles. The Coulomb coupling parameter Γ is used to distinguish between weak and strong coupling:

$$\Gamma = \frac{q^2}{4\pi\epsilon_0\, a_0\, k_B T} \begin{cases} \ll 1 & \rightarrow \text{ weakly coupled plasma} \\ \geq 1 & \rightarrow \text{ strongly coupled plasma,} \end{cases} \tag{3.1}$$

with the Wigner-Seitz radius

$$a_0 = \left(\frac{3}{4\pi n}\right)^{\frac{1}{3}} . \tag{3.2}$$

The coupling parameter Γ can be drastically increased by lowering the temperature and by increasing the charge state q. In the strongly coupled regime the Coulomb interaction of the particles can no longer be ignored and the plasma cannot be treated as an ideal, collisionless, low-density plasma. The plasma will show properties of a liquid, due to short range correlations between particles. Such correlations are typical for high density plasmas, therefore any plasma showing these correlations is often called high density[6] plasma. If Γ exceeds 172 (for a one component plasma) the plasma crystallizes and is referred to as a 'Coulomb crystal' or, if the total number in the crystal is low, 'Coulomb cluster' [41].

3.2 Examples of Strongly Coupled Plasmas

3.2.1 Astrophysical Objects

Most astrophysical plasmas are weakly coupled, despite the fact that some of them have very high densities, since the temperature is very high due to the nuclear burning

[6] In this work *density* and *particle density* are used as a synonym unless otherwise stated.

process and the Coulomb coupling parameter Γ is only weakly dependent on the density:

$$\Gamma \propto n^{\frac{1}{3}} \cdot \frac{1}{T} \,. \tag{3.3}$$

However, there are two examples of astrophysical objects with matter in the strongly coupled regime: Brown Dwarfs and White Dwarfs (WDs).

3.2.1.1 Brown Dwarfs Stars with initial masses of less than $0.08\,M_\odot$ ($M_\odot = 1.989 \cdot 10^{30}$ kg is the mass of our sun) do not have enough gravitational pressure to compress their matter to the point where nuclear burning can start. These objects are called Brown Dwarfs. Large planets, like Jupiter with a mass of ≈ 0.001 $M_\odot$, could be considered to be a Brown Dwarf. The temperature is low ($< 10^6$ K; Jupiter interior: $T = 2 - 3 \cdot 10^4$ K), but the density is rather high (Jupiter interior: $3.5 \cdot 10^{30} \frac{1}{\mathrm{m}^3}$), and the Coulomb coupling parameter can reach values as high as $\Gamma \approx 20$. This is the region where fluid like behavior of matter can be expected. Much stronger coupling is found in WDs.

3.2.1.2 White Dwarfs Stars with an initial mass of 1 to 8 $M_\odot$, go through the cycle of nuclear burning of hydrogen, producing helium. After the hydrogen resources are exhausted, the star collapses and heats up resulting in a nova explosion and begins nuclear burning of helium in a process called He3-burning, where carbon is produced and oxygen can be generated by sequential capture of neutrons. In the explosion the star typically loses enough mass to end up as a WD with a mass of ≈ 0.6 to $1.0\,M_\odot$. Such stars are too light to generate enough gravitational pressure to overcome the pressure of the degenerate electron gas and start nuclear burning of carbon. Therefore, they consist mostly of oxygen and carbon. These stars, in absence of close stellar objects, will cool off by emitting radiation thereby reducing luminosity. If a WD is part of a binary system, it can accrue mass from the other star and eventually overcome the Chandrasekhar limit of $1.4\,M_\odot$. At this point the

degenerate electron gas pressure is unable to sustain the body of the star. The star will collapse again, start carbon burning and explode as a supernova.

WD interiors have densities of up to $10^{40}\frac{1}{\mathrm{m}^3}$ at temperatures of up to $2 \cdot 10^7$ K, resulting in a Γ of $\approx$ 290 (for fully stripped O). In these stars the electrons are completely degenerate and their screening effects are therefore negligible. They act as a neutralizing background and the thermodynamical properties of the star depend mostly on the fully stripped ions which are crystallized in the core of the star, liquid like in the intermediate layers, and gas like in the outermost layer. The freezing front and the liquid-gas transition moves outward as the star cools off.

From astronomical observations the number of WDs was measured as a function of their luminosity L. It was found, that the number of WDs have a drastic drop-off at luminosities of $2.5\text{–}4.0 \cdot 10^{-5} L_\odot$, where $L_\odot = 3.8 \cdot 10^{26}\frac{\mathrm{J}}{\mathrm{s}}$ is the luminosity of our sun [see Figure (3.1)]. This drop in the so-called luminosity function for faint WDs was attributed to the finite age of the Galactic disk and therefore, no fainter (older) WDs exist. If the cooling model for such burned out stars is known, the age of the Galactic disk can be determined. In such models latent heat in the freezing and liquefying process of WD matter play an important role. Sophisticated models to calculate these energies have been created and used to perform such calculations, but no measurements so far were possible. One path to performing experiments relevant to such plasmas are mixtures of HCIs with lower charge state ions.

3.2.2 Laboratory Experiments

There are a variety of laboratory plasmas which can reach the regime of being strongly coupled. Generally the systems have low temperatures since high enough densities to compensate cannot be achieved. The most strongly coupled plasmas are actually plasmas which are cooled to extremely low temperatures.

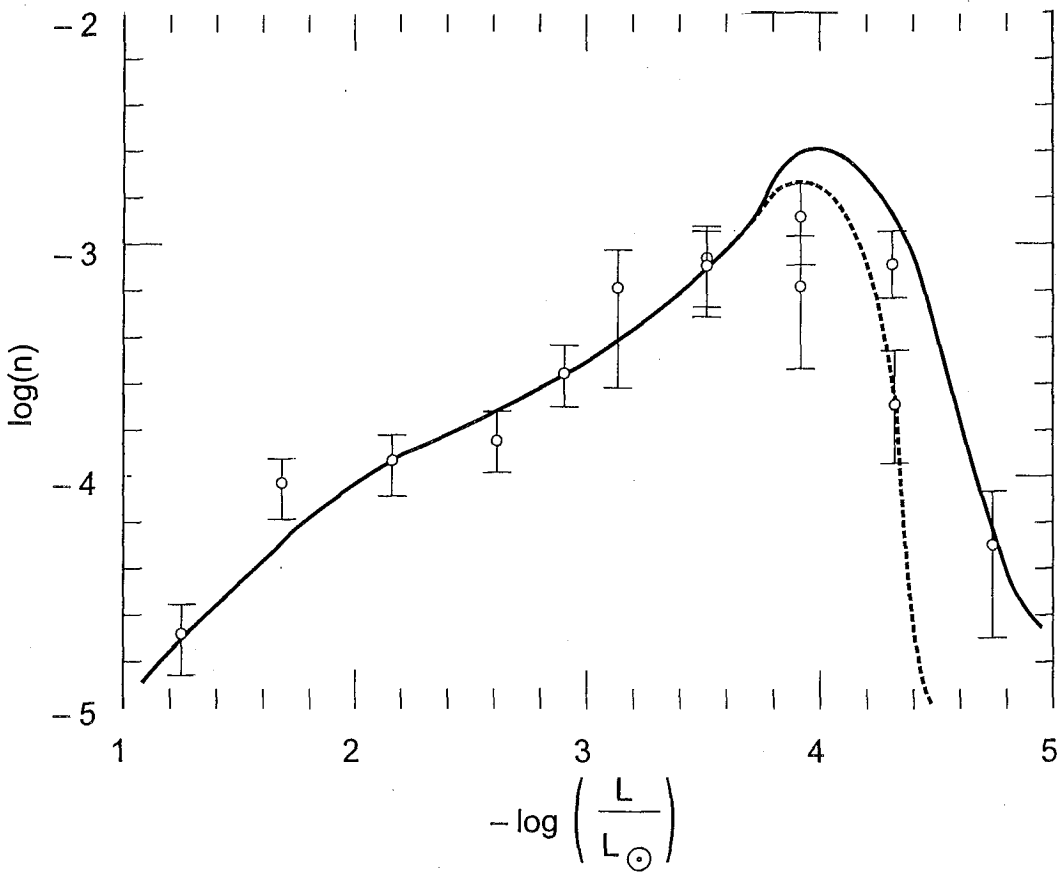

Figure 3.1: The luminosity function of White Dwarfs (WDs): the number of WDs as a function of their luminosity. A drastic drop-off for faint WDs can be seen. Therefore, the age of the Galactic disk can be determined if the cooling mechanism of WDs is well known. The solid curve is a fit including latent heats in phase transitions and the dashed curve is the radiative cool-off model. Data from Hernanz et al. [42].

3.2.2.1 Laser Produced Plasmas In most cases, these plasmas are only in the strongly coupled regime for a short time (ps) [43, 44, 45, 46]. Therefore, they are extreme examples of non-equilibrium plasmas. Inertial confinement fusion experiments produce plasmas of a DT-target by high-power laser irradiation. In the beginning stage of such an experiment just as the target is ionized, the density is high and the temperature is still low enough that $\Gamma \approx 10$ can be achieved. After this stage the temperature rises and Γ decreases.

A similar experimental situation can be observed with short pulse laser produced plasmas on surfaces. A ultra short laser pulse is fired onto a surface and the deposited energy ionizes the matter. At this point high Γs can be achieved, but the plasma is quickly expanding and the density drops.

3.2.2.2 Colloidal Suspensions and Dusty Plasmas One possibility to simulate a strongly coupled plasma is to charge macroscopic particles and suspend them in a solution. This solution can be a variety of materials. Two possibilities are listed here: In a *colloidal suspension* [47] water or saltwater is being used to suspend charged latex spheres of diameters of $0.1\mu\text{m} - 1\mu\text{m}$ and charges of $\approx 10^4 e^-$ forming a two-dimensional lattice. Most of the experiments are performed at room temperature and Γ can achieve extremely high values. However, the water suspension has a significant impact on the particle interaction due to screening and molecular and hydrodynamic effects. The system is rather complicated to describe theoretically. Similar complications are encountered in *dusty plasmas* [48], where again macroscopic particles ($2 - 50\mu\text{m}$ diameter) are charged ($10^3 - 10^5 e^-$), but they are suspended in a high frequency discharge plasma and therefore the discharge plays a major role in the screening process. Γ can reach very high values in this case as well and even three-dimensional structures are formed and can be investigated. The main interest for dusty plasmas is the application in the semiconductor industry, where dust particles can be trapped in the discharge of a plasma etching process and can, after the discharge is turned off, contaminate the sample.

3.2.2.3 Nonneutral Plasmas Nonneutral plasmas are systems of particles with one single sign of charge confined in a trap. This trap can either be a Penning trap, where the confinement is provided by static magnetic and electric fields or a Paul (rf) trap with static and rf electric fields. Since nonneutral plasmas in Penning traps are the topic of this work the next section is dedicated to such objects.

3.3 Nonneutral Plasmas

Plasmas consisting only of particles with a single sign of charge are called nonneutral plasmas and are typically realized with either positive ions, electrons, positrons or antiprotons (to name the most common types). These plasmas can be confined with static electric and magnetic fields for a long period of time. A simple consideration for particle confinement can be extracted from the angular momentum conservation. The total angular momentum $\vec{L}$ of N particles is conserved as long as no external torques act on the plasma cloud:

$$\vec{L} = \sum_{j=1}^{N} m\,\vec{r}_j \times \vec{v}_j + q_j \frac{\vec{B}}{2}\,\vec{r}_j^{\,2} = \text{const.} \tag{3.4}$$

For high magnetic fields, the second term in the sum dominates and Equation (3.4) can be rewritten as:

$$\frac{\vec{B}}{2} \sum_{j=1}^{N} q_j\, r_j^2 = \text{const.} \tag{3.5}$$

This is a confinement constraint for particles with only one sign of charge (e.g. $q_j = q = |q|$ for positive charges), which follows only from the angular momentum conservation law. If only a few particles have a substantial increase in radius, all the other particles are confined to a much smaller radius. However, for neutral plasmas the condition in Equation (3.5) can still be true if particles with opposite but equal charges increase their radius. Equation (3.5) is a confinement condition only for nonneutral plasmas.

The possibility to easily confine nonneutral plasmas for a long time has the consequence for these kind of plasmas to reach thermal equilibrium. This is a big advantage in comparison to neutral plasmas, where the confinement is much more difficult and energy has to be supplied to the plasma to keep it from recombination. The constant energy input inhibits the reaching of a thermal equilibrium making studies of equilibrium states infeasible and drives instabilities.

3.3.1 Plasma Properties of Nonneutral Plasmas

The typical definition of a plasma includes quasi-neutrality. This is not the case in nonneutral plasmas, but the plasma can be considered quasi-neutral if the trap potential is included in the model. It acts like a neutralizing background to the charges confined in the trap. It is possible to show that these charged clouds have plasma properties like Debye shielding, plasma oscillations, and instabilities (if driven) to name a few [49]. It is justified to call ion clouds confined in traps plasmas, if the Debye length λ_D is much smaller than the plasma dimensions R_i:

$$\lambda_D = \sqrt{\frac{\epsilon_0 \, k_B \, T}{q^2 \, n}} \ll R_i \, . \tag{3.6}$$

3.3.2 Nonneutral Plasmas and White Dwarfs

Since WDs can be used as chronometers to determine the age of our galaxy their thermal properties are of great interest to the astrophysical community. The cleanest way of producing a WD analogue in a laboratory is to confine multiple species of ions in a ion trap and cool them to low temperatures, so their Coulomb coupling parameter Γ exceeds a certain value and they arrange themselves in a regular structure. For one component plasmas this happens at $\Gamma = 172$. In order to be an analogue to a WD, where the ions are confined by gravitation, the different ion species have to stay mixed. For a magnetically confining Penning trap, this is only possible for ions with the same mass to charge ratio. HCIs provide more possibilities than lower charge state ions to find different ion species with the same mass to charge ratio and are therefore good candidates to realize such an analogue.

3.3.3 Single-Component Nonneutral Plasmas in a Penning Trap

In Chapter (2.3.2) the confinement of a single ion in a Penning trap and the resulting motions were discussed. In this part the discussion will focus on many trapped ions and how the density of the ion cloud can be extracted from the observable

cloud parameters. The discussion assumes that the charge of the cloud is distributed smoothly in space and it is possible to determine a charge or particle density at every point like it is possible to determine a mass density in a fluid. This is called the 'fluid model'.

Since ions can be trapped for a long period of time in Penning traps, it is reasonable to assume that they are in thermal equilibrium. The thermal equilibrium ion distribution function $f(\vec{v},\vec{r})$ of all the ions in the trap is given by:

$$f(\vec{v},\vec{r}) = n_0 \left(\frac{m}{2\pi\, k_B T}\right)^{\frac{3}{2}} \cdot e^{-\frac{H(\vec{v},\vec{r}) - \vec{\omega}\,\vec{L}_z(\vec{v},\vec{r})}{k_B T}}, \tag{3.7}$$

where

$$H(\vec{v},\vec{r}) = \frac{m\,\vec{v}^{\,2}}{2} + q\,\phi(\vec{r}) \tag{3.8}$$

is the energy of the ions and

$$\vec{L}_z(\vec{v},\vec{r}) = m\,\vec{r}\times\vec{v} + q\,\vec{r}\times\vec{A} \tag{3.9}$$

is the canonical angular momentum. We further assume that only one species with mass m and charge q is trapped in a quadrupole potential $\Phi_T(\vec{r}) = \Phi_T(x,y,z)$ given by Equation (2.19). The total potential $\Phi(\vec{r})$ is then the sum of the trap potential $\Phi_T(\vec{r})$, the ion space charge potential $\Phi_S(\vec{r})$ and the induced potential on the electrodes $\Phi_I(\vec{r})$:

$$\Phi = \Phi_T + \Phi_S + \Phi_I\,. \tag{3.10}$$

Inserting Equations (3.8) and (3.9) into Equation (3.7) (the vector potential is chosen to be $\vec{A} = \frac{\vec{B}}{2}\times\vec{r}$) yields

$$f(\vec{v},\vec{r}) = n(\vec{r})\cdot e^{-\frac{\frac{1}{2}m\,(\vec{v}-\vec{\omega}\times\vec{r})^2}{k_B T}}, \tag{3.11}$$

with the ion density

$$n(\vec{r}) = n(\rho,z) = n_0 \cdot e^{-\frac{q\,\Phi - \frac{1}{2}m\,\omega\,(\omega_C-\omega)\,\rho^2}{k_B T}}, \tag{3.12}$$

where $\rho^2 = x^2 + y^2$. For $T \to 0$ it can be seen that the enumerator in the exponential of Equation (3.12) has to be zero for n to be finite:

$$q\,\Phi - \frac{1}{2}\,m\,\omega\,(\omega_C - \omega)\,\rho^2 = 0. \tag{3.13}$$

Using Equation (3.10) and the definition for the quadrupole potential Equation (3.13) becomes

$$\begin{aligned} \Phi_S &= \left[\frac{m\,\omega\,(\omega_c - \omega)}{2\,q} + V_0\right]\frac{\rho^2}{d_0^2} - \frac{2\,V_0}{d_0^2}\,z^2 - \Phi_I \\ &\stackrel{\text{def}}{=} -\frac{2}{3}\,\pi\,q\,n_0\,(a\,\rho^2 + b\,z^2) - \Phi_I\,. \end{aligned} \tag{3.14}$$

Equation (3.14) can be used to evaluate Poisson's equation in cylindrical coordinates (ρ, θ, z):

$$\frac{1}{\rho}\frac{\partial}{\partial\rho}\left(\rho\frac{\partial\Phi_S}{\partial\rho}\right) + \frac{\partial^2\Phi_S}{\partial z^2} = -\frac{q\,n_0}{\epsilon_0}\,. \tag{3.15}$$

Cylindrical symmetry is assumed and therefore, the variable θ is omitted. Equation (3.14) is the potential of a uniformly charged ellipsoid of revolution with a constant density n_0 which is obtained from Equation (3.15):

$$n_0 = \frac{2\,\epsilon_0\,m\,\omega\,(\omega_C - \omega)}{q^2}\,, \tag{3.16}$$

and

$$\begin{aligned} a &= k_{p'}\left[\frac{1}{2(1-k_p^2)} - \frac{\ln\dfrac{1+k_p}{1-k_p}}{4\,k_p}\right] \\ b &= k_{p'}\left[\frac{\ln\dfrac{1+k_p}{1-k_p}}{2\,k_p} - 1\right] \\ k_{p'} &= 3\,\frac{1-k_p^2}{k_p^2} \\ k_p &= \sqrt{1 - \left(\frac{r_{\mathrm{cl}}}{z_{\mathrm{cl}}}\right)^2}\,, \end{aligned} \tag{3.17}$$

where r_{cl} and z_{cl} are the axes of the ellipsoid. Equations (3.17) are valid for a prolate spheroid ($z_{\mathrm{cl}} > r_{\mathrm{cl}}$) and

$$\begin{aligned} a &= k_{O'}\left(\frac{\arcsin k_O}{2\,k_O} - \frac{\sqrt{1-k_O^2}}{2}\right) \\ b &= k_{O'}\left(\frac{1}{\sqrt{1-k_O^2}} - \frac{\arcsin k_O}{k_O}\right) \\ k_{O'} &= 3\,\frac{\sqrt{1-k_O^2}}{k_O^2} \\ k_O &= \sqrt{1-\left(\frac{z_{\mathrm{cl}}}{r_{\mathrm{cl}}}\right)^2} \end{aligned} \tag{3.18}$$

apply if the cloud is an oblate spheroid ($r_{\mathrm{cl}} > z_{\mathrm{cl}}$). The ratio of the axes of the ellipse, the aspect ratio, can be readily measured in the side view image of the ion cloud and the density can be calculated with the parameter b:

$$b = \frac{3\,\omega_z^2}{2\,\omega\,(\omega_C - \omega)} \tag{3.19}$$

From Equations (3.18) it can be seen, that b has to be smaller than or equal to 3. If $b = 3$ is inserted into Equation (3.19) and used to replace $\omega\,(\omega_C - \omega)$ in Equation (3.16), one obtains the minimum fluid density:

$$n_{0,min} = \frac{\epsilon_0\, m\, \omega_z^2}{q^2} \tag{3.20}$$

The minimum density occurs in a plasma where $z_{\mathrm{cl}} \ll r_{\mathrm{cl}}$ which could lead to particle loss to the walls. Therefore, if the plasma is confined and there is no loss of particles this density is a good estimate for the lower density limit of a one-component plasma in such a trap.

A maximum density can be obtained by setting the derivative of Equation (3.16) with respect to ω equal to zero:

$$\frac{\partial n_0}{\partial \omega} = \frac{2\,\epsilon_0\, m\,(\omega_C - 2\,\omega)}{q^2} = 0\,. \tag{3.21}$$

The maximum density is obtained for $\omega = \frac{\omega_C}{2}$ and is called the Brillouin density:

$$n_B = \frac{\epsilon_0 \, m \, \omega_C^2}{2 \, q^2} = \frac{\epsilon_0 \, B^2}{2 \, m} \; . \tag{3.22}$$

Therefore, the density of the plasma n_0 has to be in the interval:

$$n_{0,min} \leq n_0 \leq n_B \; , \tag{3.23}$$

which can be made smaller by increasing the trap voltage V_0 and therefore increasing ω_z. The limit occurs when $n_{0,min} = n_B$ and we obtain for the axial angular frequency:

$$\omega_z^2 \leq \frac{1}{2} \omega_C^2 \; . \tag{3.24}$$

This is the same condition as the one given in Equation (2.30).

3.3.4 Many-Component Nonneutral Plasma

If multiple ion species are trapped in a Penning trap, they will initially be mixed. Due to centrifugal forces ions with different mass to charge ratios at the same radial position rotate at different rates about the plasma axis [50, 51]. Because of their different rotation rates there will be an angular momentum transfer between species, increasing the angular momentum for one species and decreasing it for the other. Species with increasing angular momentum will be compressed and forced toward the center of the trap and other species with decreasing angular momentum are forced to larger radii. This process will continue until all the species are rotating at the same rate, which results in a centrifugal separation of the ion species with different mass to charge ratios [50, 52]. At this point the whole mixed cloud is in thermal equilibrium and rotates as a rigid body since all the species have the same rotation frequency.

The geometrical shape of the different clouds is not anymore a spheroid. The different species form concentric rings ordered by their mass to charge ratio, where ions with a small mass to charge ratio are in the trap center. It is difficult to give an illustration what the exact shape of the rings is, but in some experiments with singly charged ions the different species were imaged [52, 53].

If the whole cloud rotates as a rigid body with the angular frequency ω and the angular cyclotron frequency $\omega_C \gg \omega$, then one can obtain from Equation (3.16) the following approximation:

$$\begin{aligned} n_0 &\approx \frac{2\,\epsilon_0\, m\,\omega\,\omega_C}{q^2} \\ &= \frac{2\,\epsilon_0\, B\,\omega}{q} \\ &\propto \frac{1}{q}. \end{aligned} \tag{3.25}$$

Therefore, if the rotation frequency is known from measuring the aspect ratio of one species, it can be given for any species in the same cloud as long as the charge of that cloud is known.

Knowing that the different ion species separate, it is clear that in order to simulate a White Dwarf plasma mixture, it is necessary to produce a mixture in the trap which consists of two different ion species with the same mass to charge ratio. This is one of the advantages of using high mass HCIs since there is the possibility to adjust the mass to charge ratio in much smaller steps and matching the mass to charge ratios is easier. Potential candidates for such experiments to mix with $^{136}Xe^{44+}$ are listed in Table (3.1).

Table 3.1: Suited isotopes to mix with $^{136}Xe^{44+}$. The mass to charge ratios are given in units of proton masses m_p over electron charges e^- and they are corrected for the missing electrons.

Ion	m [54]	q	$\frac{m}{q}$	Abundance
	m_p	e^-	$\frac{m_p}{e^-}$	%
$^{34}S^{11+}$	33.96787	11	3.08744	4.20
$^{68}Zn^{22+}$	67.92485	22	3.08695	18.80
$^{102}Ru^{33+}$	101.90435	33	3.08747	31.60
$^{102}Pd^{33+}$	101.90563	33	3.08750	1.02
$^{136}Xe^{44+}$	135.90721	44	3.08826	8.90
$^{136}Ba^{44+}$	135.90455	44	3.08820	7.85
$^{136}Ce^{44+}$	135.90714	44	3.08825	0.19
$^{170}Er^{55+}$	169.93546	55	3.08919	14.90
$^{170}Yb^{55+}$	169.93476	55	3.08918	3.05
$^{204}Hg^{66+}$	203.97347	66	3.08996	6.80
$^{204}Pb^{66+}$	203.97302	66	3.08996	1.40
$^{238}U^{77+}$	238.05078	77	3.09102	99.27

4 Cooling Methods

Initially the ions trapped in Retrap typically have energies of up to 200 V $\cdot q$. This corresponds to temperatures of $2.3 \cdot 10^6$ K for Be^+ and to 10^8 K for Xe^{44+}. The goal of this work is to produce strongly coupled plasmas with HCIs to make further research on such systems feasible. At these temperatures and the highest achievable densities of Xe^{44+} in a Penning trap ($n = 5 \cdot 10^{11} - 3 \cdot 10^{14} \frac{1}{m^3}$ for a magnetic field of $B = 4$ T) the Coulomb coupling parameter is $4 \cdot 10^{-6} - 3.5 \cdot 10^{-5}$. This is 5 – 6 orders of magnitude too low to qualify for a strongly coupled plasma and 2 more orders of magnitude too low for crystallization. Since the density cannot be increased to achieve the strongly coupled regime, the temperature needs to be dropped by 8 orders of magnitude to about 1 K (for the lowest density in the trap). The methods used to achieve this are described in this chapter. Some of the cooling mechanisms (i.e. evaporative cooling, sympathetic cooling) are always present, but can also be enhanced. To use other mechanisms (i.e. resistive cooling, laser cooling) special measures have to be taken.

4.1 Evaporative Cooling

In an collisionally coupled ion cloud confined in a potential well of depth E_0 the ions will thermalize and therefore some ions will obtain enough kinetic energy to escape the confining well. This reduces the total energy in the confined cloud and therefore the temperature drops. To simulate such an experimental situation, the following idealized path is chosen.

A system of N_0 ions is confined in an infinitely deep axial potential well. The kinetic energy of the system is E_0 and it will therefore equilibrate to a temperature of

$$T_0 = \frac{2}{3} \cdot \frac{E_0}{N_0 \, k_B} \, . \tag{4.1}$$

It will have a Maxwell-Boltzmann distribution

$$f(E) = e^{-\frac{E}{k_B T_0}} = e^{-\frac{m v^2}{2 \, k_B T_0}} \, , \tag{4.2}$$

provided the collision rate is high enough to distribute the energy to all degrees of freedom. After this distribution is reached, the axial well depth is dropped to ΔV and $(N_0 - N_1)$ ions have enough energy to escape the potential well. The amount of ions still confined, N_1, is determined by a maximum kinetic energy, $E_m = \frac{1}{2}\, m\, v_m^2$, an ion can have in the potential well of depth $\Delta V = \frac{E_m}{q}$, with q being the charge of an ion:

$$N_1 = N_0\, A \int_0^{E_m} f(E)\, \mathrm{d}E\ . \tag{4.3}$$

The energy, E_z, remaining in the axial degree of freedom of the system is given by

$$E_z = N_0\, A \int_0^{E_m} E\, f(E)\, \mathrm{d}E \tag{4.4}$$

where the following normalizations must be fulfilled: If the Equations (4.4) and (4.3) are integrated over the whole energy range, E_z must equal the total energy in one degree of freedom, $\frac{1}{2}k_B T_0$ and N_1 must be the total number N_0. Thus, one gets:

$$A \int_0^{\infty} E\, f(E)\, \mathrm{d}E = \frac{1}{2} k_B T_0 \tag{4.5}$$

and

$$A \int_0^{\infty} f(E)\, \mathrm{d}E = N\ , \tag{4.6}$$

where the constants A was introduced to satisfy these normalizations. The total energy E_1 of the system after this first ion loss is

$$E_1 = \frac{2\, N_1\, k_B T_0}{2} + E_z = \frac{3\, N_1\, k_B T_1}{2}\ . \tag{4.7}$$

At this point the potential well depth is again made infinitely deep and no ions can escape the well. This causes the system to equilibrate with a new temperature T_1. This sequence of trapping ions in an infinitely deep well for equilibration and then reduction of the well to a certain value to allow for particle loss, can be repeated. Equation (4.7) can be used to solve for T_1:

$$T_1 = \frac{2}{3}\left(T_0 + \frac{E_z}{N_1\, k_B}\right) \tag{4.8}$$

and Equation (4.4) and (4.3) can be inserted into Equation (4.8) to result after some algebra in a iteration rule for the temperature T_i

$$T_{i+1} = \frac{2}{3}\left(T_i + \frac{m}{2k_B} \cdot \frac{\int_0^{v_m} v^2 e^{-\frac{mv^2}{2k_B T_i}} \mathrm{d}v}{\int_0^{v_m} e^{-\frac{mv^2}{2k_B T_i}} \mathrm{d}v} \right) . \tag{4.9}$$

The process of ions escaping the well will become less likely as the system gets to lower temperatures and the cooling process slows down. In Figure (4.1) an example of how the temperature develops over time is shown with the data points. A double exponential was fit to the data and describes it to a good approximation. The number of ions left in the trap is also plotted in the same way and also in this case a double exponential fits the data well. From the fits it is possible to obtain the asymptotic temperature and number of particles. The system starts with 10^6 ions at 300 eV and end up with $3.7 \cdot 10^5$ at 50 eV. This is a reduction of 83 % in temperature, while keeping 37 % of the particles in the trap. In each step the energy lost is $k_B(T_{i+1} - T_i)$ and in order to find the time in which such a process happens the equilibration time, τ_{eq} [see Chapter (4.4)], has to be considered.

The process can be enhanced by slowly, compared to τ_{eq}, making the trap shallow and therefore lowering the energy threshold E_m for the escape. The inherent disadvantage of such a cooling technique is the particle loss. An advantage in the HCI cooling is that the depth of the electric potential is dependent on the charge state of the ion. Ions with the charge q see a potential well which is q times deeper than the same well for singly charged ions. This has the consequence that lower charge state ions will be ejected more likely from the trap if there is a mixture of HCI and lower charge state ions in the trap. This is the mechanism which provides the cooling of the HCIs in EBIT.

An experimental illustration of evaporative cooling is shown in Figure (4.2). In one case Xe^{44+} was captured and detected after it was held for 1 s in the trap (no

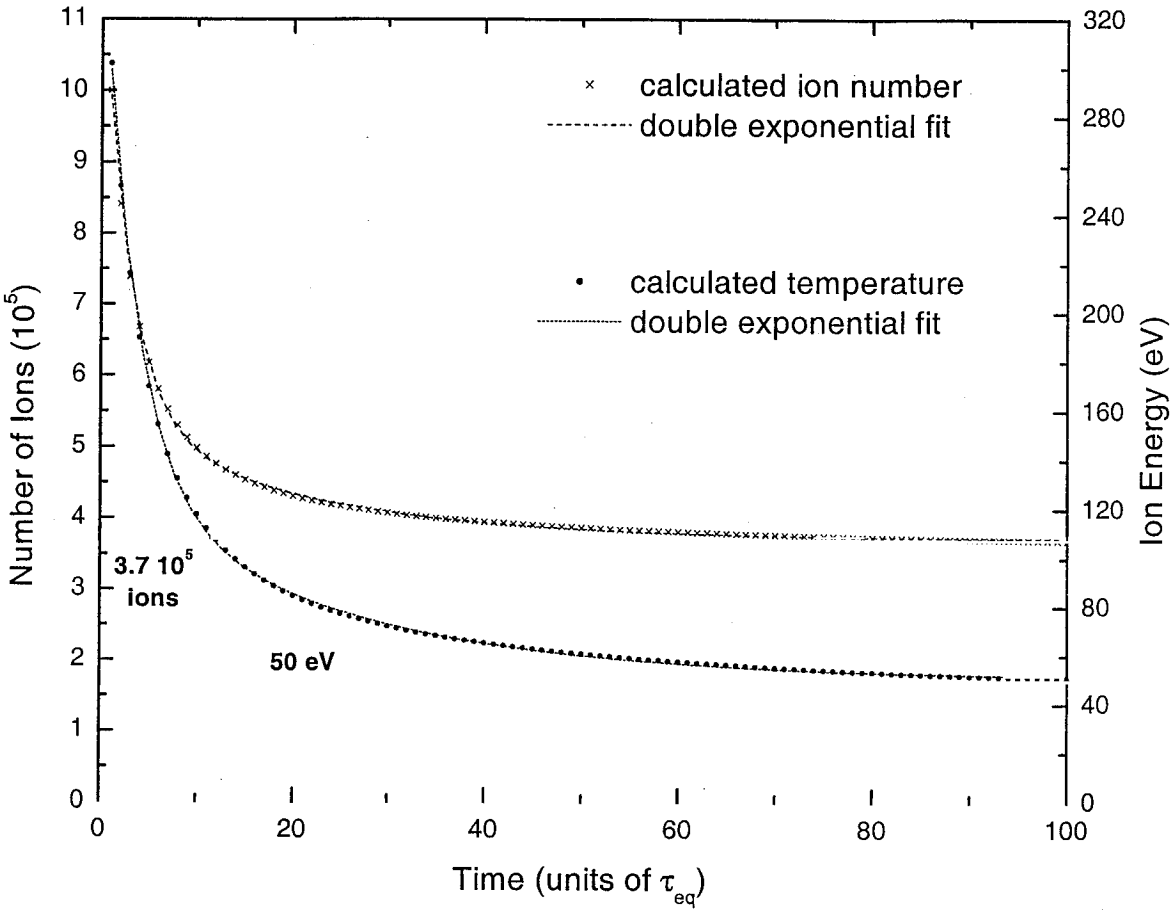

Figure 4.1: Illustration of evaporative cooling. The initial conditions were 10^6 Be^+ ions at an energy of 300 eV ($3.5 \cdot 10^6$ K). The temperature drops rapidly and approaches a final temperature of 50 eV ($5.8 \cdot 10^5$ K) while ions are ejected from the trap. The final number of ions is $3.7 \cdot 10^5$. The calculated points using Equations (4.3) and (4.9) were fit to a double exponential ($y = y_0 + Ae^{-\frac{x}{\tau_1}} + Be^{-\frac{x}{\tau_2}}$), which seems to approximate the simulated data well.

predump). In the other case one of the confining potentials was slowly lowered to maintain — for a short time only — a very shallow potential, thereby evaporating most of the ions (predump). In the case with the predump it can be seen that the signal is greatly reduced but it is possible to resolve single charge states of the captured Xe, indicating a lower temperature. In the case without the predump no charge states can be resolved and the detected peak has a long tail on the side, where

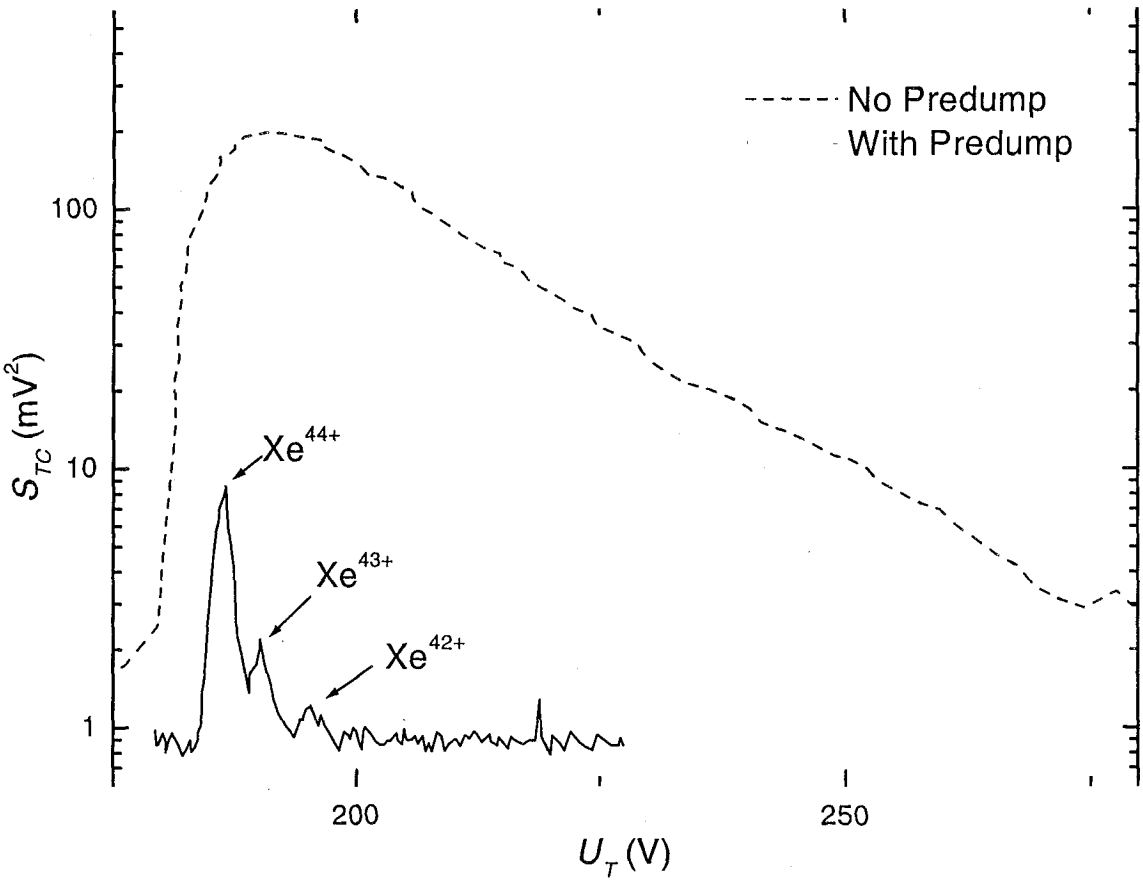

Figure 4.2: Tuned circuit signal S_{TC} as a function of trap potential depth U_T. Without predump (making the axial potential well shallow for a short time) the ions are hot and single charge states can not be resolved. With a predump three charge states of Xe can be seen but the number of ions in the trap is also greatly reduced. Both the low number of ions and the lower temperature cause the signal to decrease substantially.

the potential well is deep, indicating very energetic ions.

4.2 Resistive Cooling

In Chapter (2.3.3) the nondestructive detection of ions in the trap with a tuned circuit has been discussed. This method conserves the trap content, but can perturb it substantially. In the ion detection process, energy is dissipated in the ohmic re-

sistance of the tuned circuit [see Equation (2.33)] and is therefore removed from the ion ensemble, leading to a net cooling of the ions. If Equation (2.34) is inserted into Equation (2.32), it takes the following shape:

$$f = -\left(\frac{q\,\beta}{2\,z_0}\right)^2 \frac{R}{m} \cdot m\,v_z = -\gamma\,m\,v_z\,, \tag{4.10}$$

where the force f is acting in the direction of the velocity v_z. This constitutes a damping force with a damping constant of γ given by:

$$\gamma = \left(\frac{q\,\beta}{2\,z_0}\right)^2 \frac{R}{m}\,. \tag{4.11}$$

This is the rate with which the system is cooled. It can be rewritten involving more experimental parameters:

$$\gamma = \frac{Q\,q^2\beta^2\omega_z L}{4\,m\,z_0^2} \approx 3.10 \cdot 10^{-4}\,\frac{1}{\mathrm{s}} \cdot Q\,\frac{q^2}{M}\,, \tag{4.12}$$

Where q on the right of Equation (4.12) is in units of the electron charge and M is in atomic mass units. Parameters for the hyperbolic trap in Retrap ($L \approx 200\,\mu$H, $z_0 \approx 5$ mm, $\beta \approx 0.8$ and $\omega_z \approx 2.5$ MHz) were used to get the numeric constant of $3.10 \cdot 10^{-4}\,\frac{1}{\mathrm{s}}$.

With Equation (4.12) one dimensional cooling times τ_i for different ion species can be calculated. The quality factor Q is typically about 550.

$\tau_{\mathrm{Be}^+} = 52.7$ s

$\tau_{\mathrm{Be}^{2+}} = 13.2$ s

$\tau_{\mathrm{Xe}^{44+}} = 0.41$ s

It is important to keep in mind that these are cooling times for the axial degree of freedom. The radial degrees of freedom need to be cooled by collisionally coupling to the axial motion, which can involve different time constants.

In Figure (4.3) three cooling curves for Xe^{44+} are shown. The weighted average for the cooling time (some data is not shown) was

$\tau_{\mathrm{m,Xe}^{44+}} = 8.8(5)$ s.

However, a direct comparison of the calculated and the measured time constant is misleading. In the experiment not all the ions are on resonance with the tuned circuit all the time: Very hot ions are not in the harmonic region of the well and are therefore not on resonance. There might be other species of trapped ions, which are not on resonance either. All these ions have to be cooled by collisions. A longer time constant would be measured if the cooling time constant for the axial heating is much smaller than the collisional time constant between the axial and the radial degree of freedom. Once the axial degree is cold, the cooling rate is determined by the collisional coupling of the two degrees of freedom.

The same measurement was performed on a mixture of Be^{2+} and Be^{+}. Be^{2+} was on resonance with the tuned circuit and Be^{+} ($\approx 50\%$ of the total number) had to be cooled by collisions. In this system one degree of freedom cools five equivalent ones and the resulting time constant is

$\tau_{m,Be^{2+},Be^{+}} = 783(6)$ s.

This measurement is shown in Figure (4.4), where it was attempted to keep most of the Be^{2+} on resonance.

The advantage of the resistive cooling is that no particles are lost in the process. However, the cooling limit is the highest temperature of the tuned circuit (amplifier included). Since the amplifier has a rather weak thermal coupling to the 4.2 K environment (conduction through wires for electrical coupling and radiation to the 4.2 K enclosure), the highest temperature can be substantially higher than liquid He temperature, which then would be the lowest achievable temperature.

4.3 Laser Cooling

To achieve temperatures lower than ≈ 10 K (estimated cooling limit for the resistive cooling) without loosing particles, laser cooling schemes can be applied. The field of laser cooling has grown over the past two decades and many different techniques have been successfully applied. However, in the experiments described in this work

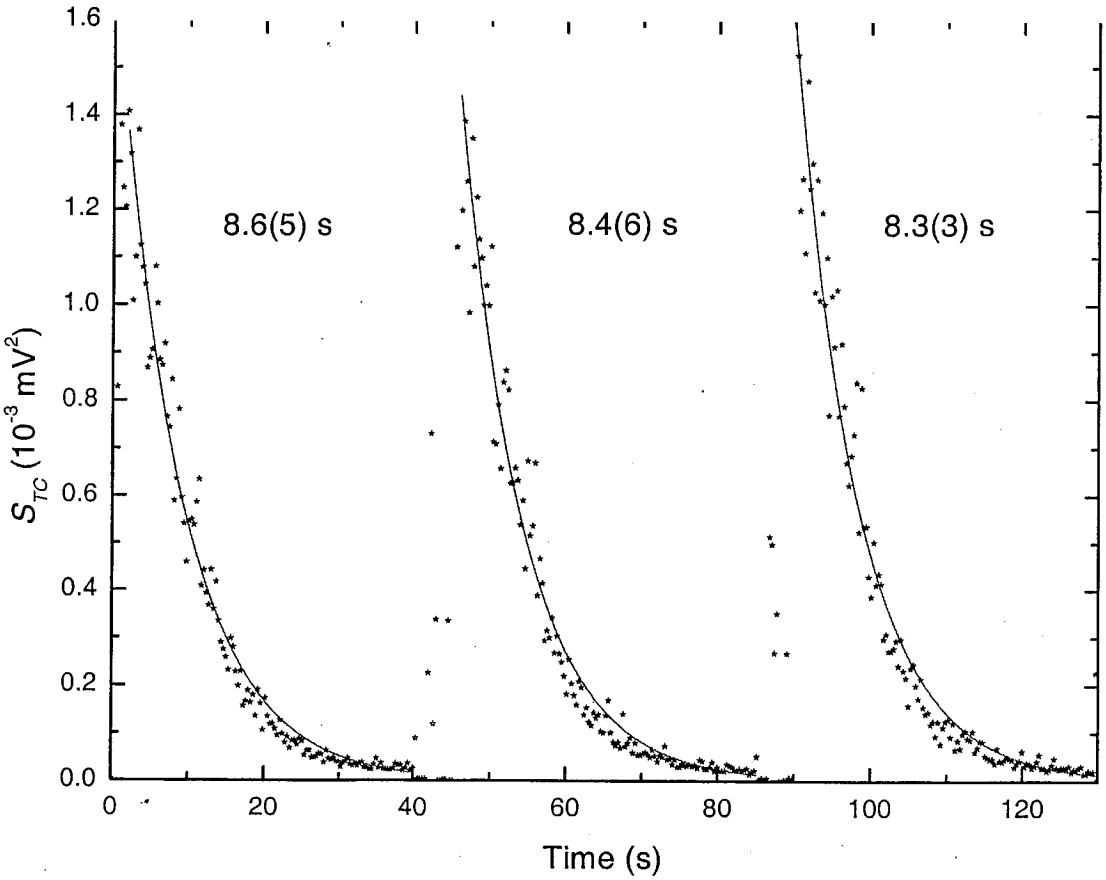

Figure 4.3: Tuned circuit signal S_{TC} as a function of time, while Xe^{44+} is on resonance: resistive cooling curves of three different loads of Xe^{44+}. A simple exponential decay was fit to the data and the resulting time constants are noted in the graph.

laser cooling means exclusively laser Doppler cooling for a weakly bound resonant absorber. This has the consequence that any sidebands from the motion of the ions are not resolved and can formally be stated as

$$\gamma \gg \omega_i \,, \tag{4.13}$$

where γ is the natural line width of the cooling transition and ω_i $(i = C, R, +, z, -, ...)$ are any motional frequencies of the ions in the trap. In this case the ion can be considered as a free particle during the scattering process, since the scattering happens on a timescale of $\frac{1}{\gamma}$.

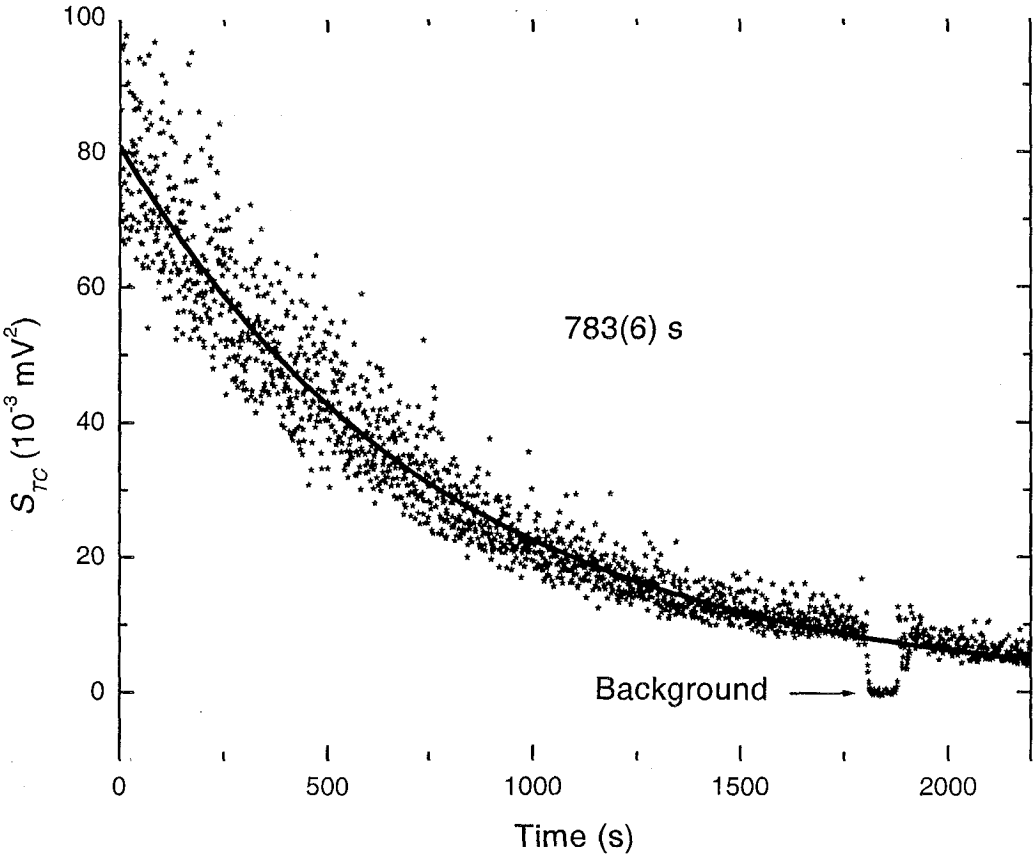

Figure 4.4: Tuned circuit signal S_{TC} as a function of time, while Be^{2+} is on resonance. A simple exponential decay was fit to the data and the resulting time constant is noted in the graph. The ions were briefly tuned off resonance to determine the background.

For a detailed review of laser cooling of ions in a trap see [55, 56]. Some relevant results from the theory of laser cooling are summarized in the following. A photon from a laser, detuned by $\Delta = \nu_L - \nu_0$ with the wave vector $\vec{k}_L$ (frequency ν_L) is absorbed by an ion of the mass m with the velocity $\vec{v}$ and afterwards reemitted at the resonance frequency ν_0 with the wave vector $\vec{k}_0$. From the conservation laws it can be derived that the average energy transfer per scattering event to the ion is

$$\Delta E = 2\pi\hbar\,\Delta = \hbar\,\vec{k}_L \cdot \vec{v} + 2\,R\,, \tag{4.14}$$

where R is the recoil energy of the ion and $\hbar$ is Planck's constant over 2π. For cooling

ΔE has to be negative and from this it can be seen that

$$\Delta < 0 \tag{4.15}$$

and

$$\hbar \vec{k}_L \cdot \vec{v} < -2\,R \tag{4.16}$$

must be satisfied. From Equation (4.16) it can be seen that the photon has to be counter propagating to the ion. The velocity component in the direction of the photon flux will therefore be reduced. Since the photon will be remitted with equal probabilities in all directions, a reduction of kinetic energy will only affect one direction and a net heating of the perpendicular degrees of freedom will take place. The energy of the emitted photon is smaller than the energy of the absorbed photon and therefore a total net cooling is established. In order to cool all degrees of freedom, six laser beams have to be applied in all positive and negative directions in space. From Equations (4.15) and (4.16) it can be seen that if $\Delta > 0$, the energy of the ion is increased and the ion is heated if it copropagates with the laser beam.

The cooling rate can be found by multiplying the scatter rate with the average energy transfer per scattering event. The scatter rate can be found by multiplying the incident photon number per area and time ($\frac{I}{h\nu_L}$) by the atomic absorption cross section σ_a. The result for the cooling rate is

$$\frac{\mathrm{d}E}{\mathrm{d}t} = \frac{I}{h\,\nu_L} \cdot \sigma_a(\nu_L) \cdot \left[\hbar \vec{k}_L \cdot \vec{v} + 2\,R\right] , \tag{4.17}$$

where $\vec{v}$ still needs to be averaged over a Maxwell-Boltzmann distribution. The result of this average yields an expression, which can be approximated with

$$\frac{\mathrm{d}E}{\mathrm{d}t} = \frac{I}{h\,\nu_L}\sigma_s(\nu_L)(h\,\Delta + R) , \tag{4.18}$$

where the scattering cross section $\sigma_s(\nu_L)$ is:

$$\sigma_s(\nu_L) = \sigma_0 \frac{\gamma\sqrt{\pi}}{2\,\nu_D} \cdot e^{-\left(\frac{\Delta - \frac{R}{\hbar}}{\nu_D}\right)^2} \tag{4.19}$$

and the resonance scattering cross section for unpolarized ions is $\sigma_0 = \frac{\lambda^2}{2\pi}$.

The limit for this cooling process can be derived to

$$\langle E_{x,min} \rangle = \frac{\hbar\gamma}{4} . \tag{4.20}$$

If the ions have a Maxwell-Boltzmann distribution then $\langle E_{x,min} \rangle = \frac{1}{2}k_B T$ and the minimum temperature achievable is

$$T_{min} = \frac{\hbar\gamma}{2k_B} \approx 0.5 \text{ mK} , \tag{4.21}$$

where $\gamma_{Be^+} = 2\pi \cdot 19.4 \cdot 10^6 \frac{1}{s}$. However, the minimum temperature given in Equation (4.21) can be substantially higher if other heat sources are present.

If the ion is trapped in a three dimensional trap, like a Penning trap, then the laser cooling becomes experimentally simpler, since six laser beams are no longer required. If the different degrees of freedom of the ions are collisionally coupled, one laser beam is sufficient to cool the whole ion cloud.

In Retrap the cooling laser was chosen to be introduced radially and it therefore cools the two radial degrees of freedom by reducing the cyclotron kinetic energy. In the Be^+ plasma the radial degrees of freedom are collisionally coupled to the axial degree even at temperatures far below 1 K [see Chapter (6)]. For the case of Xe^{44+} the coupling becomes weak at temperatures below about 10 K, but since the Xe ions will not directly be laser cooled it only matters whether the axial motion of the Xe ions are coupled to the axial motion of the Be ions. For a more detailed discussion as of why the coupling at low temperatures becomes weaker see [57].

In Figure (4.5) the chosen Be^+ cooling transition as well as the transition used to depopulate the $m_J = -\frac{1}{2}$ ground state [see Chapter (5.3.4)] are shown. The cooling transition excites the ions into the 2p $^2P_{3/2}(m_J = -\frac{3}{2})$ level, where they can fall back only into the 2s $^2S_{1/2}(m_J = -\frac{1}{2})$ ground state. All other decays cannot happen in an electric dipole transition, indicated by the selection rules in the figure.

Experimentally the laser cooling can be observed by looking at the cloud with a PMT. A typical pattern of the PMT signal for large (several GHz) detunings is

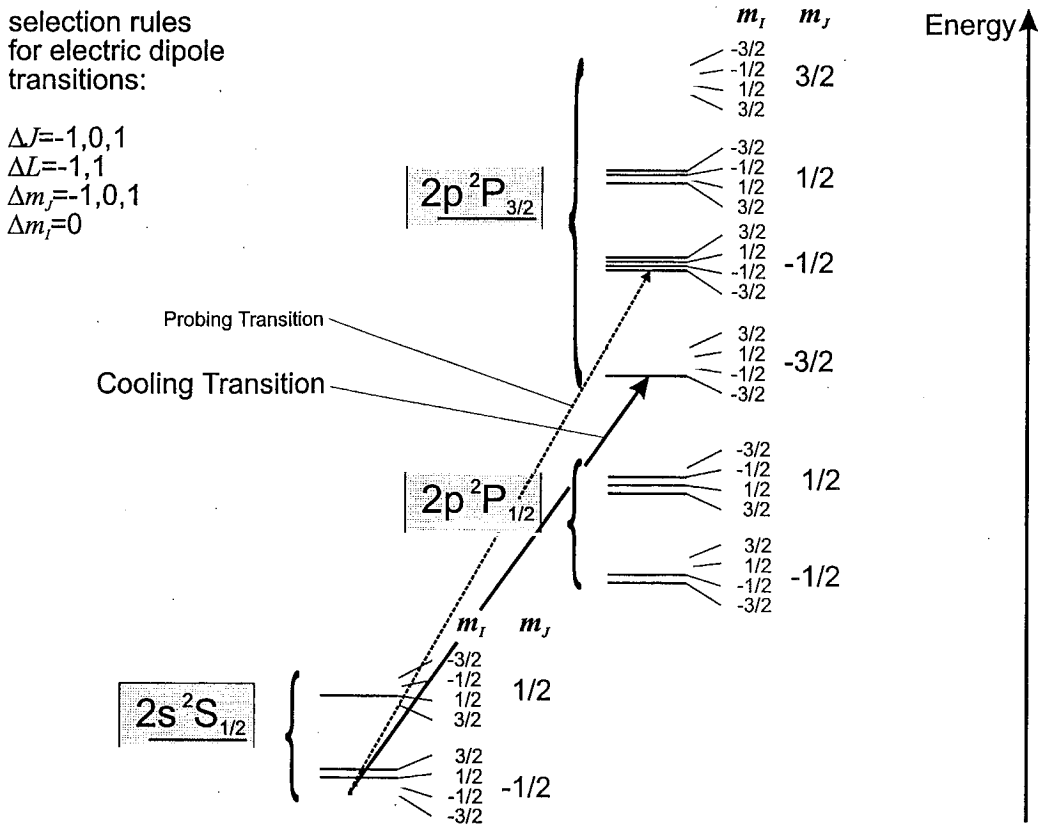

Figure 4.5: Energy term scheme for Be^+ in a high magnetic field. The 2s $^2S_{1/2}$ ground state and the two next higher 2p $^2P_{1/2}$ and 2p $^2P_{3/2}$ excited states are shown in the scheme. All the energy levels split into $2J+1$ hyperfine levels with different m_J quantum numbers. Each of these levels split again into four (the nuclear spin of ^9Be is $\frac{3}{2}$) different sublevels with different m_I quantum numbers. The transition used for laser cooling and the transition to depopulate the $m_J = -\frac{1}{2}$ ground state and pump it into the 2s $^2S_{1/2}$ ($m_J = +\frac{1}{2}$) state, are indicated as well.

shown in Figure (4.6)a. After Be^+ injection the scatter rate increases slightly and continues to slowly increase over a time of 1000 s. During this time the ions are hot (the average velocity is much higher than the velocity which is on resonance with the laser, therefore they scatter only when the velocity component in the direction of the laser matches the Doppler shift) and the time interval their velocities are on resonance with the cooling laser is very short. However, the ions are slowly being cooled, which brings the velocities into the range where more particles spend more

time on resonance with the laser light and the signal on the PMT increases faster, until eventually all the ions are cooled. Their velocities are lower than the velocity on resonance with the laser. Therefore, no ion will be on resonance, which causes the signal to drop abruptly. This described signal pattern is a typical cooling curve. If the plasma is heated, the ion velocities are pushed to higher values and the previously described cooling curve is being run through in reverse. If the heating happens fast it is possible that the PMT (depending on the time constant for the observation) does not detect the full signal height. This is the case in Figure (4.6), when Xe is injected. Only a small peak is being observed, representing the reverse cooling curve, but then the ions are hot and the cooling process starts over. If less heat is added to the system [i.e. by just pulsing the voltages on the electrodes and not loading hot ions; see Figure (4.6)b] the cooling curve is not run through as far in reverse (the velocities are not increased as much) and the sequence is much shorter. That the length of the cooling sequence is dependent on the amount of heat deposited and the possibility of heat dissipation (number of cooling ions) can be seen in the increasing length of the sequence in part b of the figure: With each load of Xe, Be^+ ions are lost due to evaporative cooling (seen by the decreasing maximum amplitude of the final cooling stage) and therefore the amount of the coolant becomes smaller resulting in a longer time to cool the (assumed) same amount of added Xe^{44+} ions.

4.4 Sympathetic Cooling

Sympathetic cooling is an expression for a special kind of collisional cooling where ions or electrons undergo energy-exchanging collisions with cold, neutral or charged particles. Since the density of neutral particles in Retrap is low the neutral sympathetic cooling mechanism can be neglected. Due to increased charge exchange of HCI with the residual gas at higher pressure, this cooling mechanism is not desired. Collisional cooling in Retrap is exclusively happening between ions. This cooling mechanism is present all the time, as long as the collision rate, is high enough.

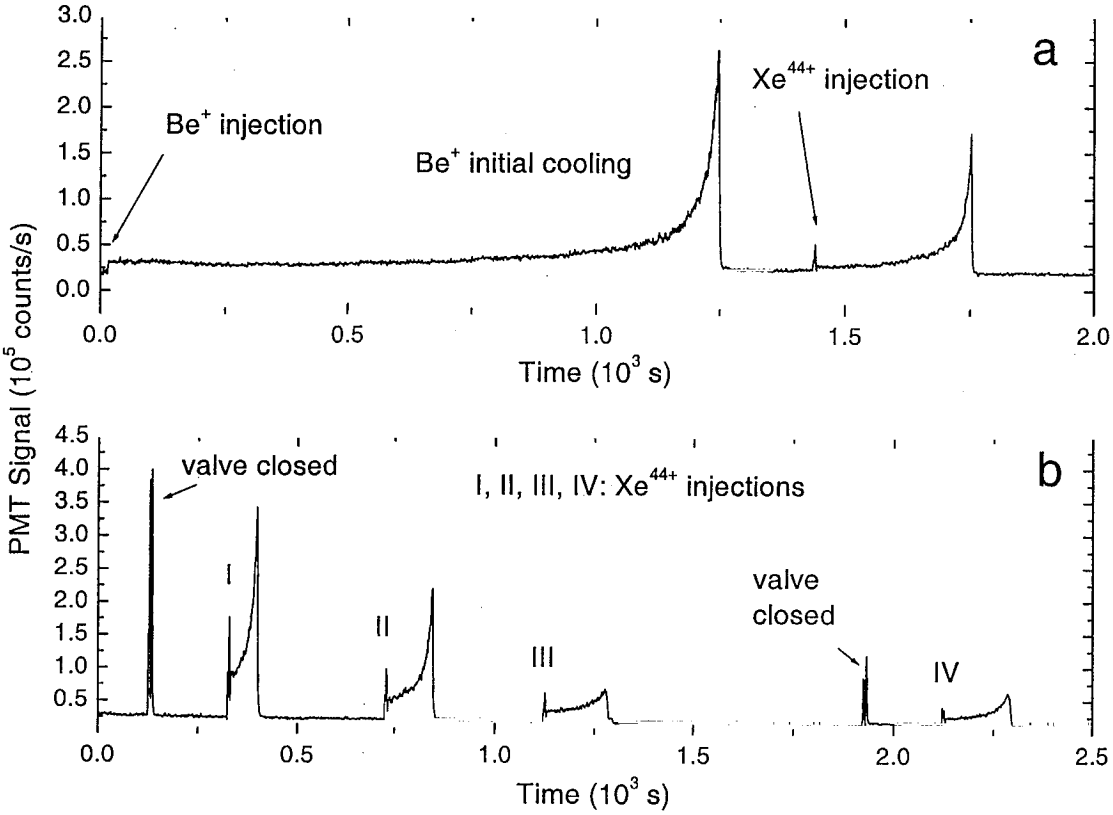

Figure 4.6: a: The PMT signal during the initial cooling process (the 'cooling curve') of Be^+ is shown. After the ions are cold, Xe^{44+} is injected into the trap: the Be^+ ions are heated by the injected hot ions and the cooling curve is being run through in reverse very fast, indicated by the small peak at the time of the injection. A second cooling curve follows the injection. b: Multiple Xe^{44+} injections are shown (I, II, III, IV) and the same phenomenon can be seen: the intensity of the cooling curves becomes weaker and weaker, indicating a Be^+ loss due to evaporative cooling. The two short peaks (marked with 'valve closed') were obtained by going through the Xe injection procedure but a gate valve in the ion beam line was closed and therefore no ions were admitted. The plasma is heated due to the pulsing of certain voltages, but the heat deposition is not as big as it is when hot ions are added to the plasma.

A detailed treatment of energy-exchanging ion-ion collisions can be found in [58]. Here only the relevant results are summarized. The self-collision time, τ_c, gives a measure of how long it takes to substantially remove any anisotropy in the velocity

distribution in a plasma of particles with the mass m, charge q, density n, and close to a temperature T, and establish a Maxwellian distribution of the kinetic energies:

$$\tau_c = \frac{2\pi\epsilon_0^2\sqrt{m}\,(3\,k_B T)^3}{0.714\,n\,q^4\ln\Lambda}\,. \tag{4.22}$$

The factor 0.714 in the denominator of the Equation (4.22) is obtained from a detailed calculation by Chandrasekhar [59, 60], taking into account the motion of the center of mass of the colliding particles and is given here for the case, that the kinetic energy is:

$$E_{kin} = \frac{3}{2}k_B T\,. \tag{4.23}$$

The Coulomb Logarithm $\ln\Lambda$ is given by

$$\ln\Lambda = \ln\left[6\pi\sqrt{\frac{2}{n}\left(\frac{\epsilon_0 k_B T}{q^2}\right)^3}\right] \tag{4.24}$$

and varies for typical laboratory and astrophysical plasmas between 5 and 20. Frequently a value of 10 is used in the literature. If the Coulomb logarithm is calculated to be less than 5 the theory, used to derive Equation (4.24), starts to break down and the equations are no longer valid. The very cold plasmas in Retrap certainly enter this regime, but an adjustment of the theory was not performed.

If two different particle species m, q and m_f, q_f with different temperatures T and T_f are mixed they reach an equilibrium temperature with a time constant τ_{eq}, the equipartition time. In the differential equation

$$\frac{\mathrm{d}T}{\mathrm{d}t} = \frac{T_f - T}{\tau_{eq}} \tag{4.25}$$

this time constant is given by:

$$\tau_{eq} = \frac{\sqrt{18\pi^3}\,\epsilon_0^2\,m\,m_f\,k_B^{3/2}}{n_f\,q^2\,q_f^2\ln\Lambda}\sqrt{\left(\frac{T}{m}+\frac{T_f}{m_f}\right)^3}\,. \tag{4.26}$$

To obtain the order of magnitude for the self-collision times and equipartition times in the Retrap plasmas certain temperatures and (low) densities are assumed and the

following values are calculated:

Be^+ ($n = 3 \cdot 10^{14} \frac{1}{m^3}$, $T = 100$ K) $\tau_c = 20\mu$s,

Be^{2+} ($n = 3 \cdot 10^{14} \frac{1}{m^3}$, $T = 100$ K) $\tau_c = 2\mu$s,

Xe^{44+} ($n = 6 \cdot 10^{12} \frac{1}{m^3}$, $T = 5000$ K) $\tau_c = 800$ ns and

Xe^{44+}+Be^+ ($n_f = n_{Be^+} = 3 \cdot 10^{14} \frac{1}{m^3}$, $T_{Be^+} = 100$ K, $T_{Xe^{44+}} = 5000$ K) $\tau_{eq} = 700$ ns.

The slowest collision processes with these parameters happen in the plasma with the singly charged ions and they become faster as the temperature is dropped and the charge state of the ions in the plasma is increased.

Experimentally, it was not possible to measure any of these collision times to an acceptable accuracy in Retrap, but the important information gained from this treatment is that the collision times are fast compared to other cooling times. However, the effect of the sympathetic cooling could clearly be seen. In Figure (4.7) a series of tuned circuit probes is shown. At first only Be^+ is trapped, then only Xe^{44+} (both have been confined for 2 s in the trap) and then two measurements with both ions in the trap at different times (2 and 5 s) are shown. It can be seen that the more time the two species spend together, the colder the Xe ions get. This is indicated by the possibility to resolve the single charge states. To get a time constant with the above theory for this case, a temperature corresponding to about 100 V$\cdot q$ has to be assumed. This results in 10^6 K for Be^+ and about $5 \cdot 10^7$ K for Xe^{44+}. With the assumption of still the same density $n_f = n_{Be^+} = 3 \cdot 10^{14} \frac{1}{m^3}$ an equipartition time of $\tau_{eq} = 200$ ms is calculated. To extract a time constant from the shown experimental data is in principle possible, but it might not compare to the theoretical value since, in the experiment, a substantial amount of cooling is being done by evaporating Be^+ from the trap. This can be seen in the shrinking of the Be^+ peak in Figure (4.7). Since the Xe ions are much hotter than the Be ions the equilibration temperature should be higher than the initial Be^+ temperature and therefore the Be^+ peak should increase. This is not the case; the peak height decreases, indicating particle loss. The peak building up between the Be^+ peak and the Xe peaks can be attributed to Be^{2+}.

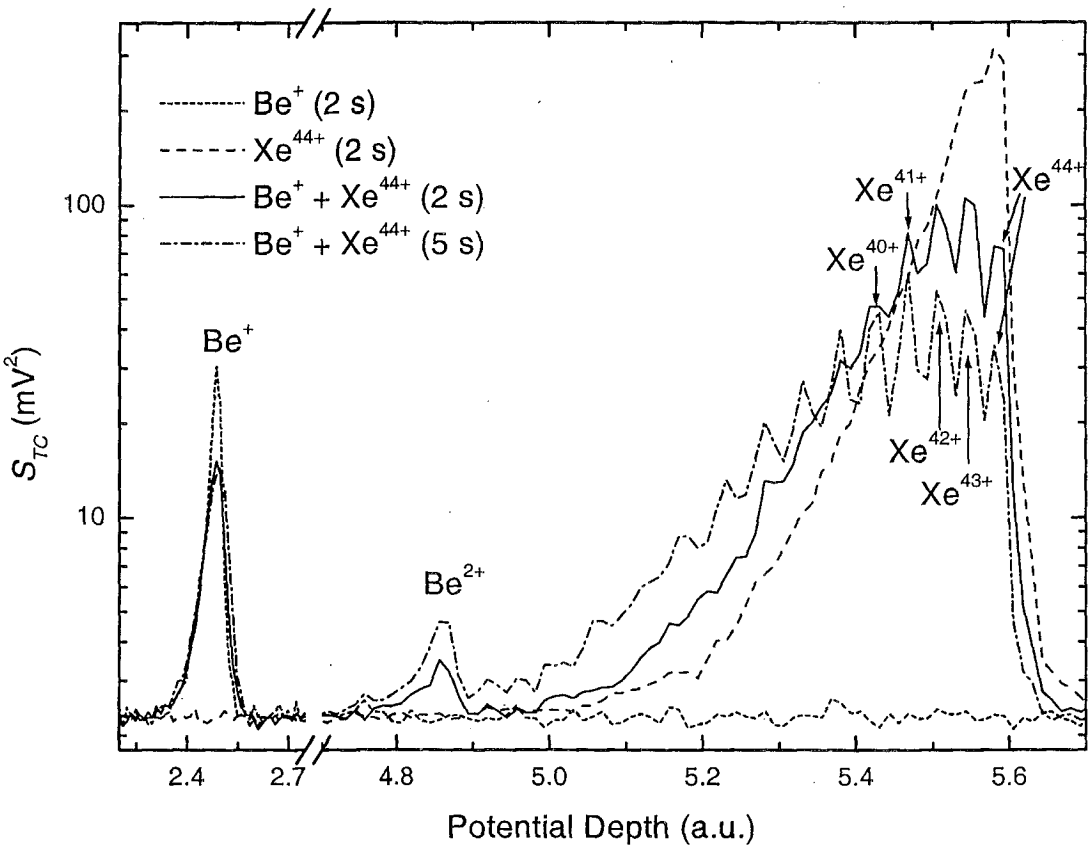

Figure 4.7: Sympathetic cooling of Xe^{q+} by Be^{+}: Tuned circuit signal S_{TC} while the potential well depth is swept. The trap can be loaded with only Be^{+}, only Xe^{44+} or both ion species. In the latter case Xe will be cooled by collisions with the cooler Be^{+} ions, since they have a 44 times lower energy than the Xe^{44+} ions. The possibility of seeing different charge states of the Xe ions indicates such a cooling. Be^{2+} is produced in this initial process due to the introduction of highly charged Xe ions.

It is apparently produced due to the introduction of highly charged ions into the Be^{+} cloud, suggesting the charge exchange reaction

$$Xe^{q+} + Be^{+} \rightarrow Xe^{(q-1)+} + Be^{2+} . \tag{4.27}$$

The charge exchange cross-sections for such collisions at these temperatures are not well known and therefore it is difficult to estimate what the right reaction channel is.

5 Experimental Data and Discussion

In this chapter experiments showing how different ion species can be brought into the same trap volume and how to measure certain plasma parameters as ion species, density, temperature and number of ions are described.

5.1 Trap Loading

5.1.1 MEVVA Injection

A MEVVA ion source loads the trap with Be^+. The MEVVA is mounted in the focal point of an analyzing magnet directly above Retrap making a $\frac{m}{q}$-selection possible [see Figure (5.1)]. A charge selection is necessary since the MEVVA produces a variety of ions. The major constituents of a MEVVA pulse are Be^+ and Be^{2+}. Other ions produced include: O^+, N^+, and O^{2+} [see Figure (5.2)]. The abundance of these species varies, depending on the quality of the vacuum in the MEVVA ion source. In the trap only the major constituents are detected since the amount of the other species is so minimal that the tuned circuit is not able to pick up their signal.

In normal operation Be^+ and Be^{2+} were produced in nearly the same amount. The reliability of a MEVVA as a beryllium ion source for Retrap was often poor: the amount of trapped Be^+ varied from shot to shot over many orders of magnitude. Therefore, a slightly redesigned MEVVA [Figure (5.3)] was tested. Instead of the seven-hole pattern of the regular MEVVA, a single centered hole was used to extract the ions from the source. The trigger electrode (also made out of Be) was made to be as symmetric as possible (in our case the Be wire had a square cross-section).This reduced the total number of extracted Be^+ ions, but increased the reliability of the source. The reason for this seems to be that with the single hole the geometrical source of the ions is better defined: the ions always come from the same spot on the MEVVA; whereas with the seven-hole design the ion extraction seemed to be through different holes at each shot and therefore changing the geometrical location of the ion

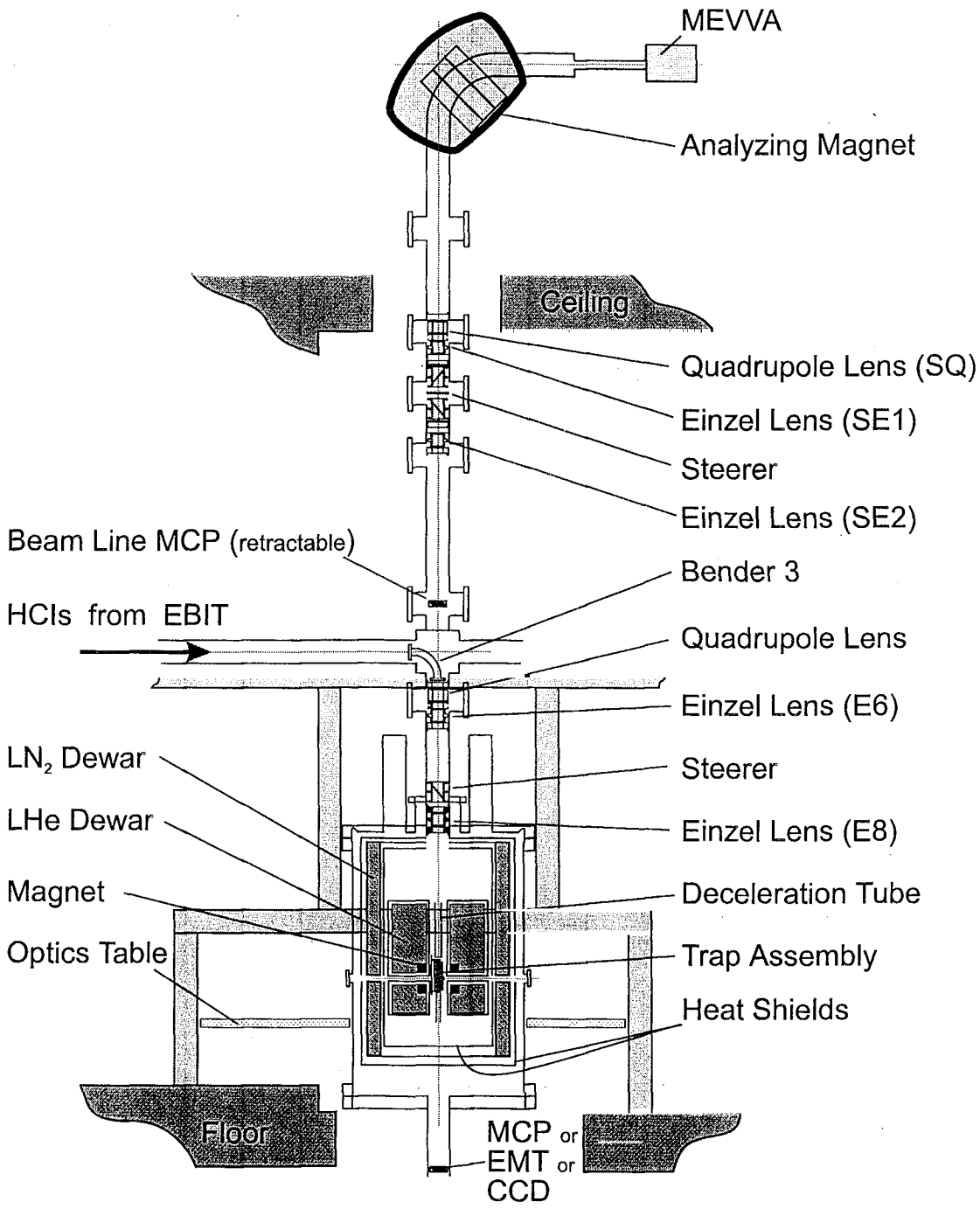

Figure 5.1: Setup to inject MEVVA ions through an analyzing magnet for charge state separation.

source. Apparently, the beamline, with Retrap as a detector, was very sensitive to the geometrical location of the ion extraction.

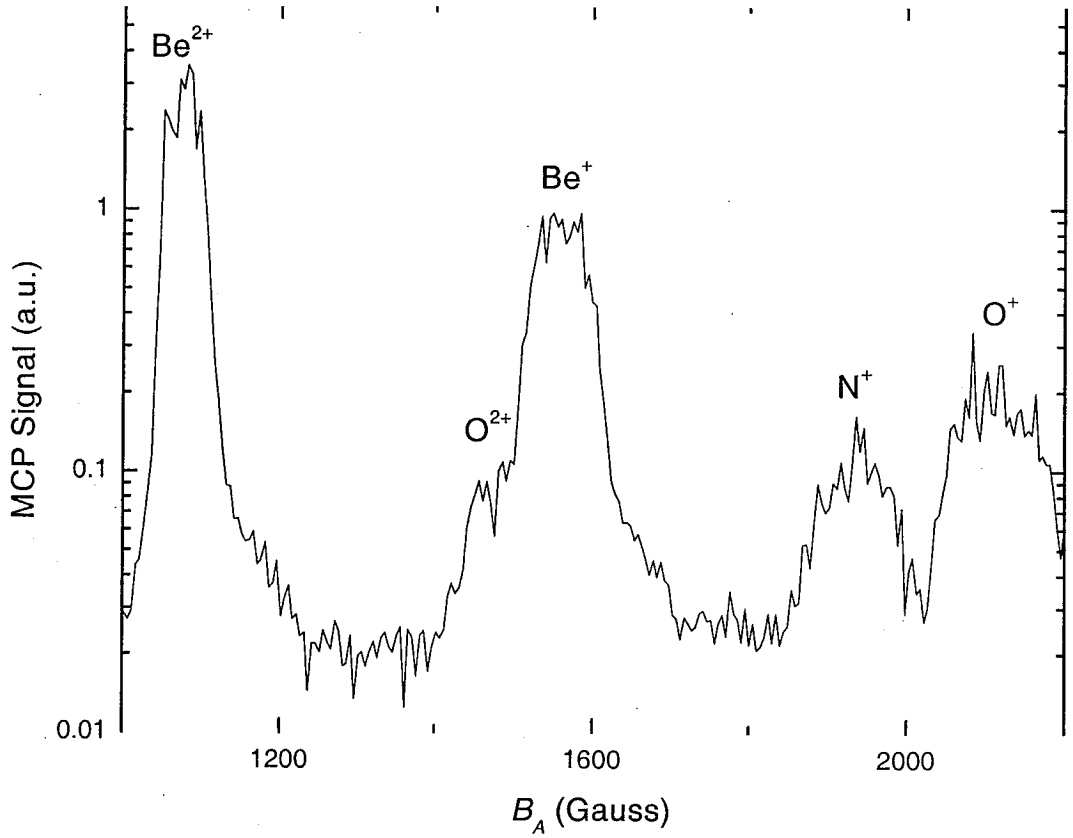

Figure 5.2: Analyzing magnet scan for the MEVVA ion injection. The signal on the MCP as a function of the magnetic field B_A of the analyzing magnet. Without mass to charge separation, all the ions seen on this scan would be trapped.

With the new design it was possible to follow an alignment procedure for the Be-beam:

- All beamline elements and the superconducting magnet are turned off.
- The analyzing magnet is scanned with the beamline MCP as a detector. The MCP was carefully positioned with a telescope in the geometrical middle of the beamline. This ensures that the center of the detected signal corresponds to the beam passing the center of the beamline.
- The analyzing magnet is set to the center of the rather broad peak of the Be^+ [see Figure (5.2)]. This defines how straight the beam is and the analyzing

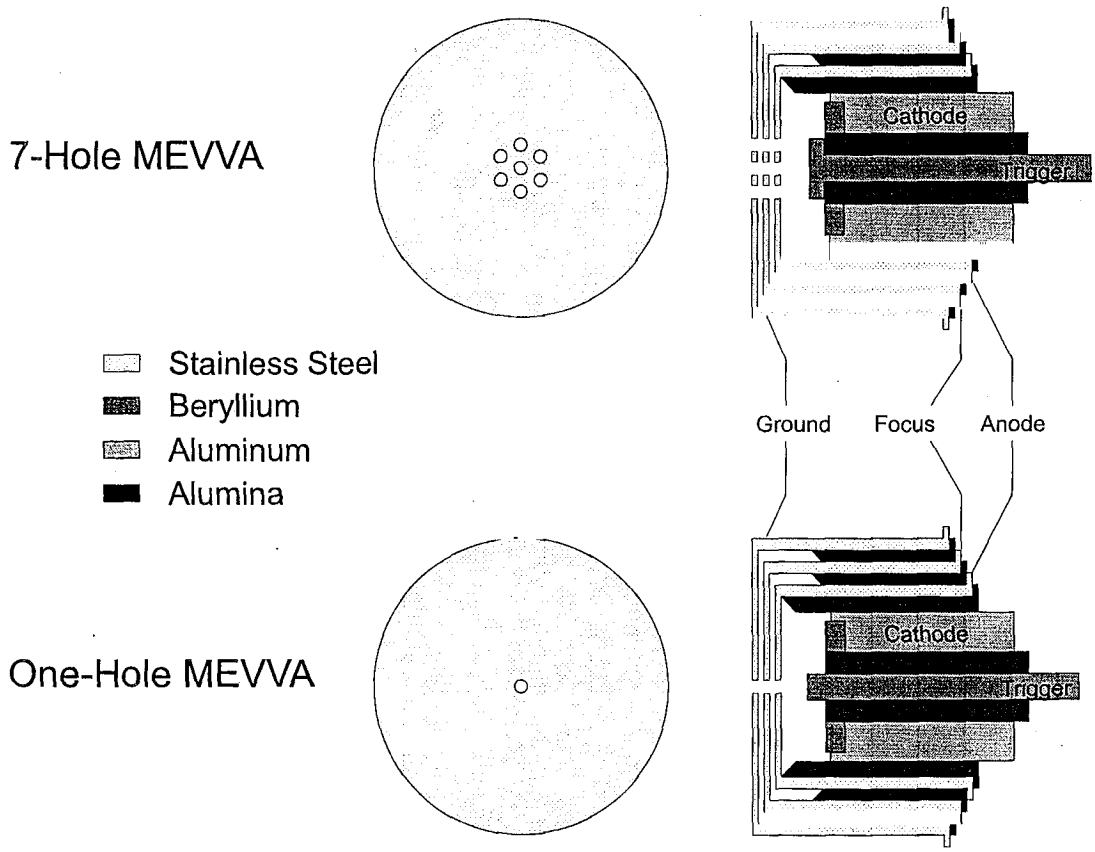

Figure 5.3: Comparison between the traditional "7-hole-MEVVA" and the slightly redesigned "one-hole-MEVVA". In the design with only one hole, the trigger electrode is not shaped as a "T" anymore but rather a square pin. The reliability of the MEVVA as an ion source for Retrap was improved.

magnet will be kept at the set value.

At this point all the other elements in the beamline need to be set, so that the throughput through the trap is maximized. Using the detector under Retrap (MCP or EMT) the following steps are performed:

- Scanning of the voltages on the einzel lenses SE1, E6, the voltage on the top deceleration tube, the voltages on the quadrupole lens SQ (best if off), einzel lens SE2 (best if off) and then the einzel lens E8 maximizes the signal on the detector.

While the superconducting magnet is ramped to the desired value, the signals on different electrodes of the trap assembly can be monitored. The signal on the uppermost electrode, which is the largest with no magnetic field, can be reduced by a factor of 10 and the signal on the bottom detector can be increased by a factor of 2, indicating the funneling property of the main magnetic field.

- If the magnetic field axis does not coincide with the geometrical axis of the trap the signal on the bottom detector is reduced since the ions are not lead straight through the trap electrodes. Maximizing the count rate on the detector by changing the current in the superconducting shim coils should lead to a well aligned magnetic field.

- At this point Be^+ can be trapped, the bottom detector is switched to the counting mode, detecting the trapped and released ions. The ions can also be detected with the tuned circuit.

With this procedure it was possible to obtain a reasonably straight Be-beam through the trap. The deviation of the beam from the ideal path through the center of the beamline is less than 0.1°. It was also possible to compare different signals caused by the MEVVA. In Figure (5.4) four different signals are displayed as a function of time: The MEVVA current signal is the current which is picked up by a current transformer connected to the anode of the discharge electrodes. The signal on the bottom detector was obtained with a MCP in the Faraday mode [see Chapter (2.3.3.3)]. By differentiating this signal one obtains a signal proportional to the ion current in the Be-beam. A signal proportional to the amount of trapped ions can be obtained with the tuned circuit when the whole capture timing pattern is shifted in time over the incoming ion pulse. This signal is also proportional to the temperature of the ions. The ions were captured and held for a certain time and then released from the trap. Finally the number of released ions as a function of when the ions were captured was recorded too. Both signals, the tuned circuit signal and the dumped ion signal, are

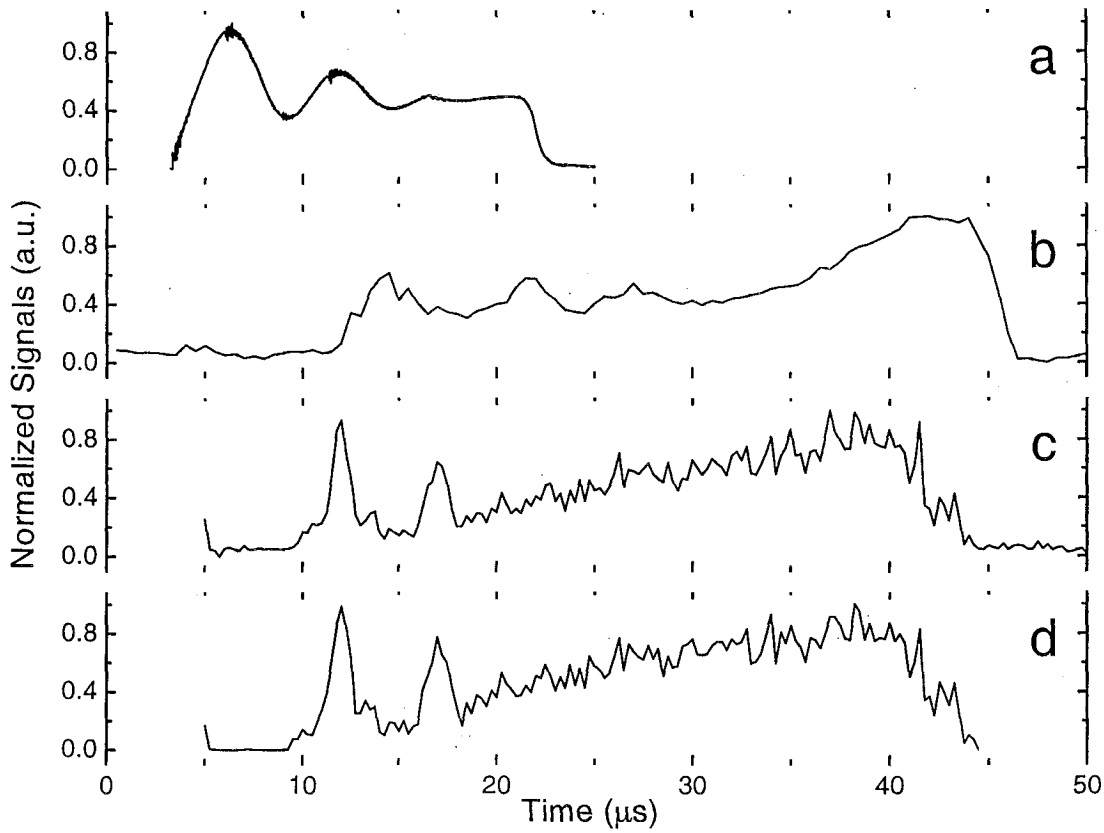

Figure 5.4: Comparison of MEVVA current signal on different detectors. a: The current in the ion source itself; b: the current on a MCP detector underneath Retrap (without trapping any ions); c: the signal on the tuned circuit as the trapping timing is shifted over the ion pulse; d: the amount of trapped ions released from the trap onto the MCP in counting mode under Retrap.

almost exactly the same.

It was noticed that the pulse where the ions are detected directly lasts much longer than the primary current pulse. This is most likely due to the fact, that the driving voltage on the discharge is not being sustained anymore, but there are still ions in the discharge region, which can be extracted.

5.1.2 Highly Charged Ion Injection

To inject EBIT-ions into Retrap, EBIT has to be tuned for maximum extracted ion current and for the lowest possible electron beam current. The low electron beam current ensures that the temperature of the ions in EBIT is as low as possible decreasing the emittance of the beam. If the ion temperature is high, the spread of the ion pulse during the transport to Retrap will be larger. In other words the initial phase space of the ions grows with the temperature.

The HCI beam is tuned with the help of the Faraday cups installed at different positions in the beam line. On each Faraday cup the current of the extracted beam is maximized, then the Faraday cup is retracted and the beam is guided to the next Faraday cup. With the analyzing magnet a specific charge state of an ion can be selected. The relation between magnetic field B_A of the analyzing magnet and the selected ion species with mass m and charge q accelerated by the potential U is given by Equation (2.7). A spectrum of the different ions going through the magnet can be evaluated using Equation (2.7) if one or two species are known. In Figure (5.5) a spectrum of an extracted ^{136}Xe beam is shown. Some charge states of the Xe coincide with some charge states of the residual gas (e.g. oxygen). This leads to higher peaks in the detected current signal helping to identify the peaks. Xe^{34+} and O^{4+} are such a case[7] , as well as Xe^{42+} and O^{5+}.

One ion species is chosen by setting the magnet to the desired value and the beam is be aligned through the rest of the beam line. The last step in the beam tuning procedure is to maximize the beam on the detector under Retrap. The superconducting field has to be ramped up and aligned [see process in Chapter (5.1.1)].

The current signal of a HCI beam hitting a detector under Retrap is shown in Figure (5.6). It can be seen that most of the pulse ($\approx 82\%$) is contained in the first 5.5 μs of the pulse. Once the beam through Retrap is optimized, the trapping of HCIs

[7]Also C^{3+} is on that position, but it might not be in this specific example, since C^{4+} at $\frac{m}{q} = 3$ seems not to be there.

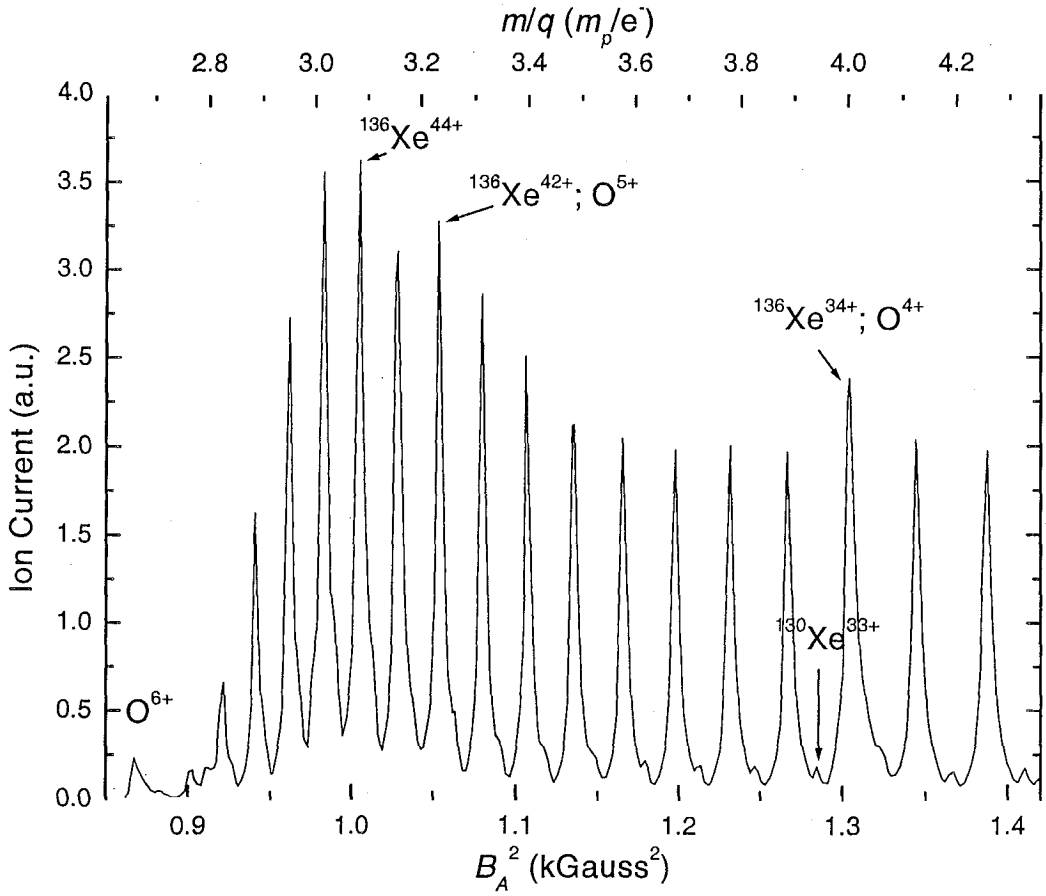

Figure 5.5: Amount of extracted ions as a function of the magnetic field of the analyzing magnet. The series of different charge states of ^{136}Xe can be seen. At $\approx \frac{m}{q} = 4$ both Xe^{34+} and O^{4+} pass the analyzing magnet, increasing the peak amplitude. The smaller peaks between the xenon peaks of lower charge states are caused by a different isotope of Xe.

can be attempted. The most crucial parameters are the deceleration amplitude, the time when the deceleration tube is switched and when the potential on the capture electrode is pulsed to confine the ions. These parameters need to be guessed at first and then adjusted until the caught ion signal is maximized. The tuning process has to include all the other beamline elements. Initially it is necessary to use the most sensitive 'catch and dump' particle detection technique, but at higher count rates the tuned circuit can be used as well.

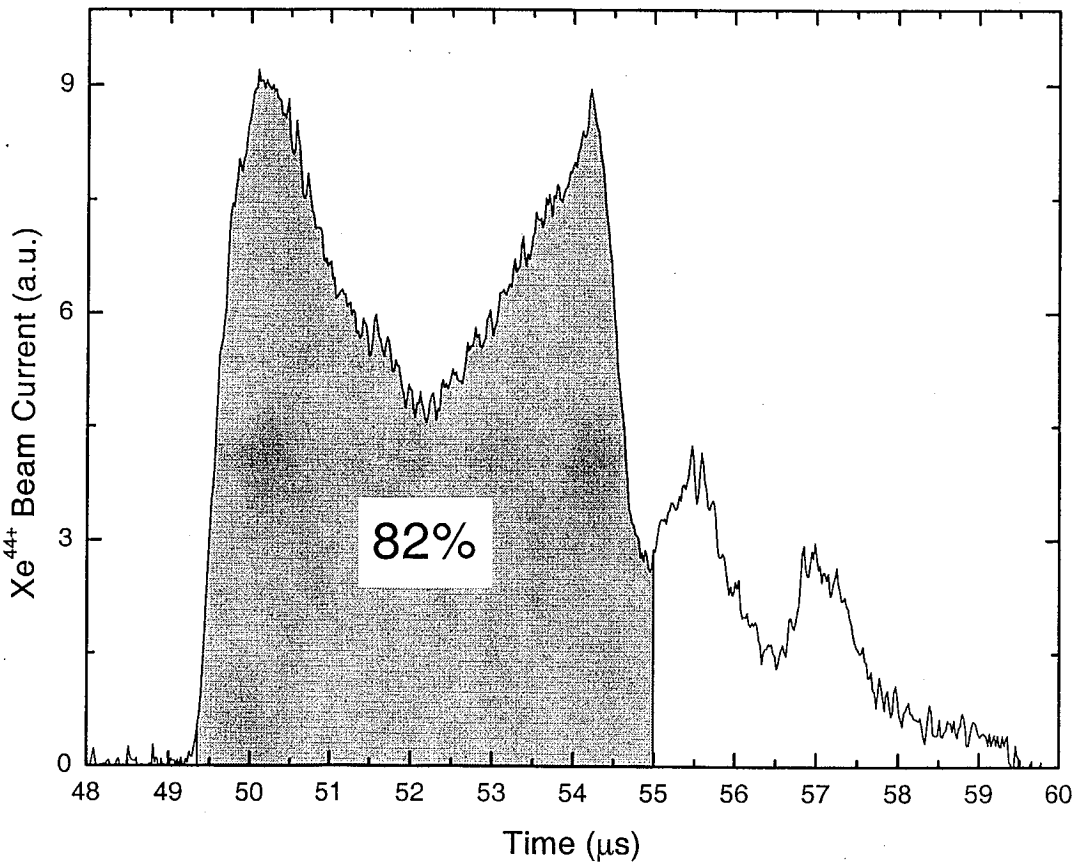

Figure 5.6: Current pulse of extracted Xe^{44+} ions. The first 5.5 μs contain about 82% of the whole pulse.

An example of a tuned circuit signal is shown in Figure (5.7). If nothing is done to cool the ions in the trap, the signal will in general not be symmetric. The ions with higher kinetic energy have a bigger axial amplitude and can therefore oscillate out of the region where the electric potential is quadratic. In this trap the non-quadratic regions have a lower potential than the ideal quadratic potential. This causes the ions to oscillate with a lower frequency than the ones with lower kinetic energy. To get them on resonance with the tuned circuit, the potential difference between the ring and the endcap electrodes has to be increased. This is the reason why the peak of the Xe^{44+} in Figure (5.7) has a tail on the side with the higher potential. To get rid of this tail, the ions have to be either cooled or the hot ions have to be released

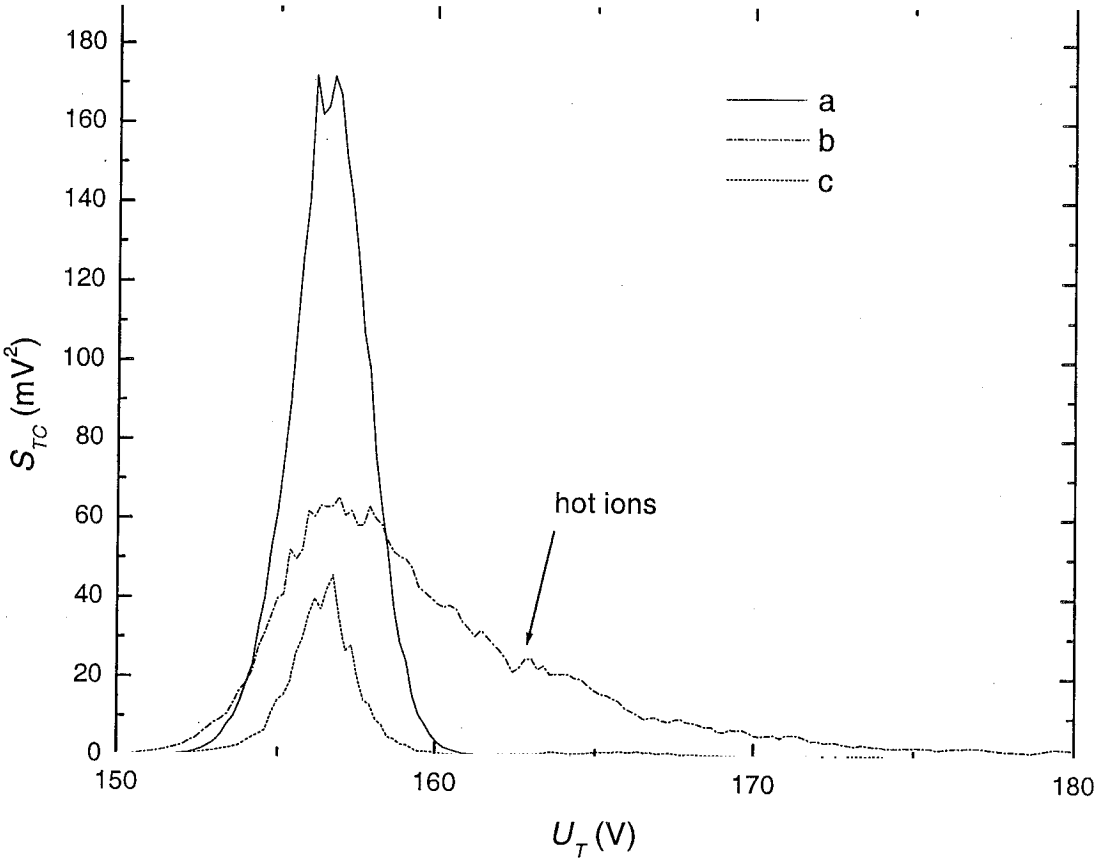

Figure 5.7: Example of a tuned circuit signal S_{TC} as a function of trapping voltage U_T for ions prepared in different ways. a: A predump right after capture gets rid of all particles which are axially hot but the radial temperature might still be high. If the system is given enough time after the predump to equilibrate then the radial kinetic energy is distributed to the axial as well (b). c: The system is equilibrated before the predump and then it is given some time to equilibrate again. It does not spread anymore indicating equal temperature in the axial and radial degrees of freedom.

from the trap (predump).

5.1.3 Merging Two Ion Species in One Trap

To cool HCIs to temperatures much below 4 K it is necessary to apply a cooling scheme beyond the resistive cooling of the ions. Since HCIs do not have strong

E1 transitions in a laser-accessible range, direct laser cooling is a very ineffective technique. A more effective technique is a sympathetic cooling scheme [see chapter (4.4)] with laser cooled Be^+ ions. A necessary condition for this scheme to work is that both species, the HCIs and the laser cooled ions are brought into the same trap volume. Many schemes were studied, but here only two types are described. In the first type of schemes, the transfer schemes, HCIs and laser cooled ions are trapped in different traps and are then merged into the same volume. This turned out to be ineffective. In the second, more successful scheme, HCIs are directly captured into the same trap that the laser cooled species is trapped.

5.1.3.1 Transfer Scheme The trap assembly for this experiment consists of two consecutive hyperbolic traps [see Figure (5.8)]. The first is called the top trap and the second one the bottom trap. Both traps are identical with the only difference that the bottom trap is equipped with ports for laser access whereas the top is not. Both traps have a tuned circuit attached to the endcap electrodes which makes resistive cooling [see chapter (4.2)] and nondestructive ion detection feasible.

At first Be^+ ions are loaded into the bottom trap, where they can be cooled resistively and/or with a laser. All the bottom trap electrodes are biased with a few hundred Volts (typically +200 V) with respect to the top trap. At the end of the cooling cycle of the Be^+ the harmonic potential well in the bottom trap is made shallow (potential difference between the ring electrode and the endcap electrodes is $\approx$ 10 V). In the meantime, HCIs had been loaded into the top trap. At this point the transfer is being started by raising the potential on all the electrodes of the top trap slowly (on a time scale of seconds) to match the bias potential of the bottom trap. During this process the most energetic ions will first have enough energy to leave the region of the top trap and will start oscillating over the whole length of both traps, colliding with the cold Be^+. Since these ions will at first barely have enough energy to climb out of the top potential well, they will have a low kinetic energy and therfore have a

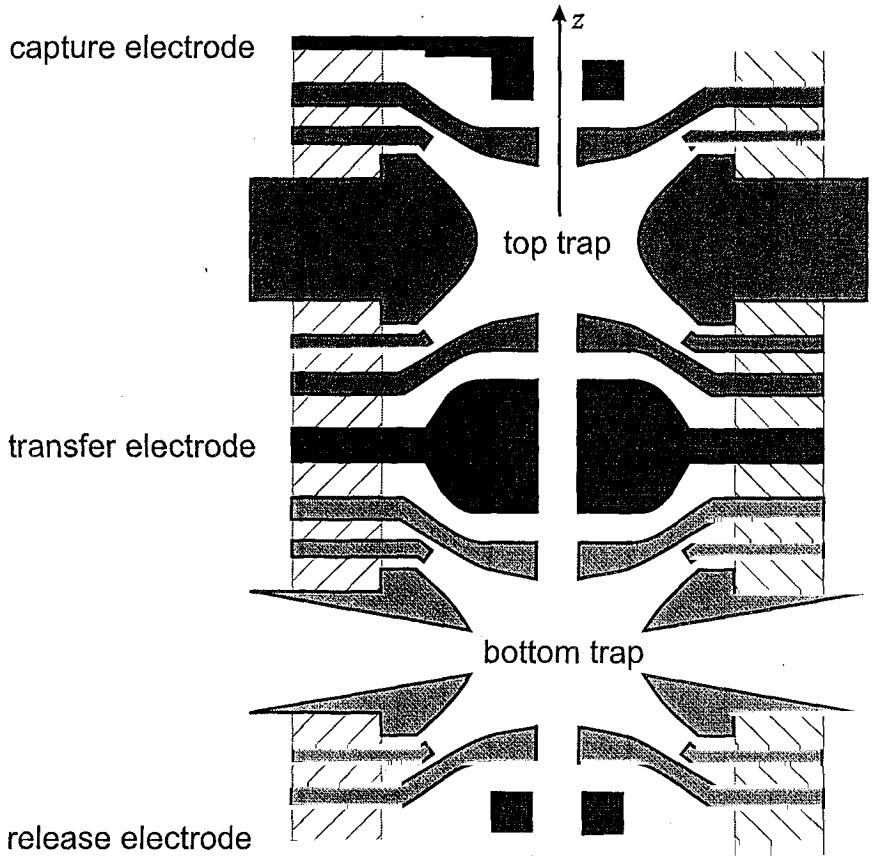

Figure 5.8: Assembly of two consecutive hyperbolic traps for ion transfer schemes. Both the top and the bottom hyperbolic trap are equipped with a tuned circuit to detect the trap content nondestructively, but only the bottom trap has viewports for laser access.

high collision rate with the cold Be^+. The collisions with the Be^+ will further reduce their kinetic energy forcing them eventually to be confined in the shallow potential well of the bottom trap. Once the top bias potential matches the bottom all the HCIs should be trapped in the bottom trap. This transfer scheme has the advantage that HCIs are transferred with a relatively low axial kinetic energy into the cold Be^+ plasma and high energy collisions will not take place.

However, with this scheme only a few ions could be transferred in the experiment. The reason for the poor performance is believed to be the absence of a radial electric field in the transfer, which might cause the ions to drift to the electrodes and be

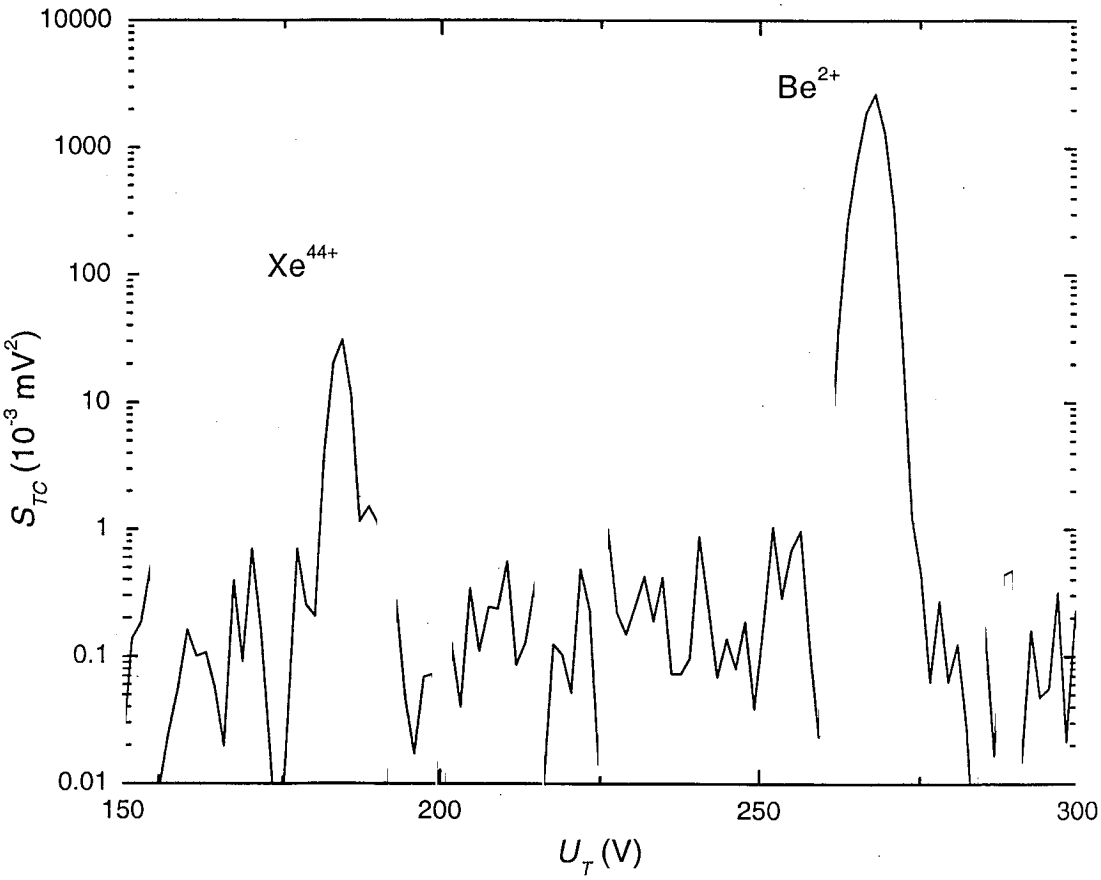

Figure 5.9: Tuned circuit signal S_{TC} as a function of trapping voltage U_T after Xe^{44+} has been transferred from the top trap to the bottom trap.

lost. This is a inherent problem with this trap, since both endcap electrodes are connected by the tuned circuit and therefore can only be ramped together. With electrically separate electrodes steep gradients in the electric field could be maintained and particle loss could be avoided.

5.1.4 Stacking Ions

A rather unsophisticated scheme with only one trap turned out to be the most successful merging technique: First Be^+ ions are loaded into the trap, and cooled resistively or with the laser. Then the trap is made shallower; a voltage difference of about 20–100 V is maintained between the ring and the endcap electrodes. At this point

a HCI capture sequence is run through. Most of the Be^+ can be kept in the trap (the colder they are the more likely they will stay in the trap). To trap HCIs all the elements in the beam line as well as the timing of the pulsing needs to be adjusted to be tuned for the desired species (each species has its own set of tuning parameters). This adjustment was automated, and it was possible to repeat Be^+ and then Xe^{44+} capture cycles many times without retuning any of the parameters.

This technique can be applied to either add HCI to cold Be^+ ions or to increase the trapped Be^+ ions by adding more Be^+ ions (stacking). In Figure (5.10) the PMT signal is shown for many capturing cycles (a). The first cycles do not show a very distinct pattern, but already the fourth stacking cycle shows an exponential-like cooling curve with a time constant of $\tau_C = 13(1)$ s and a maximum scatter rate at the time of the merge of $R_0 = 5 \cdot 10^5 \frac{\text{counts}}{\text{s}}$ [see (b) and (c) in Figure (5.10)]. The initial scatter rate increases with each cycle, indicating an increasing number of trapped Be^+ ions. At the same time the cooling time decreases from about 15 s to about 1.5 s. This indicates that more (cold) ions are in the trap and the ratio of cooling ions to ions to be cooled becomes larger. Potentially also the collision rate increases due to the lower average temperature.

The data in Figure (5.10) is showing a trend rather than an exact measurement. The time resolution (1 s) in the data taken is too poor to deduce more than a trend. The poor time resolution is also the reason for the large error bars in the figure. For any of the following measurements the trap was loaded with typically 2–5 stacking cycles. This was a compromise between number of ions trapped and time it takes to load the trap.

5.2 Lifetime Measurement

There are two ways for measuring the lifetime of HCIs in Retrap: the number lifetime method and the lifetime of a specific charge state. Each method gives answers to different questions.

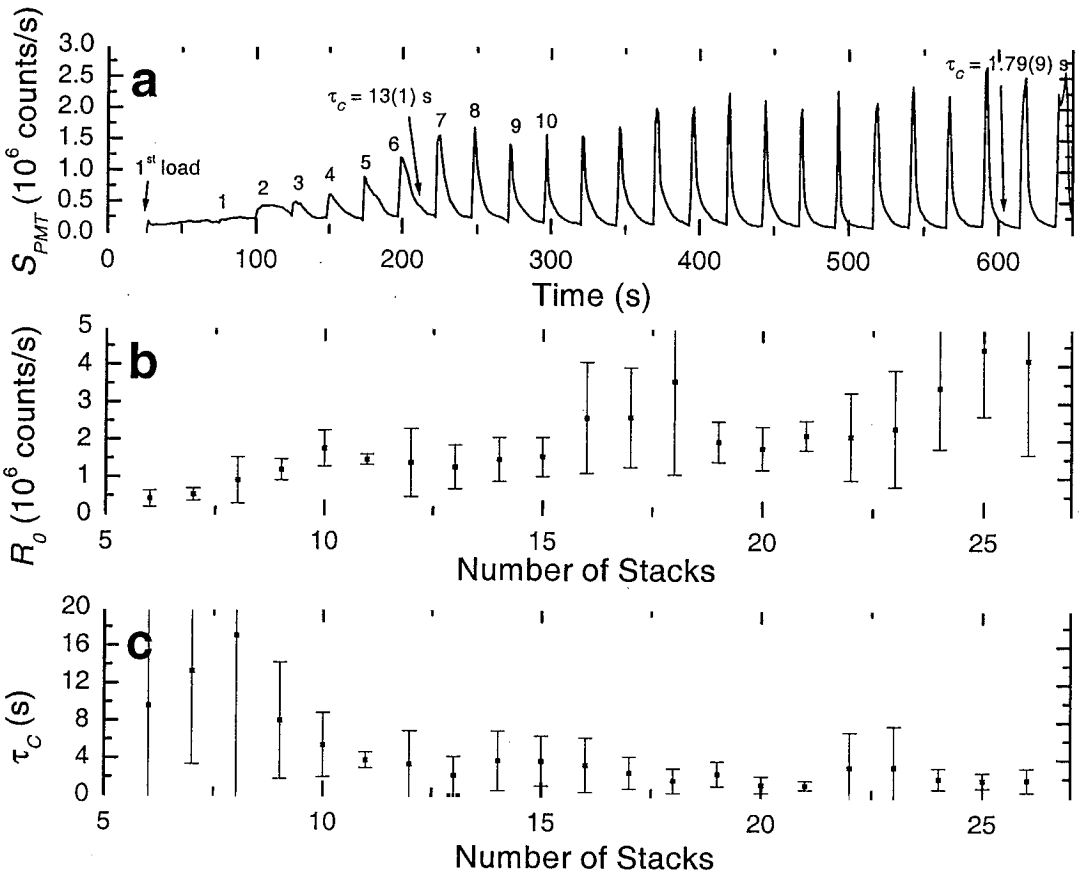

Figure 5.10: Demonstration of stacking of Be^+ ions. a: The trapped ions are heated every time new, hot ions are added to the trap, causing the scatter rate S_{PMT} to increase. b: The maximum scatter rate R_0 in each loading cycle is proportional to the number of ions in the trap. It can be seen that there is an increasing trend with every additional load and c: the time τ_C needed to cool the additional ions decreases since the amount of cooling ions relative to the ions to be cooled increases.

5.2.1 Number Lifetime

This method consists of capturing the ions in the trap, holding them for a certain time t_D and then releasing them onto a detector in counting mode. Since each ion causes a pulse on the counting detector, this method counts all the different species of HCIs in the trap in the same way (The detection efficiency of a EMT is weakly dependent on the charge state [61], therefore, it can be assumed to be constant for adjacent

charge states in HCIs). Charge exchange mechanisms cannot be detected. This is the preferred method if a overall particle loss is of interest, but the interpretation is not necessarily unambiguous. The number of detected ions can decrease or increase over time. The increase can be generated by charge exchange of HCIs with the residual gas:

$$HCI^{q+} + H_2 \rightarrow HCI^{(q-1)+} + H^+ + H\ , \tag{5.1}$$

which increases the number of ions. However, the detection efficiency for H^+ (20%) is much lower than the detection efficiency for Xe^{44+} (80%).

A detected decrease can have multiple reasons:

1. Evaporative cooling can take place, ejecting ions from the trap while cooling the remaining ions.

2. The cloud expands due to imperfections of the trap [62] and particles will be lost to the ring electrode.

3. The cloud expands, becomes bigger than the aperture in the endcap electrode and is scraped off in the release process.

4. Due to the decreasing magnetic field on the way to the detector, the cloud expands, because the ions tend to follow the magnetic field lines. The size and the position of the detector limits the detection to particles coming from a restricted area within the trap.

The described mechanisms are not easy to distinguish and therefore, only the sum of all the effects can be seen.

A typical signal of HCIs is shown in Figure (5.11). Many of such data series have been recorded for different traps and trap-combinations and for different conditions. All the measurements show similar signatures: A rapid decay is observed at early times and it slows down for later times. The data fits rather well to a double exponential decay. The two time constants resulting from these fits ranged from 11 ms to

1.4 s and from 95 ms to 53 s. The mean value of the short time constant is about 400 ms. Since no increase is seen in the measurements, the production of low charge state ions seems to be a negligible process. The dominating process is particle loss and/or cloud expansion. The agreement between the fit and the data might indicate evaporative cooling [see Chapter (4.1)]. But equilibration processes in the trap happen on a short time scale and can also cause ion ejection and cloud expansion. If ions are injected with a high cyclotron energy that energy will be distributed over all degrees of freedom and can cause the axial energy to increase, enhancing the evaporative cooling process.

The results for such measurements with Be^{+} and Be^{2+} are similar, reinforcing the conclusion that the decrease in detected number of particles is mostly due to evaporative cooling and cloud expansion, since Be^{+} does not have any significant charge exchange with the residual gas and it can be kept in the trap (once equilibrated) for days.

5.2.2 Lifetime of One Charge State

A way of measuring the lifetime of one charge state in Retrap is the tuned circuit method. It offers two major advantages:

1. All the ions in the trap can be detected (cloud expansion is less relevant) however, the mass to charge ratio has to be smaller than 10 since the voltage difference between the endcap electrodes and the ring is limited to 600 V.

2. On the tuned circuit charge states can be resolved and therefore, lifetimes for each charge state can be obtained.

The disadvantage of this detection method is that the signal is not only proportional to the number N of ions in one charge state but also to the average axial kinetic energy $\langle E_{kin} \rangle$ of these ions [see Equation (2.36)]. If the ions are cooled by some mechanism during a lifetime measurement the signal will decrease leading to an interpretation of

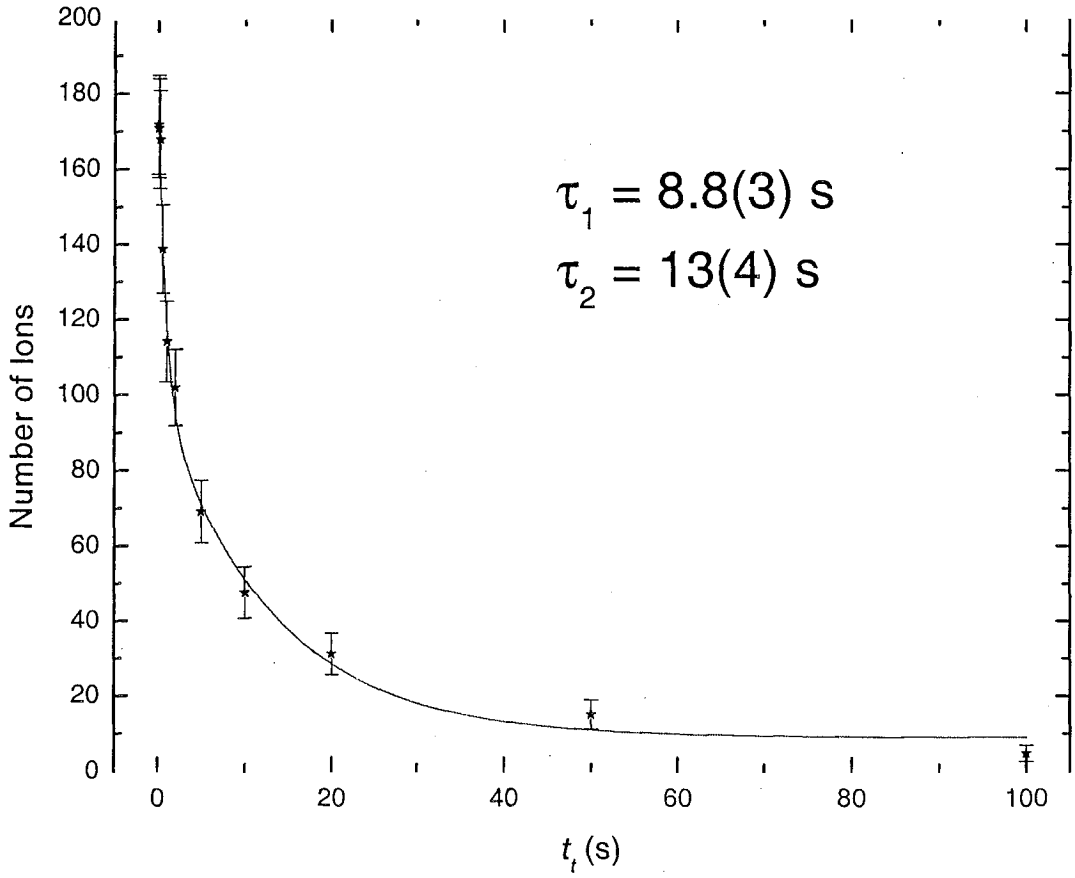

Figure 5.11: Measurement of the number of detected Xe ions N_{Xe} when released from the hyperbolical trap after a variable trapping time t_t. The decay of ions in the trap fits a double exponential indicating ion loss due to evaporative cooling.

particle loss. Measuring the trap content means tuning the ions on resonance with the tuned circuit. This will also cool the ions. The cooling can be neglected if the time the ions are on resonance for detection is much shorter than the cooling time [see Chapter (4.2)]. Typical detection times are in the order of 10 ms and therefore, cooling can be neglected for lower charge states. However, the higher the charge state the shorter the cooling times and the more cooling effects will influence life time measurements.

The lifetime of the HCIs varied drastically over time. The reason for the variations was the change of pressure of the residual gas. Since the trap itself is cooled with

liquid He the electrodes are at 4.2 K and H_2 is adsorbed until the whole surface is coated with a monomolecular layer. This causes the pressure of H_2 in the trap volume to rise and drops the life time of HCIs drastically. To regenerate the vacuum, the trap is moderately heated (all the liquid He is removed from the dewar and room temperature He gas is blown through it). This causes most of the hydrogen to be desorbed from the inner surfaces of the trap and the life time of HCIs is again longer. However, a roughly constant stream of H_2 originating in the warmer regions of the vacuum vessel is flowing into the trap volume and will eventually cover the electrodes again. The pressure in the trap will deteriorate over time. Typically after one week of cold operation the lifetime of the HCIs deteriorated to a few seconds [see Figure (5.12)] and the vacuum had to be regenerated. After such a regeneration process the lifetime was typically in the order of 100 s. In Figure (5.13) a measurement with an extraordinarily long lifetime is shown. Due to the long lifetime, measurements at only three different times were performed and therefore, the error for the lifetime is rather large. However, it is possible to see that the lifetime of the Xe^{44+} ions in this case was in the order of 2000 s.

In order to get such data, the ions need to be prepared. Right after the catch, the ions are hot and need to be cooled to obtain a clean signal. The cooling technique used for the data in Figure (5.12) was to enhance evaporative cooling by applying a predump. The scheme is described in Figure (5.14). The hot ions are released from the trap by lowering the potential on the dump electrode almost to the same potential of the ring and endcap electrodes. The potential difference between the ring potential and the catch electrode potential is typically in the order of 10 V. After this preparation single charge states of the HCIs can be resolved [$t_R = 0$ in Figure (5.12)] and the decay and build-up of individual charge states can be detected by inserting a variable waiting period of t_R between the predump and the detection. A slightly different scheme is described in Figure (5.15) and was used to obtain the data in Figure (5.13). In this second scheme a resistive cooling period is inserted

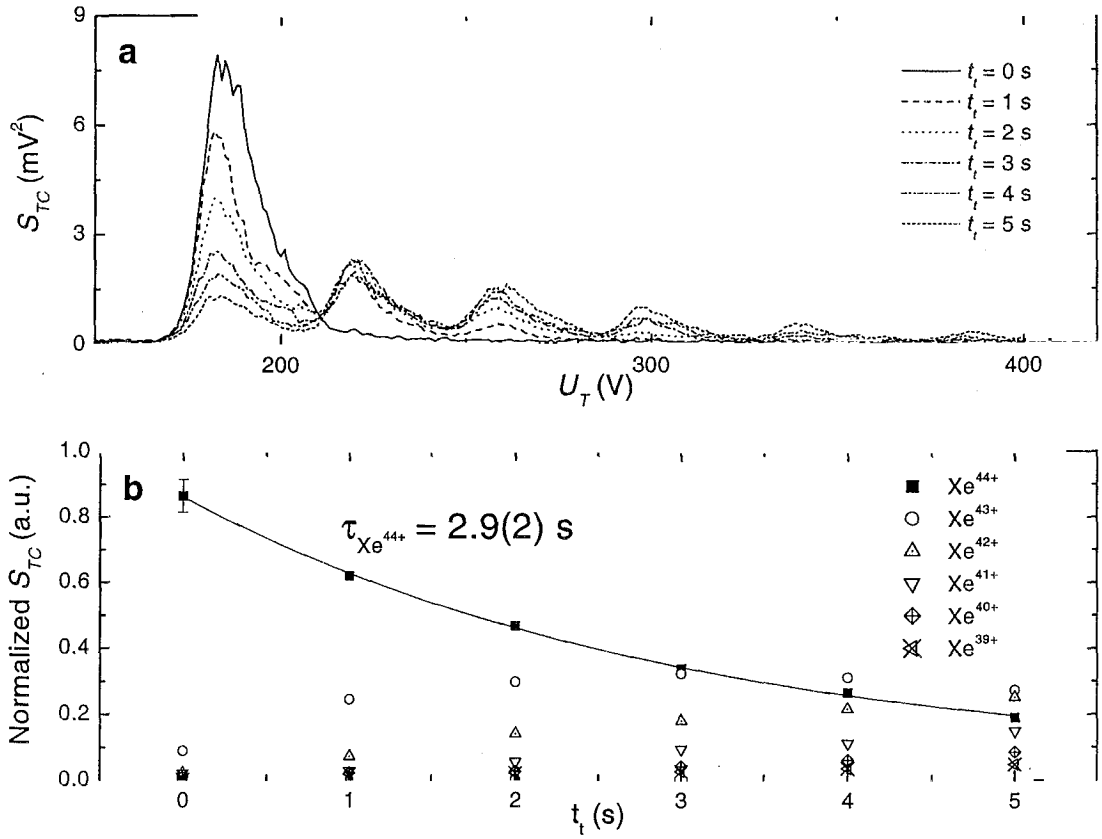

Figure 5.12: Lifetime measurement of Xe^{44+} using the tuned circuit. a: Tuned circuit signal S_{TC} as a function of trapping potential U_T at different trapping times t_t; b: extracted signal for each ion at different times normalized to a constant total signal. The solid line is a fit of the number of Xe^{44+} ions in the trap to an exponential dacay.

before the predump. The potential on the ring electrode is ramped to where the injected ion species (here Xe^{44+}) is on resonance with the tuned circuit, therefore, resistively cooling the ions on resonance. The hot ions will not be resistively cooled since they are not on resonance, but they may collide with the colder resonant ions and be sympathetically cooled [see chapter (4.4)]. After a certain time a predump is performed which ejects the hottest ions and then an additional cooling cycle is added to insure all the ions have a harmonic motion. The advantage of inserting a resistive cooling period before the predump is that more ions will be cold and less ions will

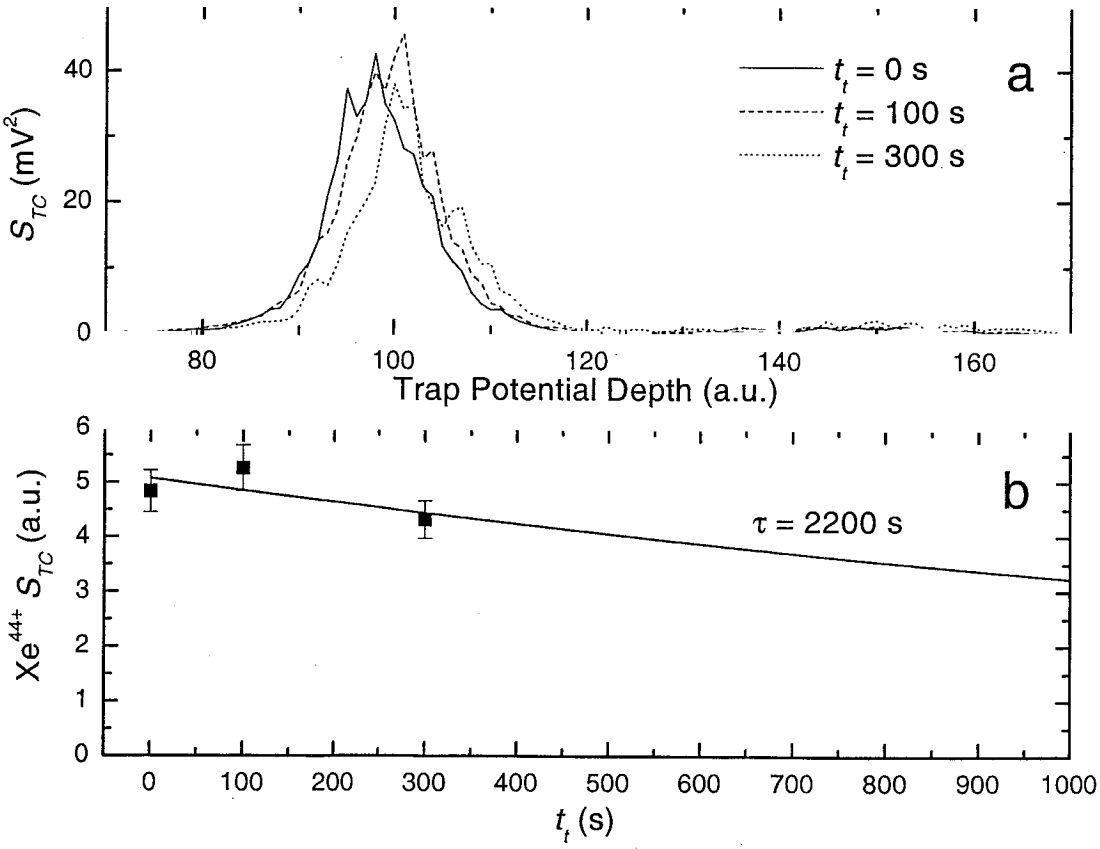

Figure 5.13: Lifetime measurement of Xe^{44+} with the tuned circuit. a: Tuned circuit signal S_{TC} at different trapping times t_t. b: Extracted tuned circuit signal for Xe^{44+} at different times.

be lost in the predump. After the last cooling cycle the ring potential is detuned slightly so that the ions are off resonance and a variable waiting time t_R is inserted. In the case of the data in Figure (5.13) with a Xe^{44+} lifetime of 2200 s the number of released ions after each measurement was counted to be $\approx$ 70 ions per load. This number did not depend on t_R.

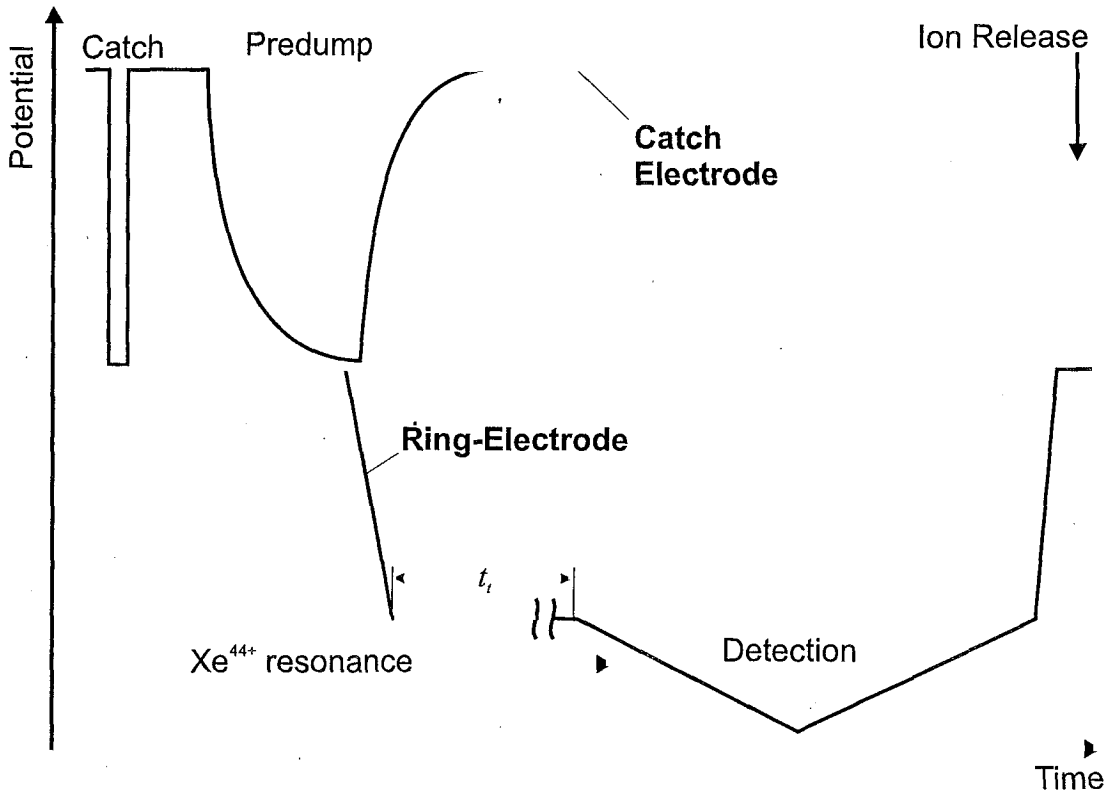

Figure 5.14: Pulsing and ramping scheme for the voltages on the catch and the ring electrodes to perform a lifetime measurement with a predump. The voltage on the endcap electrodes was constant and the trapping time t_t was varied.

5.3 Plasma Parameters

5.3.1 Ion Number

The number of ions caught depended crucially on the tuning of EBIT and all the beam line elements. The trapping efficiency is estimated as follows. First the capture of HCIs, i.e. Xe^{44+}, is investigated. After tuning EBIT and the beam line the signal on the bottom detector was $U_B = 2.75$ V. In Figure (5.16) an average signal on the bottom detector is shown. The measured RC-time was $\tau_{RC} = 84(7)$ μs. The resistor R was given by the input impedance of the amplifier (1 MΩ) and the capacitance was calculated to be $C = 84(7)$ pF. The gain of the amplifier was 200. Therefore, a total charge of $Q_B = 7.2(6) \cdot 10^6$ e$^-$ was detected if, on average, each Xe^{44+} ion produces a

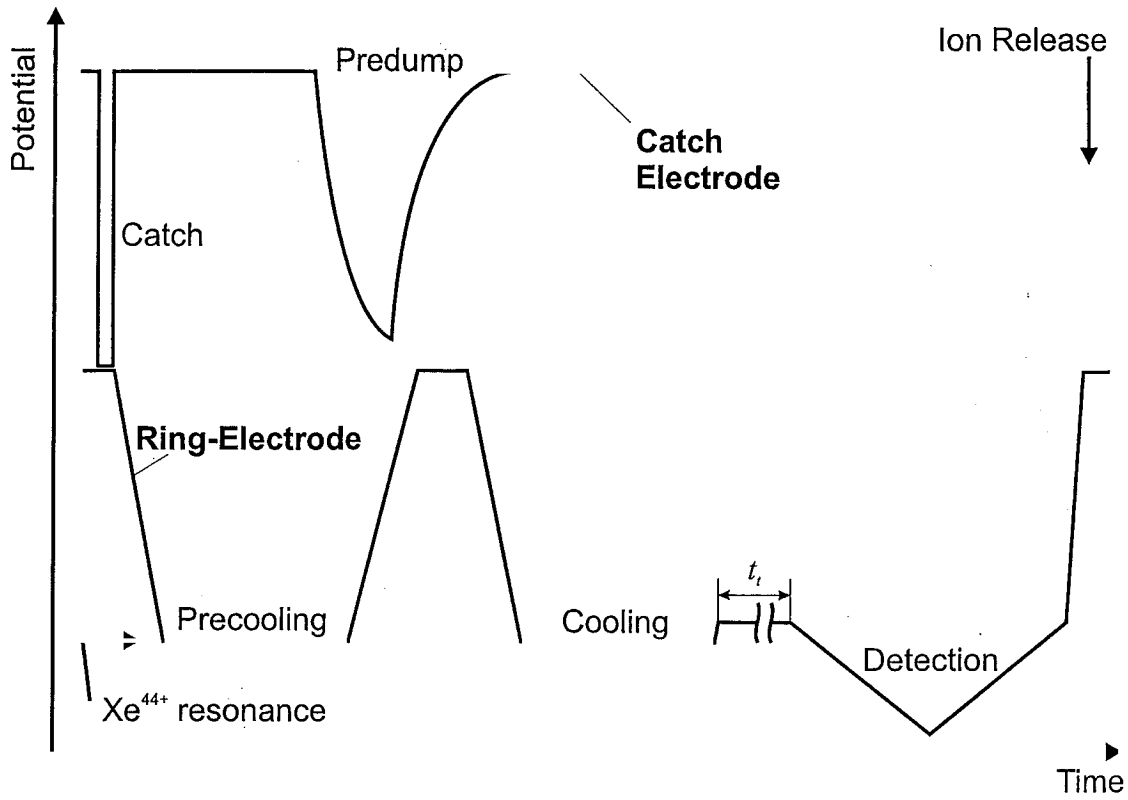

Figure 5.15: Pulsing and ramping scheme for the voltages on the catch and the ring electrodes to perform a lifetime measurement with a precooling cycle to minimize the ion loss in the predump. The voltage on the endcap electrodes was constant and the trapping time t_t was varied.

charge of ≈ 120 e^- (charge of Xe^{44+}+ 75 emitted secondary electrons per HCI impact [63, 64, 65]) and a pulse length of 6 μs is assumed [see Figure (5.6)], an ion current of 10^4 Xe^{44+} ions per μs was detected. The potential difference between the extraction potential and the deceleration potential was 200 V and therefore, about 1.4 μs of the incoming pulse are decelerated in the deceleration tube with an effective length of 15 cm. Thus, there are about $1.4 \cdot 10^4$ ions available for catching. The ions caught in the trap were held for a short time, to avoid evaporative cooling and cloud expansion, and then released onto the bottom detector in counting mode. The result was 230 Xe^{44+} ions per dump. The efficiency of the detector is about 80% for these ions. We assume that all the ions in the trap are hitting the detector, therefore, about 290 ions

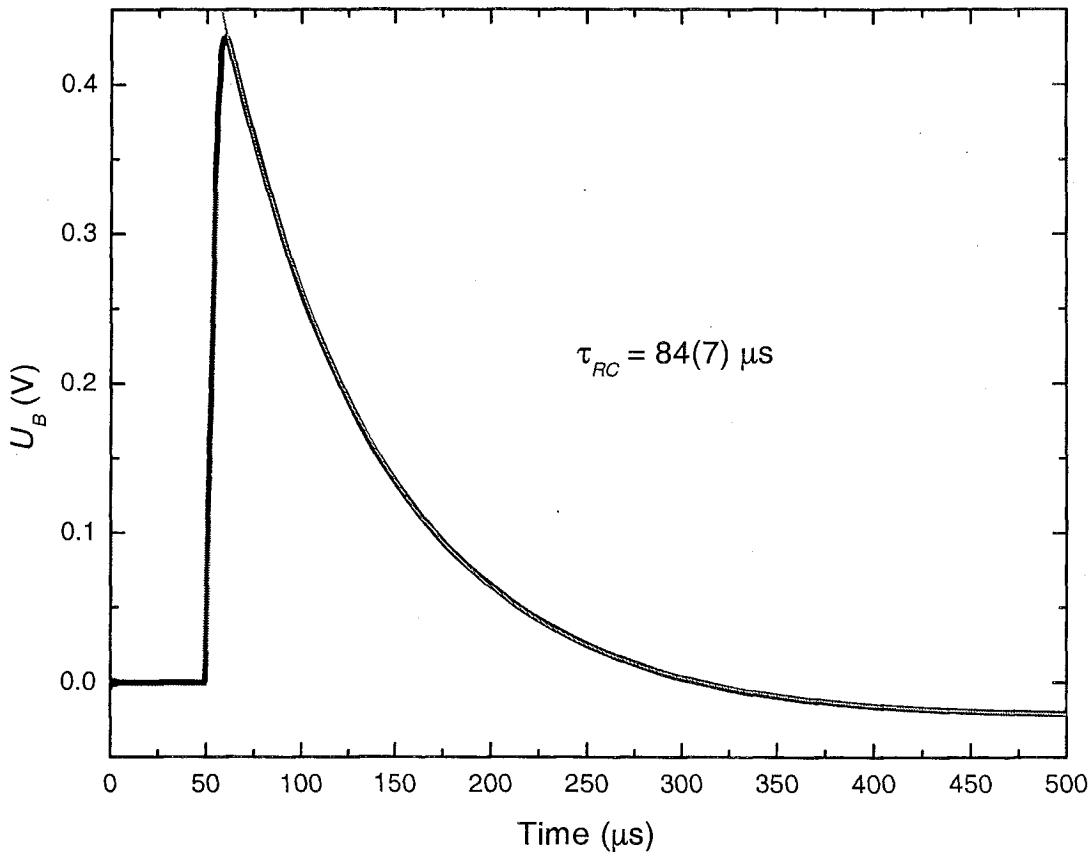

Figure 5.16: Xe^{44+} signal on bottom detector U_B. An exponential is fit to the data to extract the RC-time τ_{RC}.

were released from the trap. This yields a trapping efficiency of $\epsilon_t = 2.1\%$.

In the case of Be^+ no amplifier is needed to detect the signal on the bottom detector. The RC-time is $\tau_{RC} = 1.23$ ms. The input impedance of the scope is $R = 10$ MΩ and the detected signal height is 132 mV resulting in a capacitance of $C = 1.23$ nF and a total charge of $Q_B = 10^9$ e^-. Assuming an average charge of 10 e^- per ion impact [66] was detected and the pulse was 30 μs long [see Figure (5.4)], the number of ions going through the trap was 3.3 10^6 per μs. The fraction of decelerated ions due to the difference of deceleration potential and extraction potential is 2.2 μs of the incoming pulse. Therefore, potentially $7.3 \cdot 10^6$ Be^+ ions can be caught. The ions actually captured are determined from laser measurements and are typically in the

order of $5 \cdot 10^4$ [see chapter (5.3.3)]. With these numbers a capturing efficiency of $\epsilon_t = 0.7\%$ is calculated.

The error on the calculated efficiencies is rather large (in the order of 50%) since only estimates can be given. Therefore, the efficiencies for HCIs and for Be correspond pretty well indicating that the capture was limited mostly by the setup of the trap and not by the condition of the beam. The reason for the low efficiency is unknown. Likely reasons are the matching of the beam deceleration with the magnetic field, so that the motion of the ions will be locked to the magnetic field lines [see Chapter (2.2.1)] and the focusing properties of the deceleration tube.

5.3.2 Cyclotron Excitation

The tuned circuit offers an excellent method to probe the trap content nondestructively. This method becomes more difficult as the energy and therefore, the temperature of the ions decreases and as there are less ions trapped. Since, in the described experiments, HCIs are cooled to temperatures of about 1 K a different detection scheme is needed. A scheme exciting the modified cyclotron motion of different ion species in conjunction with LIF detection is well suited for such temperatures.

In this scheme the cyclotron motion of a specific ion species is resonantly excited while Be^+ ions are continuously cooled by a laser. By resonantly heating a specific ion with the corresponding cyclotron frequency Be^+ is heated sympathetically. This causes the fluorescence signal of the Be^+ ions to change. By monitoring the LIF while scanning the excitation frequency on the ring electrode resonances are observed. The LIF detection of this heating process can work in two ways.

One possibility (laser-cooled fluorescence mass spectroscopy [67]) is to laser cool Be^+ ions to the cooling limit thereby keeping a maximum but constant scatter rate on the PMT by maintaining a small detuning Δ of the cooling laser. If the Be^+ ions are heated, fewer ions will be on resonance with the laser (σ_s in Equation (4.19) drops for that Δ) and the detected scatter rate will drop. As soon as the excitation is

removed, the Be^+ ions are cooled by the laser to the same temperature as before and the scatter rate rises back to normal. This scheme requires a very steady laser beam in frequency and position to achieve a steady PMT signal at the maximum scatter rate.

A different possibility with less restrictive requirements for the laser stability is to increase the cooling laser detuning ($\Delta \approx 0.8$–1 GHz). At this detuning it cools the ions for a while, but then the cooling power drops since all the ions are much colder and their velocities will rarely have the right component to the laser in order to scatter its photons [$\nu_D \ll \Delta$ in Equation (4.19)]. This also means that the heating sources are not strong enough to heat the ions to where they could be kept at velocities high enough to be on resonance with such a far detuned laser. This results in a rather steady signal close to background. If an ion species is now heated, it will heat the laser cooled ions by collisions and the scatter rate will increase. For this method the stability of the laser position and frequency is not as crucial as for the first method, however, the energy input to heat the ions has to be higher in order to be able to detect a signal.

In Figure (5.17) two series of measurements are shown for the same setup. To see the Be^+ resonance the excitation frequency is swept from 6 to 7 MHz and an additional resonance was seen by sweeping the frequency from 14 to 18 MHz. The two frequencies are $\nu_1 = 6.422(2)$ MHz and $\nu_2 = 15.113(4)$ MHz. It is safe to assume that the resonance at ν_1 is caused by Be^+, but the resonance at ν_2 seems to be too far off to be Be^{2+}. If a value of $B = 4$ T for the magnetic field is assumed (it is set to be approximately 4 T), then an estimate of the mass to charge ratio of 4.04 can be given for ν_2 using Equation (2.27). This suggests, that He^+ is the ion excited at ν_2. The plasma at this point is in equilibrium and, since there is no detectable signal on the tuned circuit, at a temperature around 10 K. It is therefore a good assumption that the whole mixture (i.e. both species) rotates with a constant angular velocity ω. From Equation (2.29) it follows (ω_- is substituted with ω since there is more than

one particle in the trap and the space charge produced by the ion cloud adds to the electric field produced by the electrode potentials) that

$$\omega_+ + \omega = \omega_C \,. \tag{5.2}$$

With Equation (5.2) and Equation (2.27) the relation between magnetic field and the difference of the measured frequencies $\Delta\nu_+$ can be given:

$$\Delta\nu_+ = \frac{1}{2\pi}\left(\frac{q_1}{m_1} - \frac{q_2}{m_2}\right) B \,. \tag{5.3}$$

This allows one to calculate the magnetic field B and therefore, the cyclotron frequency ν_C of each species ($\nu_{C,\mathrm{Be}^+} = 6.941(6)$ MHz and $\nu_{C,\mathrm{He}^+} = 15.630(6)$ MHz) and the rotation frequency of the cloud $\nu = 522(10)$ kHz.

In a second experiment the cyclotron resonance frequency for Be^+ and Be^{2+} was measured in a different way: This time the RF-voltage was pulsed on for a short time τ_E and then the system was given a time τ_R to relax and cool. The timing of the cycle is described in Figure (5.18). The following parameters were used: $\tau_E =$ 50 ms and $\tau_R = 500$ ms. The average turn-on time of the excitation signal was determined to be <10 μs. A typical detected signal on the multi channel scaler is shown in Figure (5.19). Then the excitation frequency ν_E was varied and the maximum amplitude A_{max} was measured and is displayed as a function of ν_E in Figure (5.20). A Gaussian peak function was used to fit the data and the result for the centroids is: $\nu_{+,\mathrm{Be}^+} = 6.92049(9)$ MHz and $\nu_{+,\mathrm{Be}^{2+}} = 13.84377(12)$ MHz. With these values the magnetic field can again be calculated with Equation (5.3): $B = 4.06315(1)$ T. In this experiment Be^{2+} was injected and therefore, its presence was known.

Additional information from this data can be extracted as well. It is not clear how quickly the excitation of the Be^{2+} leads to an increase in the scattered photon signal compared to the excitation of the Be^+ directly. In other words: How different is the coupling between the radial motion of the Be^{2+} to the radial motion of the Be^+ from the coupling of the radial motion of the Be^+ to itself? The data taken in

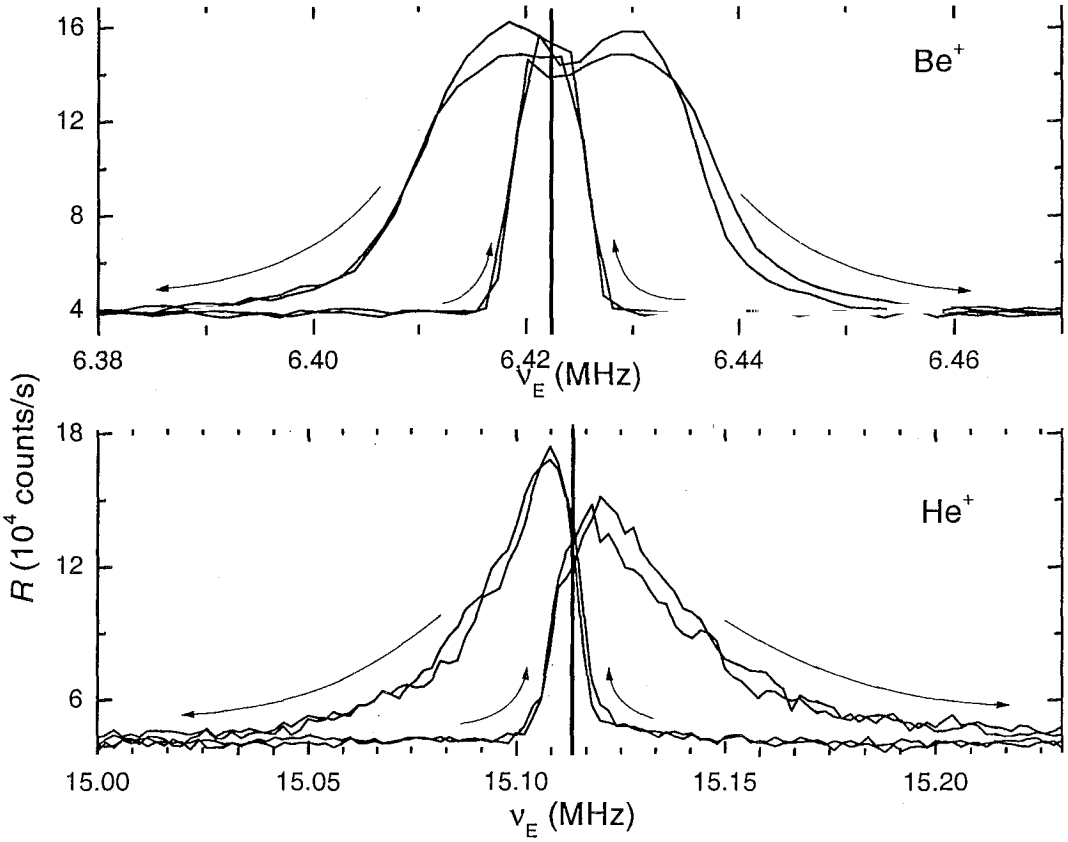

Figure 5.17: Cyclotron excitation of Be^+ and He^+. If the excitation frequency ν_E is swept over a resonance of any ion species trapped together with Be^+, then an increased scatter rate R from the Be^+ ions can be detected due to the heating of the resonant ion species. The arrows indicate the direction of the frequency sweep.

the described way might answer this question. The rise time of the signal in both cases, the Be^+-excitation and the Be^{2+}-excitation, can be fit with $A_{\max}(1 - e^{-\frac{t-t_0}{\tau_H}})$. The time constants τ_H for the fits are: $\tau_{H,Be^+} = 3.53(3)$ ms and $\tau_{H,Be^{2+}} = 3.72(8)$ ms. This suggests, that the differences in collision times between the two species at these temperatures and densities are in the order of 190(110) μs. This result guarantees that the excitation of different ion species than Be^+ heats Be^+ on a timescale of ms as quickly as if Be^+ were directly excited.

The same procedure of exciting and detecting the ion cyclotron motion can be applied to any ion species, as long as Be^+ is trapped with it as well. The result is shown

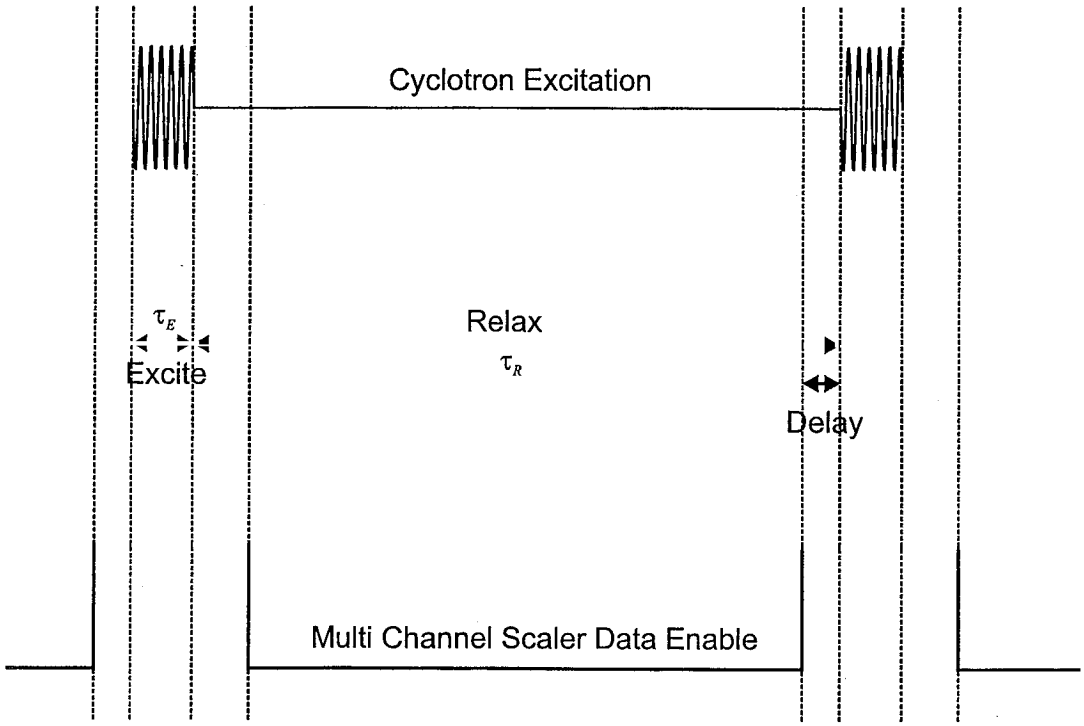

Figure 5.18: Pulsed cyclotron excitation scheme. The ion plasma is given a certain time to be cooled after the heating due to the excitation and come to equilibrium.

in Figure (5.21): Xe^{44+} was injected into Be^{+} and this mixture was continuously probed for approximately 2700 s. The first probing cycles are overlayed in part (a) of the figure and the later ones in part (b). (Notice that are many charge states present in the system). Xe^{44+} ions captured electrons and ions ranging from Xe^{31+}–Xe^{43+} were created: the longer the confinement time, the lower the charge state. Besides the Xe charge states, Be^{2+} and He^{+} can be seen. He^{+} can be created by charge exchange between the HCI and He gas, however, the creation of Be^{2+} is not clear, since the kinetic energies of the HCIs are not sufficient to come close enough for an electron to be transferred from one ion to the other [68]. With the use of Equation (5.2) and Equation (2.27) the following linear relation between the measured resonance frequency ν_+ and the charge to mass ratio can be obtained:

$$\nu_+ = \frac{B}{2\pi} \cdot \frac{q}{m} - \frac{\omega}{2\pi} \,. \tag{5.4}$$

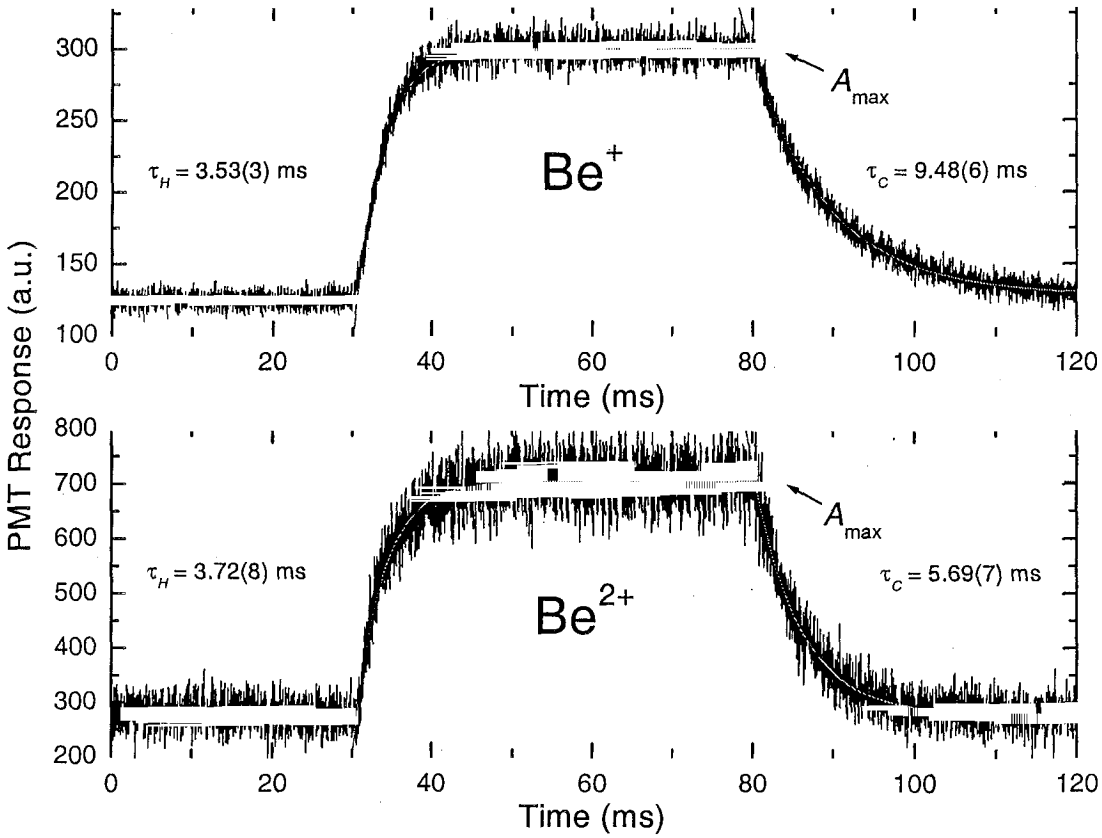

Figure 5.19: Pulsed excitation of Be^+ and Be^{2+}. The time constants for cooling and heating the plasma in each case are comparable. The times and the amplitude were obtained by fitting the functions $A_{\max}(1-e^{-\frac{t-t_0}{\tau_H}})$ and $A_{\max}e^{-\frac{t-t_1}{\tau_C}}$ to the data.

The data extracted from Figure (5.21) and a linear fit to it is shown in Figure (5.22). All the frequencies of the different Xe charge states lie, within their error bars, on a straight line. Only one peak, attributed to the He^+, deviates significantly from this line. The reason for this is unknown. The possibility that the peak was assigned to the wrong ion is unlikely, since the deviation from the line is much less than if a low charge state ion of any different species (including potential molecules) is assigned (higher charge states are excluded since there is not enough energy in the system to create such ions).

The magnetic field determined by the slope of the line is $B = 4.13(1)$ T and the rotation frequency of the cloud is $\nu = 590(40)$ kHz.

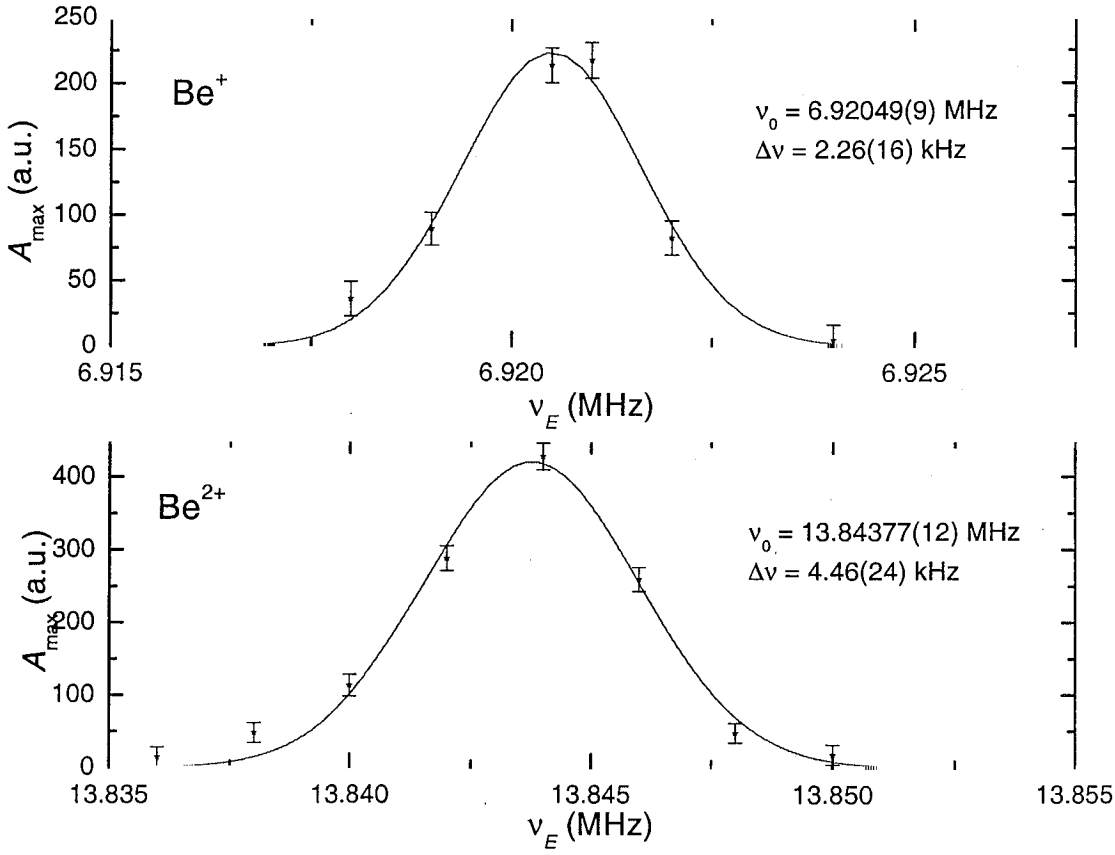

Figure 5.20: Maximum scatter rate $A_{\max}$ in the pulsed cyclotron excitation mode as a function of excitation frequency ν_E. Gaussian line profiles were fit to the data.

Such measurements were repeated for multiple clouds with different constituents and at slightly different magnetic fields. The results are listed in Table (5.1). For systems with only two ion species there is no possibility to do a linear regression since the problem is exactly solvable. The obtained values might have bigger errors than the given errors. But in the case of many ion species a linear regression can be calculated and the errors on the results are more accurate.

The density for each ion species is different, but for $\omega \ll \omega_C$ Equation (3.16) becomes

$$n_0 \approx \frac{2\,\epsilon_0\, m\,\omega\,\omega_C}{q^2} = \frac{2\,\epsilon_0\,\omega\,B}{q}\,, \tag{5.5}$$

and therefore, the use of the product of charge state q and Be^+ density n_{Be^+} in

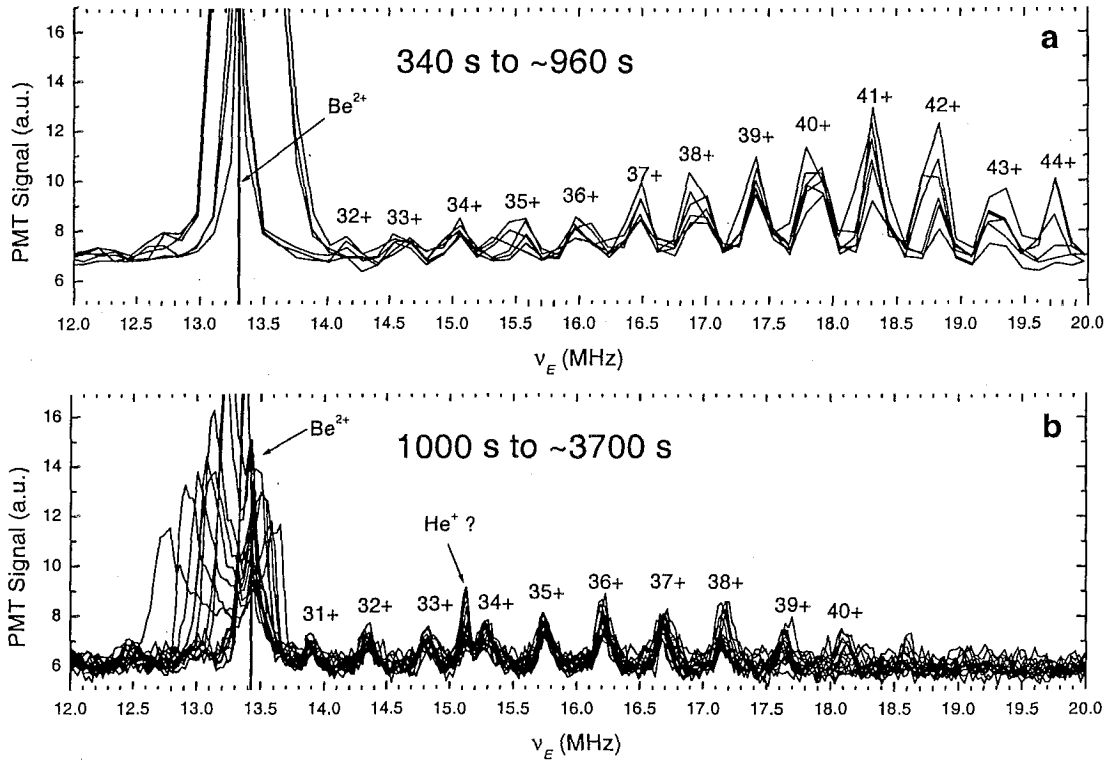

Figure 5.21: A RF voltage with frequency ν_E was applied to two opposing ring sectors of the trap to excite the modified cyclotron motion of the confined ions. When the frequency is on resonance with an ion species the ions are heated and they heat the Be^+. This causes the cloud to scatter more photons. a: The first probing cycles are overlapped with a rather poor resolution of 130 kHz. b: The last probing cycles with a 5 times better resolution of 26 kHz show more detail. The cut off peak in both graphs is caused by Be^{2+}, which has been created due to the injection of the HCIs. Since there is more Be^{2+} than Xe^{q+}, Be^+ is heated more efficiently by Be^{2+} than by the few HCIs.

Table (5.1) is justified. To obtain the density for each ion species with charge state q in that particular mixture the given value in column '$n_{Be^+} \cdot q$' has to be divided by q.

In each set of measurements with HCIs the measured resonance frequency of the singly charged ions always lie below the line obtained by fitting the HCI data. The reason for this is unknown.

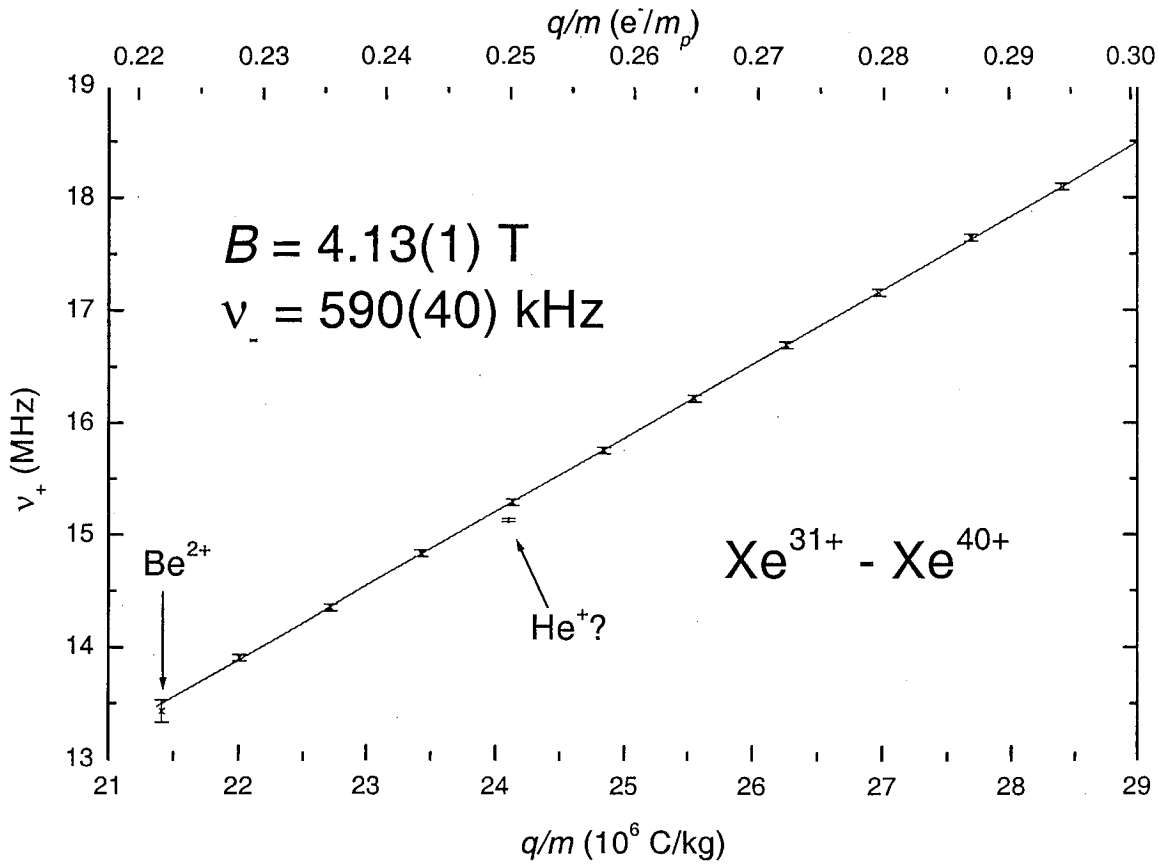

Figure 5.22: Measured modified cyclotron resonance frequencies ν_+ versus the charge to mass ratio q/m of the excited ion species from the data of Fig. (5.21)b. The measured data points from the HCIs and Be^{2+} fit well to a straight line. The value for He^+ lies slightly below the line, indicating a different rotation frequency ν for these ions.

5.3.3 Cloud Imaging and Particle Density

A different way of measuring the density of a trapped ion cloud can be attempted by measuring the aspect ratio of the spheroidal ion cloud. As discussed in chapter (3.3) the cloud shape can be related to the rotation frequency if the Debye length is much smaller than the plasma dimensions. This is easily achieved in our experiments. In this regime a one component plasma forms a spheroidal cloud, which rotates with a constant rotation frequency ν. The density of the cloud can be calculated from the

Table 5.1: Summary of the LIF cyclotron measurements on different ion clouds. The magnetic field B and the rotation frequency ν was obtained by fitting a straight line to the cyclotron resonance data. The density n_{Be^+} can be obtained from the cloud rotation frequency. It is given in units of particle density times charge state. To obtain the real particle density for a species, this value has to be divided by the charge state of that species.

Nr.	Ions	B	ν	$n_{\mathrm{Be}^+} \cdot q$	Note
		T	kHz	$\frac{1}{\mathrm{m}^3}$	
1	Be^+, Be^{2+}	4.06315(1)	2.8(3)	$8(1) \cdot 10^{12}$	pulsed excitation
2	Be^+, He^+	4.075(5)	522(10)	$1.33(7) \cdot 10^{15}$	
3	Xe^{13+}–Xe^{17+}, Be^{2+}	4.452(2)	1122(3)	$2.604(7) \cdot 10^{15}$	
4	Xe^{31+}–Xe^{40+}	4.13(1)	590(40)	$1.5(1) \cdot 10^{15}$	Figure (5.22)
5	Xe^{32+}–Xe^{44+}	4.13(1)	796(40)	$2.0(1) \cdot 10^{15}$	
6	Xe^{32+}–Xe^{39+}	4.142(13)	704(52)	$1.75(13) \cdot 10^{15}$	
7	Xe^{32+}–Xe^{40+}	4.095(15)	477(60)	$1.23(16) \cdot 10^{15}$	
8	Be^{2+}, He^+	4.057(38)	84(130)	$2.3(36) \cdot 10^{15}$	

ratio of the spheroid height $2\,z_{\mathrm{cl}}$ to the width $2\,r_{\mathrm{cl}}$ [see Equations (3.17) and (3.18)], using Equations (3.16) and (3.19). The dimensions of the spheroid can be measured from a side view image.

Two different optical setups to image the cloud were used. The first setup was realized with a cryogenic CCD camera and a directly attached commercial objective lens for UV light. The lens was a Nikon *105mm f/4.5 UV Nikkor AIS* objective lens. The advantages of this setup are the easy alignment, the flat field which is obtained by such a lens corrected for imaging errors, and the high intensity per pixel, making short exposure times possible. The disadvantage is that the actual image of the cloud does not fill the CCD chip and therefore, the resolution is limited to about 100 μm.

In a second setup, the commercial objective lens was replaced by a single biconvex UV lens which was placed in front of the vacuum viewport. The CCD camera was moved away from the lens, achieving a magnification of this optical system of $M = 4$. With this system the image of the ion cloud filled the CCD chip almost completely. Since the photon flux is still the same longer exposure times were necessary to obtain such high resolution images but the resolution is as good as 10 μm. The disadvantage of the long exposure times can be avoided by binning the CCD camera, therefore, decreasing the resolution but increasing the counts per pixel. Stability concerns due to the big distance of the CCD camera from the lens turned out to be unnecessary: once aligned, the images of the cloud did not shift over the CCD chip over a time period of weeks and a realignment was not necessary. Since the cooling laser beam diameter was smaller than the axial cloud extent the shape of the cloud could only be imaged by sweeping the vertical laser beam position over the whole cloud during an exposure.

With the low resolution setup, a series of measurements was done where Be^{+} ions were laser cooled to $\approx$ 10 K and then Xe^{44+} ions were captured into the cold Be. This caused the Be ions to heat up but the laser recools them again [cf. Figure (4.6)]. After the mixture equilibrated the temperature of the Be was dropped by decreasing the detuning Δ of the cooling laser, forcing the mixture to centrifugally separate. This exact same sequence was repeated with a gate valve in the EBIT beamline closed, inhibiting any HCIs to be trapped. In this case a heating of the Be was observed as well, when the pulsing sequence took place, but it was not as strong and therefore, it equilibrated sooner. The most apparent difference to the case with HCIs was that there was no observable separation, when the temperature of the Be was dropped. This experiment was repeated several times and the same observations were made.

The sequence is illustrated in Figure (5.23), where the PMT signal is shown on top and in the bottom part several side view images of the cloud at different times are shown. The point in time when the images were taken is indicated with a Greek

letter. At $t = 5$ s the trap is loaded with Be^+ ions, which are cooled (α) within about 30 s. At $t \approx 38$ s (β) Xe^{44+} ions are injected into the trap, causing the Be^+ to heat up, but within 5–6 s the mixture equilibrates and the PMT signal drops to almost background (γ). The cooling laser detuning was at about 10 GHz and was decreased at this time to 6.5 GHz (δ), reducing the Be^+ temperature further and a clear centrifugal separation can be observed in the side view. The PMT signal at this point is very noisy which is likely to be caused by the positional instability of the laser, which translates, due to the different Doppler shifts of the ions at different radii, into a frequency instability. The general trend is decreasing and the PMT signal comes again close to background (ϵ). At about 100 s the trap is emptied and shortly thereafter reloaded. Before the reloading process a gate valve in the EBIT beamline is closed to inhibit Xe^{44+} ions getting to Retrap. The whole sequence is repeated and images are taken at corresponding times compared to the previous sequence. Note that the initial cool-down peak (ζ) is about twice as high as the previous one. This indicates, that more Be^+ ions were caught in this load. The heating peak (η) due to the pulsing of the voltages for the Xe capture is only half as tall as the cool-down peak, whereas in the previous sequence the heating peak was twice as high as the initial peak. Also in the case with no HCIs, the equilibrium after the HCI-catch pulsing sequence happens within about 2–3 s. At point (ι) where the laser frequency is moved closer to the resonance, the cloud lights up but no separation is observed. The unequal intensity in the images δ and ι is due to a slight misalignment of the laser beam in the horizontal plane. Note also that the visible radial extent of the cloud in the images ϵ and κ is given by the apertures in the ring electrode and not by the cloud size and the axial size of the cloud image is given by the laser beam diameter and not by the cloud size either.

Since in the just described sequence of images the optical resolution was rather low (100 μm) no cloud shape measurements were feasible. After improving the resolution to 10 μm by implementing the above discussed high resolution optical setup, cloud

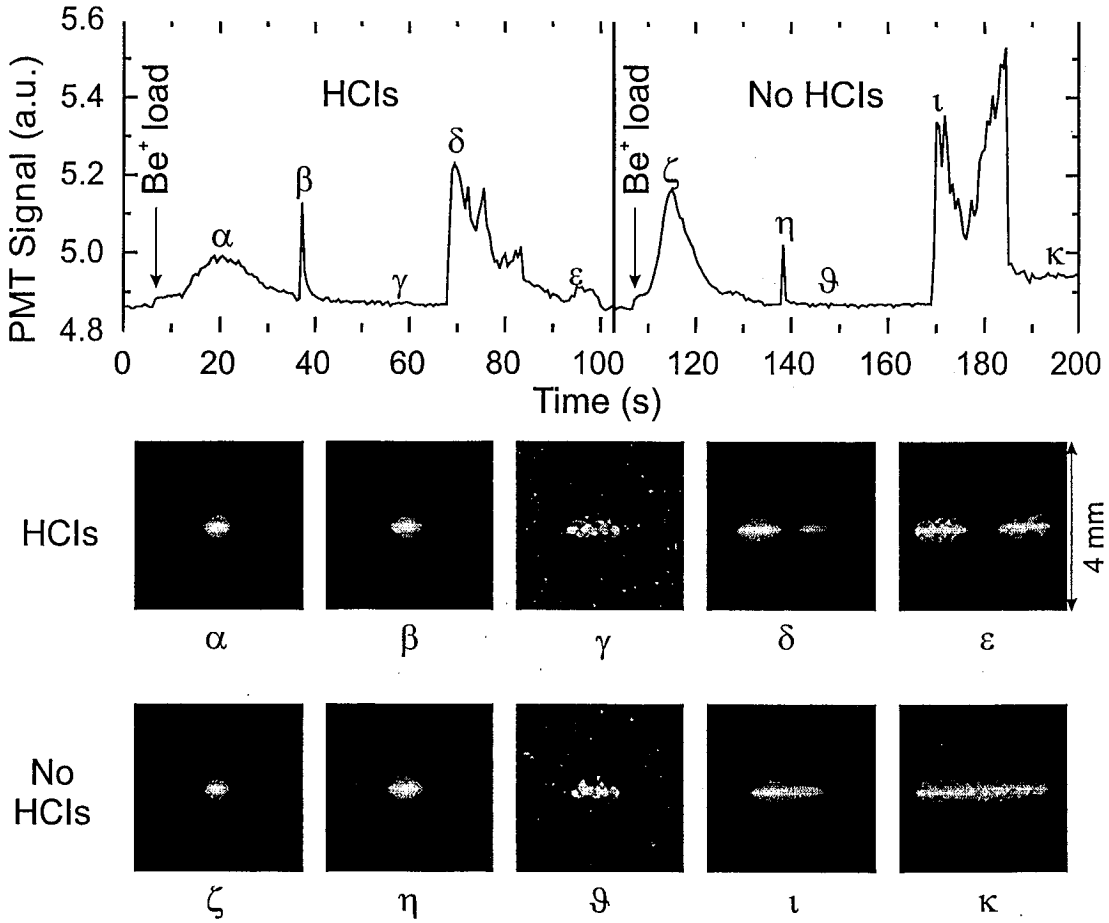

Figure 5.23: Top: PMT signal for two sequences of ion trapping and merging. In the first part Be^{+} was loaded into the trap and Xe^{44+} was added at β and in the second part the same sequence was repeated with a gate valve to EBIT closed, so that no Xe^{44+} could get to Retrap. Bottom: Side view CCD images looking at the cloud while these sequences were performed. The Greek letters indicate at what point the image was taken.

shape measurements were possible. In order to image the whole cloud the cooling laser beam needed to be moved vertically over the cloud. This was accomplished by sweeping the focusing lens manually up and down several times during long exposures. An image obtained in such a way is shown in Figure (5.24): The trap is loaded with only Be^{+}. Since the exposure time was 15 min, the CCD chip was hit by many cosmic rays, which appear as very bright pixels or clusters of pixels (a). The image

was corrected for cosmic rays by replacing the high counts in such pixels by the average of the neighboring 8 pixels (b). The result of an exposure of the CCD chip by uniform light (c) shows that the sensitivity of the pixels over the whole chip is different. This sensitivity also affects real images. To compensate for the different pixel sensitivity a series of such uniform light exposures with different exposure times t_i was made. If the intensity in the j^{th} pixel in the k^{th} row of an exposure of $N \times N$ pixels is $I_{j,k}$ then the average intensity for a given exposure time t_i is:

$$\overline{I(t_i)} = \frac{\sum_{j=1}^{N} \sum_{k=1}^{N} I_{j,k}(t_i)}{N^2} . \tag{5.6}$$

If the sensitivity of each pixel was exactly the same and the exposure was uniform over the whole chip, then $\overline{I(t_i)}$ would be equal to $I_{j,k}(t_i)$. If the pixel intensity is then plotted over the average intensity for different exposure times one would get a perfect line with slope 1 and the intersection 0. Since the sensitivity changes over the CCD chip, such a plot was made for each pixel and therefore, a slope $s_{j,k}$ and a intersection $I_{R,j,k}$ for each pixel can be calculated with a linear regression. With these values any image can be corrected pixel by pixel for the different sensitivity with the following relation:

$$I_{j,k,\text{corr}} = \frac{I_{j,k} - I_{R,j,k}}{s_{j,k}} , \tag{5.7}$$

where $I_{j,k,\text{corr}}$ is the corrected intensity. Practically this did not yield the expected result of eliminating the streaks common to the images in Figure (5.24) a, b and c. It was found empirically that the expectations can be satisfied by adjusting the slope and the intersection for each image with the coefficients α and β:

$$I_{j,k,\text{corr}} = \frac{I_{j,k} - \alpha\, I_{R,j,k}}{\beta\, s_{j,k}} . \tag{5.8}$$

The corrected image is shown in Figure (5.24) d). The low resolution images did not have to be corrected, since the interesting image was confined to a small area consisting of few pixels. The sensitivity, therefore, did not change drastically over that area.

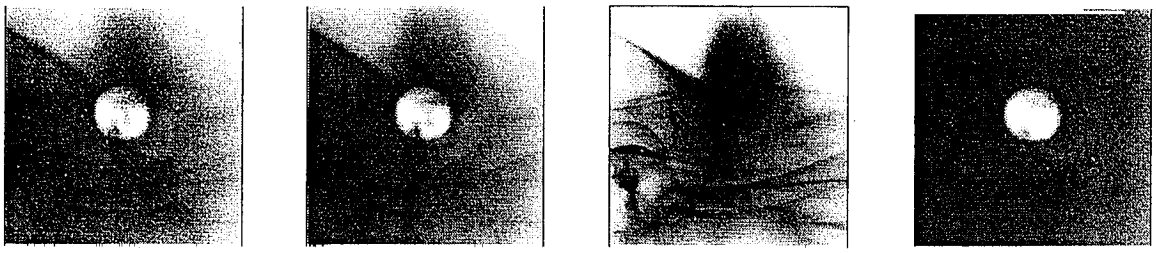

Figure 5.24: Correction sequence for high resolution CCD images. a: original image; b: image corrected for cosmic rays; c: background; d: final corrected image.

All high resolution images had to be corrected. The method using Equation (5.8) gave satisfying results.

To determine the aspect ratio of the observed ellipses in the side view images, the contour of the ellipse was digitized and an ellipse was fit to the data. Both axes of the ellipse are returned as fit parameters. Figure (5.25) contains a series of images with different trap contents: a, b and c show a cloud of only Be^+ ions. In b it is possible to see that there must be some contaminant ions on the outside of the Be^+ since the shape is not a perfect ellipse — the sides of the ellipse are cut off. The rotation frequencies (and therefore the densities) of the first three clouds increase from a to c. The increase of the rotation frequency was established by moving the cooling laser horizontally and therefore, exerting different torques onto the cloud. The measured aspect ratios and calculated densities of these clouds are listed in Table (5.2). Be^{2+} has been added to the clouds in d–g. The centrifugal separation of Be^+ and Be^{2+} is clearly visible: the dark gap in the middle of the cloud are the Be^{2+} ions. However, in image f this separation is not so clear anymore. One possible reason for this is that the plasma might not have been in equilibrium yet. The shape of the cloud in the images d through f has been changed mostly by changing the well depth of the electrostatic potential. In d it is 170 V, in e 90 V and in f 10 V. This does not change the density as drastically as the method of moving the cooling laser. In image g a cloud shape is shown, which was obtained after a cooling laser frequency scan over

the resonance and was stable as long as the laser was not moved. The laser was kept reasonably stable in both dimensions and therefore, the vertical extent of the cloud is most likely determined by the laser beam diameter and not by the cloud size. As soon as the laser was moved, this 'metastable' shape was destroyed and a spheroidal shape was observed.

In another experiment Xe^{34+} was injected into Be^{+}. The obtained images are shown in Figure (5.26) and a clear centrifugal separation is observed. The observed shape of the cloud is still part of an ellipse, just some parts are dark. The HCIs are in these dark parts. However, if a constant cloud rotation of all ion species is assumed, a density for the HCIs can be calculated from the density of the Be^{+} ions [see Chapter (3.3.4)]. The number of HCIs can be obtained by counting the released ions and with the density, the size and shape of the cloud can be calculated. The result of such a calculation is indicated by the gray, cut-off ellipse placed in the dark part of the images in Figure(5.26). The densities calculated from these images are given as well in Table (5.2) for Be^{+} and Xe^{34+}.

From the cyclotron measurements in chapter (5.3.2), the composition of the dark gap is known to be not only the injected Xe^{34+} but also lower charge states of Xe and Be^{2+}. For the density and shape calculation in the figure, 100 Xe^{34+} ions were assumed. The series of images in Figure (5.26) is for the same cloud just after different times. In c it is apparent that some ions with a higher mass to charge ratio have been created. These arrange themselves in a ring around the Be^{+} and cause the ellipse to be clipped on the outside.

5.3.4 Temperature and Cloud Rotation

In the previous sections it was described how the density and the composition of the plasma can be measured with RF-excitation and imaging of the Be^{+} cloud. This section is dedicated to the measurement of the temperature with a LIF technique. The measurement of an ion plasma temperature with LIF is only possible if there is a

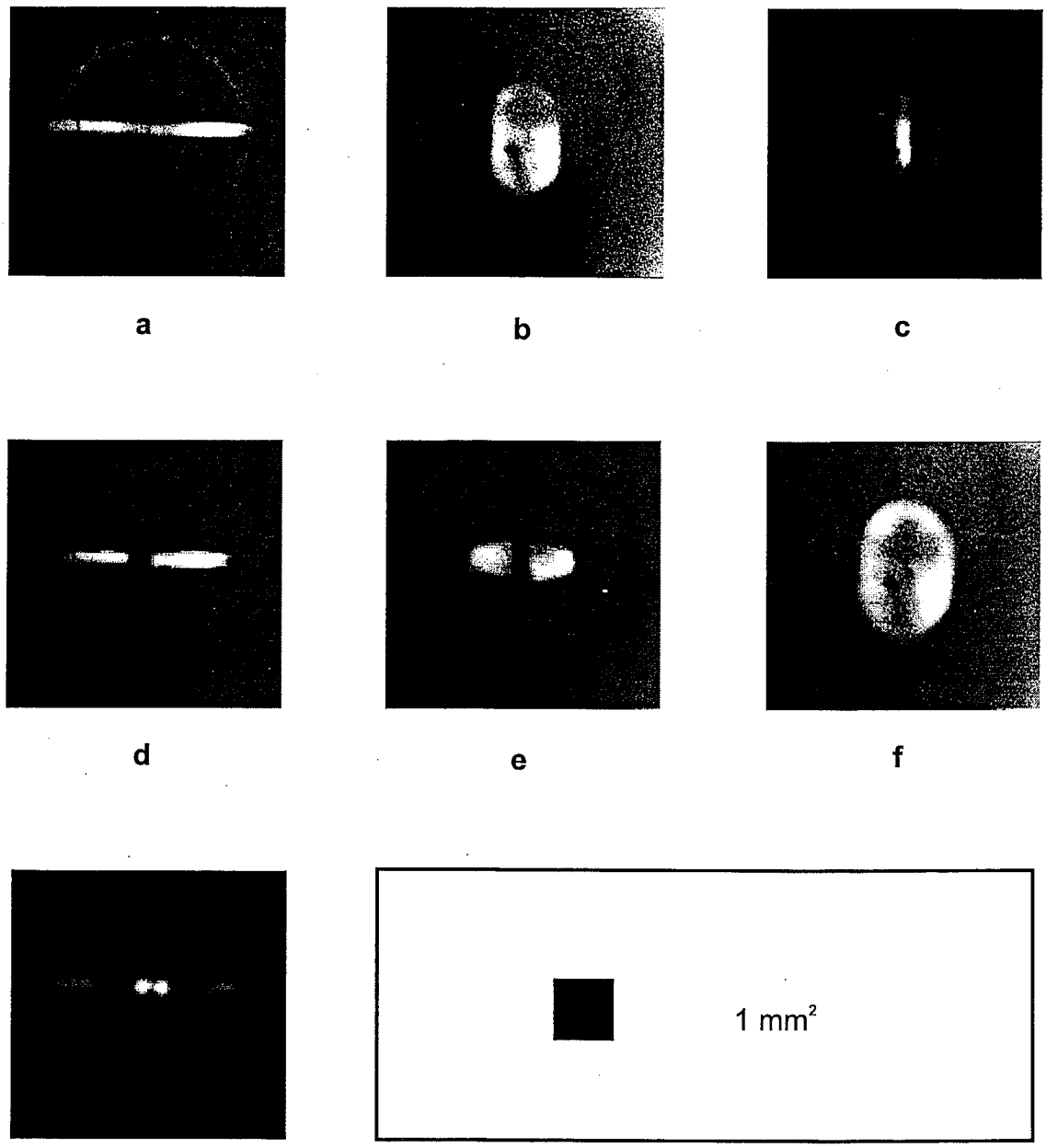

Figure 5.25: High resolution CCD images of Be^+ and Be^{2+} clouds: a–c: only Be^+ at different densities (highest resolution); d–f: Be^+ - Be^{2+} mixture at different densities and g: an unexplained 'metastable' cloud configuration (binned images and therefore, a little lower resolution).

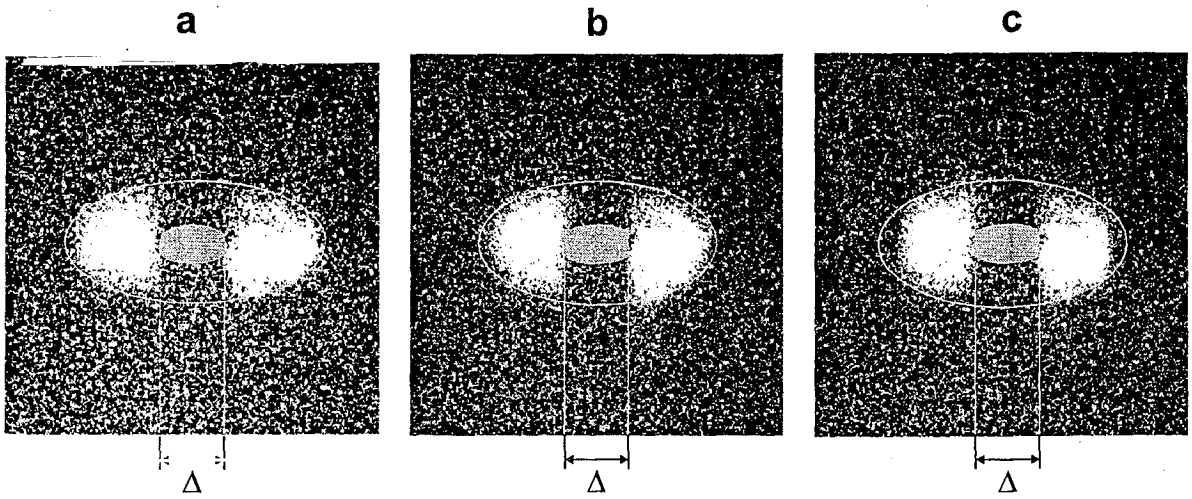

Figure 5.26: High resolution CCD images of Be^+ and Xe^{34+} clouds. The 'invisible' Xe ions are indicated in the image with an ellipse of calculated shape if there were only Xe^{34+} in the center. All the clouds are slightly different due to different trapping times. In c the accumulation of impurity ions on the outside is already rather clear.

laser accessible transition from the ground state available. The HCIs unfortunately do not have strong transitions in the laser accessible regime. However, there are fine- and hyperfine transitions in HCIs, which have a suited wavelength, but these transitions are weak and sophisticated detection schemes have to be applied. The temperature of the HCIs in Retrap will depend on the temperature of the cold Be^+ ions, coupling between the species and external heat sources. These three parameters will determine an equilibrium temperature for any plasma species in the trap. Assuming that the external heat sources are constant for all the ion species, it is possible, by determining the cooling power and the temperature for a pure Be^+ plasma, to calculate the heating power. With molecular dynamics simulations [see Chapter (6)] the strength of the coupling can be determined.

A spectroscopic technique with an additional laser is used to realize the temperature measurement. A scan of the cooling laser over the 2s $^2S_{\frac{1}{2}}(m_j = -\frac{1}{2})$–2p $^2P_{\frac{3}{2}}(m_j = -\frac{3}{2})$ cooling transition can not be used to extract information about the temperature. It fails, because the cooling laser changes the temperature of the

Table 5.2: Summary of the densities n, rotation frequencies ν and numbers of ions N of different clouds in the trap. The measured quantities are the length of the axes of the ellipses a and b and the confinement voltages U. If more than one species is in the trap, the density of the other species can be calculated, by assuming that the rotation frequency is the same for all ions. The image number refers to Figure (5.25) and Figure (5.26).

image	ion	a	b	U	ν	n	N
		mm	mm	V	kHz	$\frac{1}{m^3}$	
Figure (5.25)							
a	Be^+	1.360(40)	0.0125(12)	38(2)	37.7(20)	1.04(5) 10^{14}	1.00(16) 10^5
b	Be^+	0.576(12)	0.829(9)	38(2)	137.5(80)	3.74(20) 10^{14}	4.3(3) 10^5
c	Be^+	0.141(2)	0.483(4)	38(2)	375(20)	9.84(50) 10^{14}	4.0(2) 10^4
d	Be^+	1.301(34)	0.186(7)	170(2)	186(10)	5.0(3) 10^{14}	6.7(7) 10^5
	Be^{2+}					2.5(2) 10^{14}	1 10^5
e	Be^+	0.822(9)	0.367(6)	90(2)	105(4)	2.87(9) 10^{14}	1.46(10) 10^6
	Be^{2+}					1.44(5) 10^{14}	1 10^5
f	Be^+	0.736(9)	1.062(11)	10(2)	36(8)	1.0(2) 10^{14}	2.4(5) 10^5
	Be^{2+}					5.0(1) 10^{15}	1 10^5
Figure (5.26)							
a	Be^+	1.47(1)	0.67(1)	50(2)	79(4)	2.16(9) 10^{14}	1.3(2) 10^6
	Xe^{34+}					6.4(3) 10^{12}	100
b	Be^+	1.38(1)	0.71(1)	50(2)	84(4)	2.3(1) 10^{14}	1.3(2) 10^6
	Xe^{34+}					6.8(3) 10^{12}	100
c	Be^+	1.38(1)	0.71(1)	50(2)	84(4)	2.3(1) 10^{14}	1.3(2) 10^6
	Xe^{34+}					6.8(3) 10^{12}	100

plasma during the scan: on the lower frequency side of the transition the laser cools the ions [cf. Equation (4.14)] and therefore, will steepen the wing of the transition; on the higher frequency side, the laser will heat the ions fast, so that no ions will be on resonance right after the transition, causing the higher frequency wing of the line to disappear. However, the temperature can be measured using a second laser tuned to the 2s $^2S_{\frac{1}{2}}(m_j = -\frac{1}{2})$ - 2p $^2P_{\frac{3}{2}}(m_j = +\frac{1}{2})$ transition (probing transition), which depopulates the ground state 2s $^2S_{\frac{1}{2}}(m_j = -\frac{1}{2})$ and pumps the ions into the 2s $^2S_{\frac{1}{2}}(m_j = +\frac{1}{2})$ state which is not on resonance with the cooling laser. If the second (probe) laser is scanned over the probing transition, while the cooling laser is kept at a fixed frequency detuning close to the cooling resonance to maintain a high scatter rate, the scatter rate will drop due to the depopulation of the ground state. This dip in the fluorescence signal can be fit to a Voigt line profile and the temperature is obtained as a fit parameter.

A series of such temperature measurements was done on a single Be^+ cloud in order to determine the relation between cooling laser detuning and achievable temperature: For a given radial position R_i of the probe laser with respect to the cloud center, the frequency ν_T is scanned over the resonance of the probing transition (Figure (5.28) single probe scan). From such a scan the centroid $\nu_C(R_i)$ and the width $\Delta\nu_{G,R_i}$ of the line can be extracted. The Lorentz width is assumed to be 19.4 MHz [69] and was entered as a fixed parameter. Since all the particles in the cloud rotate with a constant angular frequency ω, the centroid of the line will shift with the radial position of the probe laser. A simple geometrical consideration [see Figure (5.27)] reveals that all particles on a straight line G through a cloud, which rotates with a constant angular rotation frequency ω, perpendicular to the magnetic field, have the same velocity component $\vec{v}_{L,i}$ in direction of the line. Therefore, the Doppler shifted, probe resonance frequency is the same for all particles on that line as well. The frequency difference $\Delta\nu_C$ of two probe transitions at different probe laser positions

due to the Doppler shift is:

$$\Delta\nu_C = \nu_C(R_k) - \nu_C(R_i) = \frac{\omega}{\lambda} \cdot (R_k - R_i) = \frac{\omega}{\lambda} \cdot \Delta R \,. \tag{5.9}$$

If the measured centroids are plotted as a function of the radial positions of the probe laser, a linear regression yields the slope k_j of this line. This slope can be used to calculate the rotation frequency $\nu = \frac{\omega}{2\pi}$ of the cloud:

$$\nu = \frac{1}{2\pi} k_j \lambda \tag{5.10}$$

Since the laser beam is not an ideal line but rather a beam with a Gaussian intensity distribution, a convolution of the beam profile with the absorption peak of an ideal infinitely narrow laser beam is measured. This broadens the measured line width to $\Delta\nu_{G,R_i}$. To calculate the real Doppler line width $\Delta\nu_T$ caused by the finite temperature of the ions the Gaussian part from the beam profile $\Delta\nu_{\text{beam}}$ has to be deconvolved. If the beam diameter is known [see Section (5.3.4.1)], it can be transformed into frequency units by multiplying it with the slope of Equation (5.10). Since both the line shapes are Gaussian, $\Delta\nu_T$ can be calculated in the following way:

$$\Delta\nu_T = \sqrt{\Delta\nu_{G,R_i}^2 - \Delta\nu_{\text{beam}}^2} \,. \tag{5.11}$$

From this width the temperature of the cloud can be calculated with the relation

$$T = \frac{\Delta\nu_T^2 \, m \, \lambda^2}{8 \, k_B \ln 2} \,, \tag{5.12}$$

where m is the mass of the ion species and λ is the wavelength of the probing transition. For the same detuning Δ_j of the cooling laser the same temperature T_j is expected to be measured and an average of all the temperatures $\overline{T_j}$ at Δ_j is calculated. This procedure of measuring the cloud temperature with correction for the finite beam diameter was repeated for several different values of Δ. The result is shown in Figure (5.29), where the average temperature for a certain detuning is plotted as a function of the detuning.

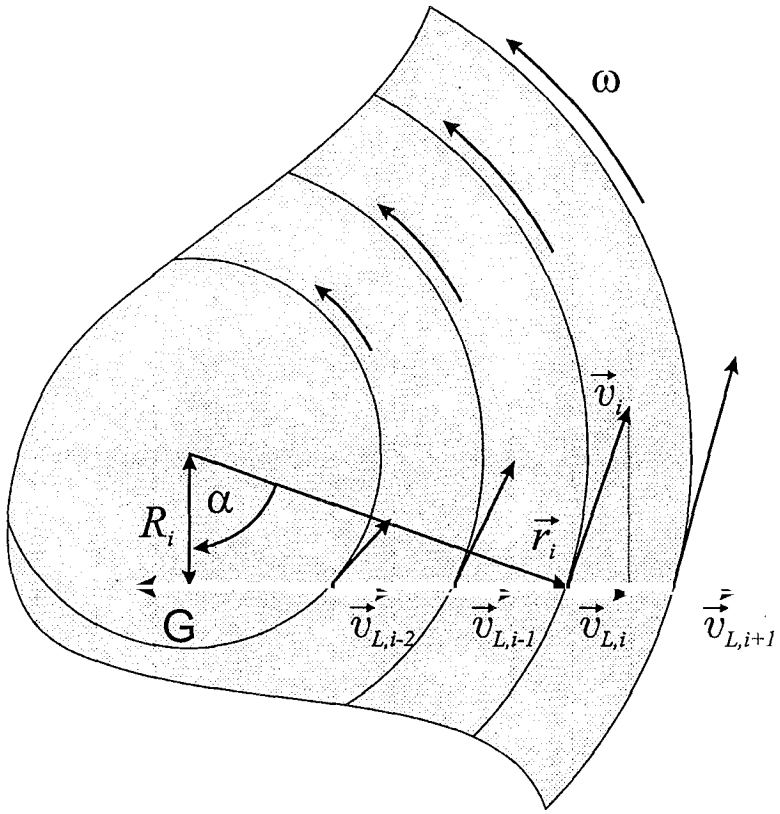

Figure 5.27: If a cloud rotates as a rigid body with the angular frequency ω, then all the velocity components $\vec{v}_{L,i}$ along a straight line through the cloud are the same.

The expected functional relation between these two quantities is a quadratic function. This can be deduced from the expression for the laser cooling power P_C. The rate of energy extraction per ion is given by [cf. Equation (4.17)]

$$P_C = \frac{dQ}{dt} = \epsilon_{LC}\, h\, \Delta\, \sigma_s(\nu_L)\, I_L\, \frac{1}{h\nu_L}\,, \tag{5.13}$$

where I_L is the laser flux in the cloud and ϵ_{LC} is a factor ≤ 1 describing the overlap of the laser beam with the ion cloud. If the natural line width γ is much less than the Doppler width $\Delta\nu_T$, the scattering cross section $\sigma_s(\nu_L)$ can be given by

$$\sigma_s(\nu_L) \approx \sigma_0 \frac{\gamma\sqrt{\pi}}{2\,\Delta\nu_T}\, e^{-\left(\frac{\Delta}{\Delta\nu_T}\right)^2}\,, \tag{5.14}$$

where σ_0 is the resonance scattering cross section (for such transitions $\sigma_0 = \frac{\lambda^2}{2\pi}$) and $\Delta\nu_T$ is given by Equation (5.12). If Equation (5.14) is inserted into Equation (5.13)

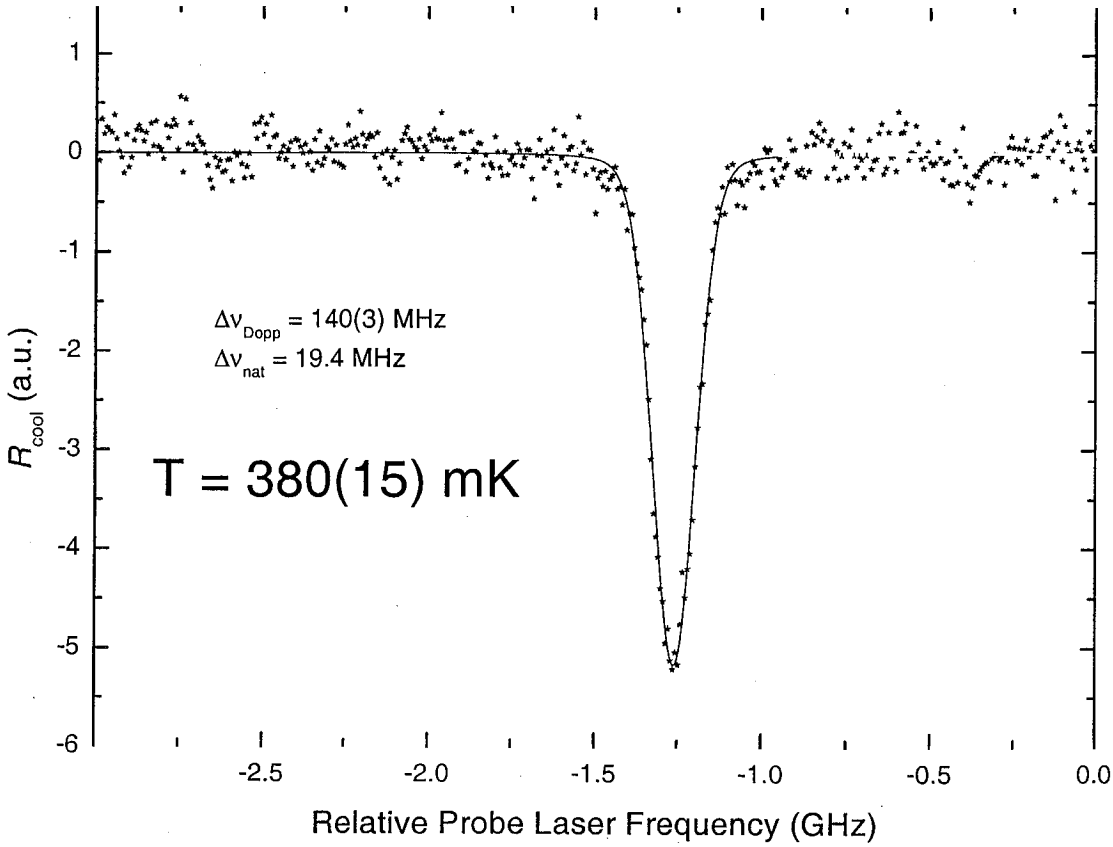

Figure 5.28: Probe laser resonance: If the probe laser is scanned over the depopulation transition, the scatter rate R_{cool} from the cooling laser drops and if the process is performed slow enough, the line shape can be fit to a Voigt profile, which will yield the Doppler width and thereby the temperature of the cloud. The shown measurement is not corrected for the cloud rotation, which would reduce the calculated temperature.

the following expression is obtained:

$$P_C = A \cdot x \cdot e^{-x^2} \tag{5.15}$$

with

$$x = \frac{\Delta}{\Delta\nu_T} \tag{5.16}$$

and

$$A = \frac{\sigma_0 \, I_L \, \gamma \, \sqrt{\pi}}{\nu_L} \, . \tag{5.17}$$

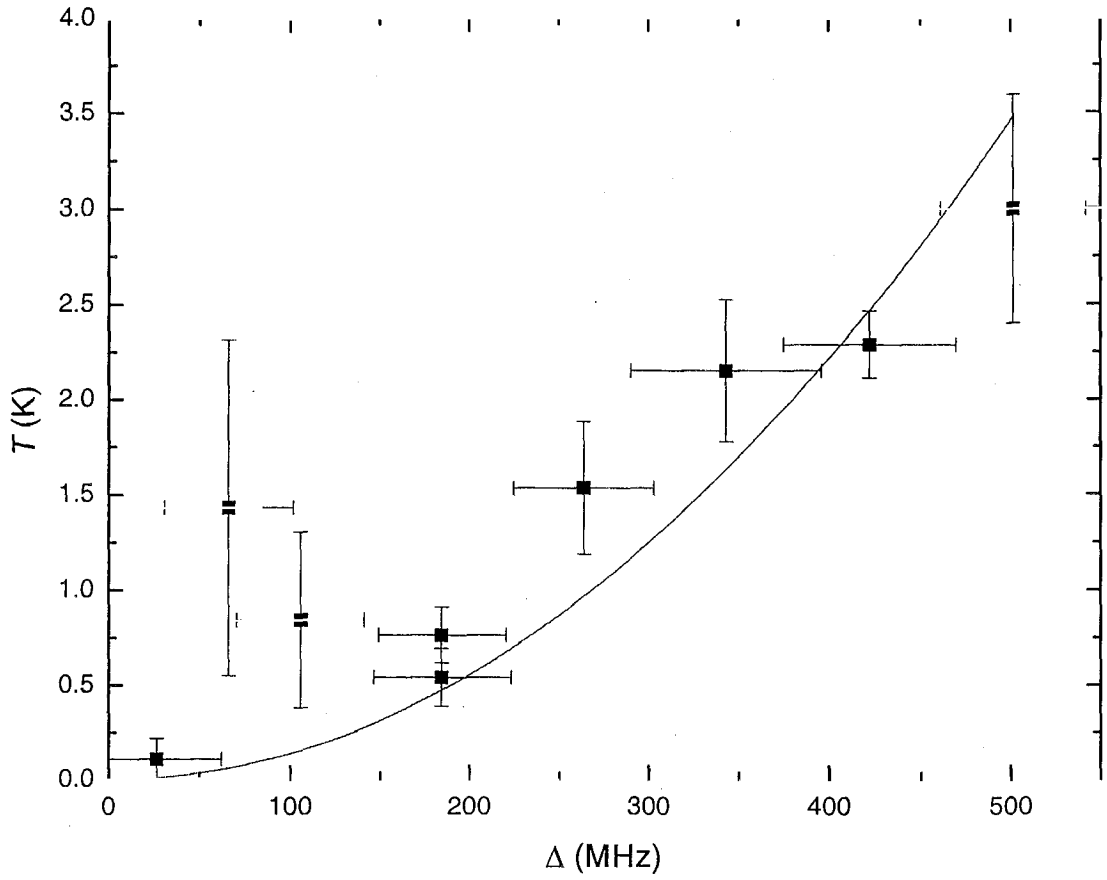

Figure 5.29: Temperature T of a Be^+ plasma versus detuning Δ of the cooling laser. For small detunings the stability of the cooling laser is crucial and was not always achieved. This could explain the large deviations of some data points. The solid line is the result of a fit using the quadratic function in Equation (5.19)

If the plasma in the trap is in thermal equilibrium, the heat extraction P_C has to match the heat input from all heat sources P_H (to name two possible sources: trap imperfections, electro-magnetic radiation noise). If the assumption is made that the external heat sources do not vary in time, both these quantities have to be constant as well:

$$P_C = P_H = \text{const} . \tag{5.18}$$

It is not known what the heat sources in the experiment are, but with Equation (5.18) the total heating power can be calculated if the cooling power is known, when the

cloud is in equilibrium. Equation (5.18) can only be fulfilled if x in Equation (5.16) is a constant. This condition and replacing $\Delta\nu_T$ with the help of Equation (5.12) yields the relation between the cooling laser detuning and the temperature when the cloud is in thermal equilibrium:

$$T = C \cdot \Delta^2 \,, \tag{5.19}$$

where C is a constant which has to be determined from the experiment. In Figure (5.29) a quadratic model function has been fit to the data. The fit yields $C = 1.38(12)10^{-5}\ \frac{\mathrm{K}}{\mathrm{MHz}^2}$ and thus x can be calculated:

$$x = 1.18(5) \,. \tag{5.20}$$

By knowing this constant, all the parameters in Equation (5.15) are known and the cooling power and the heating power can be calculated to $P_C = P_H = 1.1(1) \cdot 10^{-20}\ \frac{\mathrm{W}}{\mathrm{particle}}$ (The intensity of the cooling laser was 1.1 mW in a beam with the diameter of 180 μm and an overlap of $\epsilon_{LC} = 3 \cdot 10^{-3}$ was calculated from the fluorescence). To obtain a different unit, P_H is divided by k_B and the result is: $P_H = 770(80)\ \frac{\mathrm{K}}{\mathrm{particle \cdot s}}$.

It is also possible to calculate the cooling rate by estimating the photon detection efficiencies, calculating the solid angle and estimating the beam cloud overlap. The beam cloud overlap can be estimated by measuring the cloud dimensions on the CCD side view image. With this estimate a heating rate of about 1000 $\frac{\mathrm{K}}{\mathrm{particle \cdot s}}$ is calculated. This is in good agreement with the previously obtained value.

5.3.4.1 Laser Beam Diameter As mentioned before the beam diameter $\Delta\nu_{\mathrm{beam}}$ is an important parameter for correcting the measured width of the Gaussian line profile to obtain the information about the temperature of the ions. The measurement of the laser beam profile was performed in two ways [see Figure (5.30)]. One way is to measure the intensity profile along the z-axis in a side view image of the Be^+ cloud on the CCD chip, when the laser beam is not moved and the cloud is large compared to the beam dimensions [Figure (5.30)a]. In the second method a rotating disc with

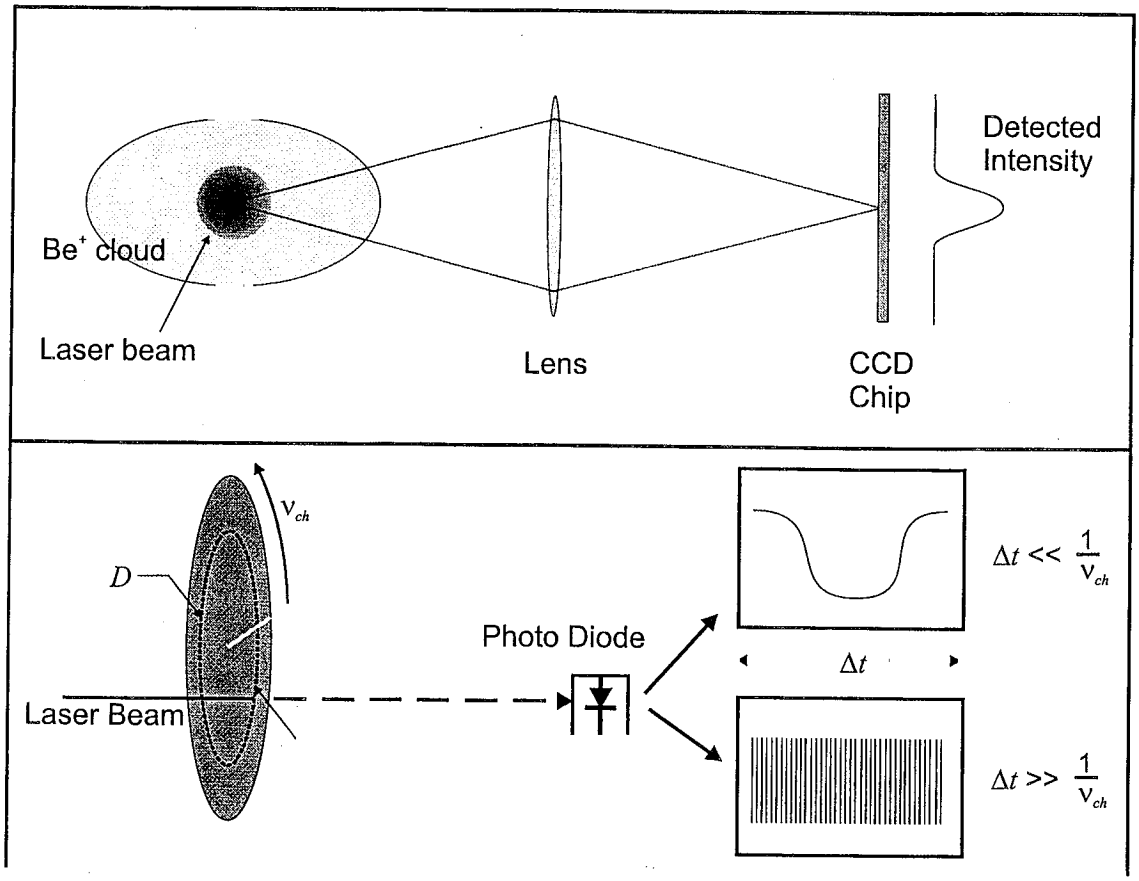

Figure 5.30: Sketch of the two applied schemes to measure the laser beam diameter. a: The Be^+ cloud is bigger than the beam and is assumed to have equal density throughout the cloud. The information is obtained by taking a CCD image and evaluating the detected intensity profile. b: A rotating disc with a slit is placed in the position where the knowledge of the beam diameter is desired. By evaluating the photo diode signal as a function of time for different time intervals Δt and measuring D the beam diameter can be calculated.

a slit is placed where it is desired to know the diameter and the beam intensity is measured with a fast photodiode [Figure (5.30)b].

In the latter case the chopper wheel will progressively uncover the beam (increasing signal on the diode) until the whole beam passes through the slit (signal is a maximum and it is flat) and then the beam will again be covered. The wings of the diode signal versus time $I_D(t)$ contain information about the beam intensity profile $I(t)$ (here

the intensity is a function of time, but it can be converted into a function of length by using the velocity of the slit). Mathematically, a deconvolution of the measured intensity by the transmission of the slit is necessary. Since the slit transmission is a simple mathematical function (rectangular pulse), it is possible to show that the deconvolution is equivalent to a differentiation with respect to time. If the slit is wide compared to the beam diameter, it is possible to look only at one side of the slit and model the transmission $T(t)$ of the slit as a step function:

$$T(t) = \begin{cases} 0 & : \quad t < 0 \\ 1 & : \quad t \geq 0 \end{cases} \tag{5.21}$$

To show the equivalence of the deconvolution with the differentiation we write the definition of the convolution $I(t) \otimes T(t)$ and show that in this case it is equivalent to the integration:

$$\begin{aligned} I_D(t) = I(t) \otimes T(t) &= \int_{t'=-\infty}^{t'=\infty} I(t')\, T(t-t')\, \mathrm{d}t' \\ &= \int_{t'=-\infty}^{t'=t} I(t')\, T(t-t')\, \mathrm{d}t' + \int_{t'=t}^{t'=\infty} I(t')\, T(t-t')\, \mathrm{d}t' \ . \end{aligned} \tag{5.22}$$

If the definition for the step function Equation (5.21) is used Equation (5.22) can be written as:

$$I_D(t) = \int_{t'=-\infty}^{t'=t} I(t') \cdot 0 \quad \mathrm{d}t' + \int_{t'=t}^{t'=\infty} I(t') \cdot 1 \quad \mathrm{d}t' = \int_{t'=t}^{t'=\infty} I(t')\, \mathrm{d}t' \ . \tag{5.23}$$

This shows the equivalence of the convolution with the integration in case one of the two functions is a step function. Since the inverse function of the integration is the differentiation, the differentiation is equivalent to the inverse of the convolution: the deconvolution. The second edge of the slit is just another step function as long as the slit is wide. If the slit becomes narrow, a differentiation does not yield correct results.

In order to convert the beam profile as a function of time to an intensity profile as a function of radius, the velocity of the slit v_S needs to be measured. This is

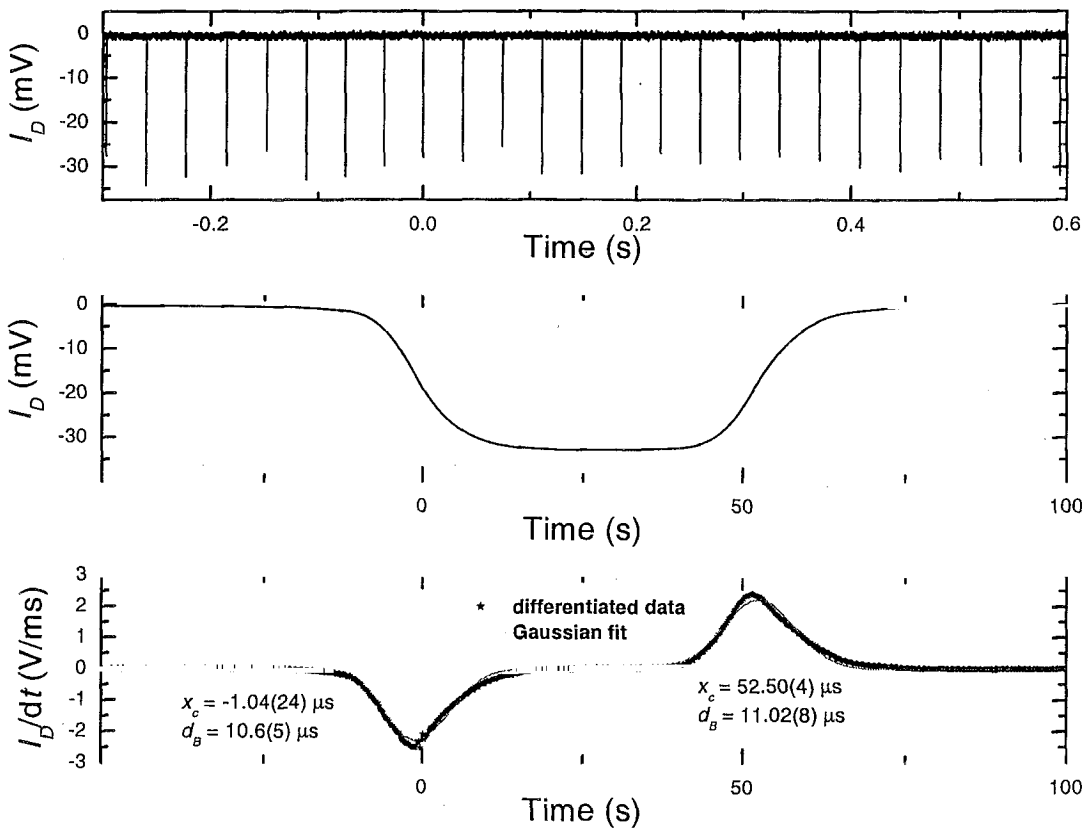

Figure 5.31: Data to measure the laser beam diameter with a chopper wheel. Top: Photo diode signal I_D over a long time Δt to get the chopper frequency ν_W. Middle: Photo diode signal over a short time Δt to get the beam profile information. Bottom: Differentiated photo diode signal over a short time yielding a signal proportional to the beam profile with two Gaussian fits. The resulting fit parameters are noted in the graph.

accomplished by increasing the time interval Δt on the oscilloscope when measuring the diode signal. This signal looks comb-like and by counting the teeth of the comb N_T the frequency ν_W of the wheel can be measured. The radius $\frac{D}{2}$ of where the beam hits the wheel has to be measured as well. In Figure (5.31) such a measurement is shown. The radius was $\frac{D}{2} = 3.34(1)$ cm, the measured frequency was $\nu_W = 26.9567(22)$ Hz and the velocity was calculated to be $v_S = 5.657(17)$ $\frac{\mathrm{m}}{\mathrm{s}}$. From the results of the two fits an weighted average for the beam width $\overline{d_{B,t}}$ can be calculated: $\overline{d_{B,t}} = 10.96(26)$ μs

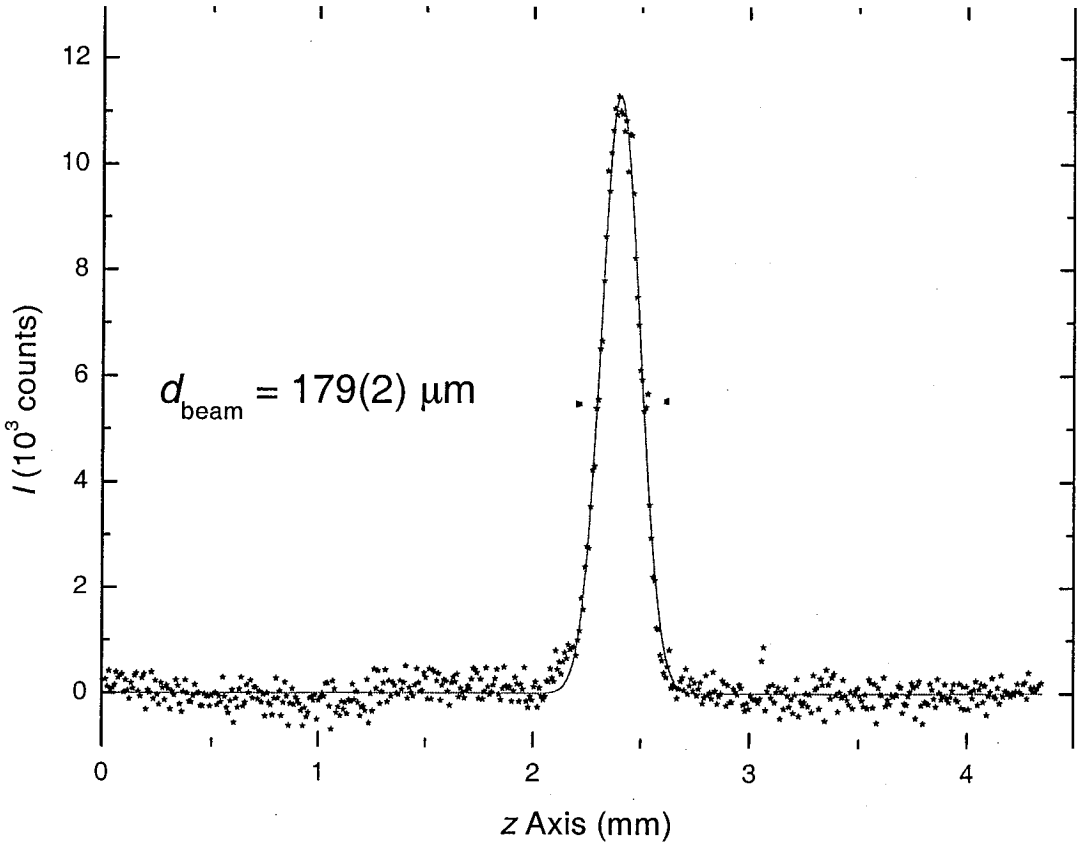

Figure 5.32: Intensity I along a column of a CCD imaging the cooling laser beam intersecting a large Be^+ cloud. It can be assumed that the density of the Be^+ ions is constant over the cross-section of the laser beam. Therefore, this image provides information about the laser beam profile in the z-direction.

which corresponds to $\overline{d_{B,probe}} = 62.0(15)\ \mu$m.

Another possibility of measuring the beam diameter is by imaging the fluorescing cloud. This method was applied to measure the cooling laser diameter. While the cooling laser is cooling the Be^+ cloud and the cloud is guaranteed to be much larger in the z-direction than the laser beam, a CCD image of the cloud is taken. Since the beam is smaller than the cloud and the cloud can be assumed to have a constant density [70] over its volume the CCD detects a projection of the beam profile. Such a measurement has been performed for the cooling laser. The intensity along the z-axis is shown in Figure (5.32). A Gaussian fit seems to be good enough to approximate

this profile. A beam width of $d_{B,\mathrm{cool}} = 179(2)$ μm is calculated as the full width at half maximum.

6 Molecular Dynamics Simulations

In Molecular Dynamics (MD) simulations the equations of motion are evaluated for each of the N particles by (numerical) integration. Therefore, it is possible to get all the system parameters like density, temperature, potential energy, etc. at any given time. Since the force on one particle depends on all the other $N-1$ particles, the solution of such problems will usually be obtained by solving a system of coupled differential equations. The calculation time required is on the order of $\mathcal{O}(N^2)$ and therefore, the problems are often limited to a small number of particles. The forces involved in describing the experimental situation here are limited to the well known Coulomb interaction between the particles and forces on moving charged particles in static electric and magnetic fields.

6.1 Principle

The equations of motion for N particles with the mass m_i and the charge q_i moving in a static electric ($\vec{E}$) and magnetic ($\vec{B}$) field are given by

$$m_i \cdot \ddot{\vec{r}}_i(t) = \vec{F}_i(t) \; ; \; i = 1, .., N \; , \tag{6.1}$$

where the force $\vec{F}_i(t)$ is given by the sum of all forces acting on the particle:

$$\vec{F}_i(t) = \underbrace{\frac{q_i}{4\pi\epsilon_0} \sum_{\substack{j=1 \\ j\neq i}}^{N} \frac{q_j \vec{r}_{ij}}{r_{ij}^3}}_{\text{Coulomb interaction}} + \underbrace{q_i (\dot{\vec{r}}_i \times \vec{B})}_{\text{Lorentz force}} - \underbrace{q_i \vec{\nabla} \Phi_T(\vec{r}_i)}_{\text{quadrupole potential}} \; , \tag{6.2}$$

where Φ_T is the trap potential from Equation (2.19) and the interparticle distance is given by $\vec{r}_{ij} = \vec{r}_i - \vec{r}_j$. The position of the particle $\vec{r}_i(t)$ can be expanded into a Taylor series around t and yields the following approximation for the times $t+\tau$ and $t-\tau$:

$$\vec{r}_i(t+\tau) = \vec{r}_i(t) + \tau \dot{\vec{r}}_i(t) + \frac{\tau^2}{2} \ddot{\vec{r}}_i(t) + \frac{\tau^3}{6} \dddot{\vec{r}}_i(t) + \mathcal{O}(\tau^4) \tag{6.3}$$

and

$$\vec{r}_i(t-\tau) = \vec{r}_i(t) - \tau \dot{\vec{r}}_i(t) + \frac{\tau^2}{2} \ddot{\vec{r}}_i(t) - \frac{\tau^3}{6} \dddot{\vec{r}}_i(t) + \mathcal{O}(\tau^4) \; . \tag{6.4}$$

By adding Equation (6.3) to Equation (6.4) and by subtracting Equation (6.4) from Equation (6.3) expressions for the iteration of the position and the velocity $\vec{v}_i(t) = \dot{\vec{r}}_i(t)$ are obtained:

$$\begin{aligned} \vec{r}_i(t+\tau) &= 2\,\vec{r}_i(t) - \vec{r}_i(t-\tau) + \tau^2\,\ddot{\vec{r}}_i(t) + \mathcal{O}(\tau^4) \\ \vec{v}_i(t) &= \frac{\vec{r}_i(t+\tau) - \vec{r}_i(t-\tau)}{2\,\tau} + \mathcal{O}(\tau^3)\,. \end{aligned} \tag{6.5}$$

The iteration rules in Equation (6.5) constitute the Verlet algorithm. This algorithm was chosen to solve the problem in Equation (6.1) and it needs the position at t and at $t-\tau$. Two positions have to be given to start the problem and the velocity lags behind by τ. If the real expression for the force, Equation (6.2) is inserted into the equations for the iteration Equation (6.5), the Verlet algorithm is turned into a implicit algorithm with respect to the velocity and position. With a magnetic field of $\vec{B} = (0,0,B)$ and the position of one particular particle $\vec{r} = (x,y,z)$ with the velocity $\vec{v} = (v_x, v_y, v_z)$ the iteration instruction becomes

$$\begin{aligned} x(t+\tau) &= 2\,x(t) - x(t-\tau) + \frac{\tau^2}{m}\Big(\underbrace{F_x}_{\text{non-Lorentz}} + q\,B\, \underbrace{v_y}_{\frac{y(t+\tau)-y(t-\tau)}{2\tau}} \Big) \\ y(t+\tau) &= 2\,y(t) - y(t-\tau) + \frac{\tau^2}{m}\Big(\underbrace{F_y}_{\text{non-Lorentz}} - q\,B\, \underbrace{v_x}_{\frac{x(t+\tau)-x(t-\tau)}{2\tau}} \Big) \\ z(t+\tau) &= 2\,z(t) - z(t-\tau) + \frac{\tau^2}{m}\Big(F_z \Big) \end{aligned} \tag{6.6}$$

Equations (6.6) are the relations needed to iterate the positions of each particle if the index i is added to all the equations. For the time step τ a fraction of the inverse

plasma frequency ω_p was chosen:

$$\tau = \beta \frac{1}{\omega_p} = \beta \sqrt{\frac{\epsilon_0 m}{n_0 q^2}} \,. \tag{6.7}$$

Determining β is an empirical process and the right choice will yield a run, where the total energy is conserved to a good approximation. If β is too large, particles have the chance to advance too far and might come very close to each other. This causes, in that next time step, the Coulomb repulsion to be extremely high and the particles will experience a big acceleration, resulting in large velocities. This might increase the total energy of the system. If β is too small, the calculation time will be unnecessarily long and rounding errors are introduced. A typical value for β is 10^{-3}.

At this point it should be mentioned and emphasized that this algorithm works for arbitrary ion species and mixtures thereof. In this work however only mixtures consisting of up to two species have been simulated.

6.2 Initialization, Cooling and Heating

6.2.1 Initialization

A typical start configuration of particles is an ensemble of particles ordered in an arbitrary crystal lattice of an initial density n_I to avoid short distances of particles, which could potentially violate energy conservation. The velocity of each particle is seeded using a Maxwell-Boltzmann distribution. Note that the temperature of this distribution will not be the temperature of the resulting equilibrium configuration, since the initial kinetic energy will not correspond to the final kinetic energy, which results from equilibration processes between potential and kinetic energies.

As input parameter it is possible to give the species of the ions (limited to two in all the simulations here) by defining the charge and mass for each particle species. It is further possible to shrink or expand the initial lattice in the radial or the axial direction to implement different angular momenta and thereby obtain different densities [see Equation (3.16)]. This can be enhanced by giving the ion ensemble different

initial rotation frequencies as well.

6.2.2 Cooling and Heating

6.2.2.1 Cooling Since in the experiment the ions can be cooled to low temperatures, such a mechanism is also provided in the simulation. In order to modify the temperature this quantity needs to be calculated first. Considering the special geometry in Retrap, the magnetic field was set to be parallel to the z-axis and thus, the momentary temperature of the particles $T_{z,m}$ in the z-direction, along the magnetic field, can be expressed with

$$T_{z,m} = \frac{m}{N\,k_B} \sum_{i=1}^{N} v_{z,i}^2 \,, \tag{6.8}$$

where $v_{z,i}$ is the velocity in the z-direction of the i^{th} particle. This temperature can be compared to the desired temperature $T_{z,d}$:

$$\delta = \frac{T_{z,d}}{T_{z,m}} \,. \tag{6.9}$$

The scaling factor δ can be used to rescale the velocities to force the ensemble to the desired temperature at that moment. Note that this is an iterative process and the rescaling needs to be applied many times to ensure the system reaches the desired temperature.

Even though only the axial degree of freedom, parallel to the magnetic field, is cooled, it is observed that the radial temperature decreases to the same temperature, provided the cooling process happens slow enough so the ions have the chance to collide often and exchange kinetic energy. This was checked by measuring the radial temperature $T_{r,m}$. In the calculation of the radial temperature the velocity of each particle has to be corrected with the rigid body rotation angular frequency ω of the whole cloud. This frequency can be obtained with

$$\vec{\omega} = \frac{\vec{L}}{I} = \frac{\sum_{i=1}^{N} m_i\,\vec{r}_i \times \vec{v}_i}{\sum_{i=1}^{N} m_i \vec{r}_i^{\,2}} \tag{6.10}$$

and is used to calculate the velocity component $\vec{v}_{R,i}$ of each particle due to the rigid body rotation of the ensemble:

$$\vec{v}_{R,i} = \vec{\omega} \times \vec{r}_i \ . \tag{6.11}$$

With Equation (6.11) the velocity component in the x-y-plane of each particle v_{xy} can be corrected by a simple vector subtraction and from the resulting velocity the radial temperature according to Equation (6.8) can be calculated:

$$T_{r,m} = \frac{1}{2} \cdot \frac{m}{k_B} \sum_{i=1}^{N} (\vec{v}_{xy} - \vec{v}_{R,i})^2 \ . \tag{6.12}$$

The factor of $\frac{1}{2}$ comes from the fact that the radial motion has two degrees of freedom and has twice as much heat capacity as the axial motion.

The calculation of the radial temperature in the described way assumes that the whole cloud is rotating as a rigid body. If this condition is not fulfilled, the temperature calculation is not correct. However it could be seen that for low temperatures the rigid body rotation is a good assumption.

In the program it can be specified whether the axial degree of freedom should be cooled or the radial degree or both. It is possible to give this option for both ion species separately. This flexibility is not necessary to simulate the real situation in Retrap, but it was helpful in determining whether assumptions about the coupling of the radial and axial motion and the rigid body rotation are valid.

6.2.2.2 Heating In the last section a cooling algorithm was described. To model the cooling of ions in a perfect trap the implementation of such an algorithm would be sufficient. However in a real trap heat sources are present and the achievable temperature depends on the cooling power and on the heating power of these sources.

Knowing the experimental heat sources for the Be^+ case is not so important, since it is possible to directly measure the temperature of this species. For ions which have no transition to use for a temperature measurement the knowledge of the heating rate is crucial to determine the temperature of that particular species. If there are

no heat sources all the ion species would eventually reach the same temperature as the directly cooled Be^+ ions. However if heat sources are present, then the achieved temperature depends on the heating rate and the collisional coupling between the directly cooled ion species and the collisionally cooled species. For a low enough heating power a linear relation between the temperature increase $\Delta T = T_{\mathrm{Xe}} - T_{\mathrm{Be}}$ and the heating power P_H is assumed:

$$P_C = P_H = \frac{\mathrm{d}E_T}{\mathrm{d}t} \approx \alpha \, \Delta T \, . \tag{6.13}$$

To simulate such a situation the code was modified to input a constant heat load acting on one ion species, while keeping the other species at a fixed temperature. This reflects the experimental possibility to measure the temperature of the Be^+ ions, while the separated Xe^{44+} ions are being sympathetically cooled by collisions with the cold Be^+ ions and at the same time heated by undetermined heat sources.

To determine the heating power of all the sources in Retrap it was assumed that the total heating power and cooling power for a pure Be^+ plasma in equilibrium is the same. This was discussed in Chapter (5.3.4) and the heating power was experimentally determined to 1000 $\frac{\mathrm{K}}{\mathrm{particle \cdot s}}$. The implementation of this heat source is done by applying, every 200 time steps, a velocity scaling to the Xe^{44+} ions, which results averaged over time in a constant heat input and raises the temperature of the separated ions. In the next chapter the results of several different runs are summarized.

6.3 Results

A code was developed to run with different number of particles but most of the simulations were done on systems with a total number of 128 particles. The following questions were addressed:

1. Can a cloud of mixed ions be cooled to temperatures below 1 K with the described axial cooling mechanism?

2. Can one species of ions in a mixed cloud be sympathetically cooled by cooling only the axial or radial motion of the other species?

3. Are ordered structures observed for large Coulomb coupling parameters?

4. Is the coupling between the HCIs and the laser cooled Be^+ ions, despite the experimentally present heat sources, strong enough to cool Xe sympathetically to temperatures where it is possible for the Xe to crystallize?

5. Can a separation of ion species with different mass to charge ratios be observed?

In the following, simulations are presented with some answers to these questions.

6.3.1 Cooling

A mixture of 64 $^{136}Xe^{44+}$ and 64 $^{9}Be^{+}$ ions was equilibrated and afterwards cooled to 50 mK by cooling the axial motion of the Be^+ ions. The cooling is done slowly, making sure the cloud equilibrates after energy has been taken out. In Figure (6.1) a part of the cooling process from 50 K to 10 K is shown. It can be observed, that the temperature measured in the radial degree of freedom for the Be ions follows the axial temperature with negligible time delay. If the temperature were dropped quickly, the radial motion might decouple from the axial motion. This is favored if the cloud temperature becomes lower [57]. In the figure this decoupling is observed for Xe, causing the radial temperature of the Xe^{44+} to drop rather slow compared to the other temperatures. Xe^{44+} is expected to crystallize around 10 K. For the Be^+ in the cloud the freezing is expected to happen at about 60 mK and the decoupling of the radial motion from the axial motion was observed at around 30 mK.

The cooling can also be applied directly to the radial motion and the axial temperature drops due to the coupling of the two degrees of freedom. The axial motion of the Be^+ was used to cool the ions in the simulations, since it was observed that the axial motion of the Be^+ ions is coupled rather well to the axial motion of the HCIs and the radial motion of the Be^+ ions. In the experiment, the radial motion of the

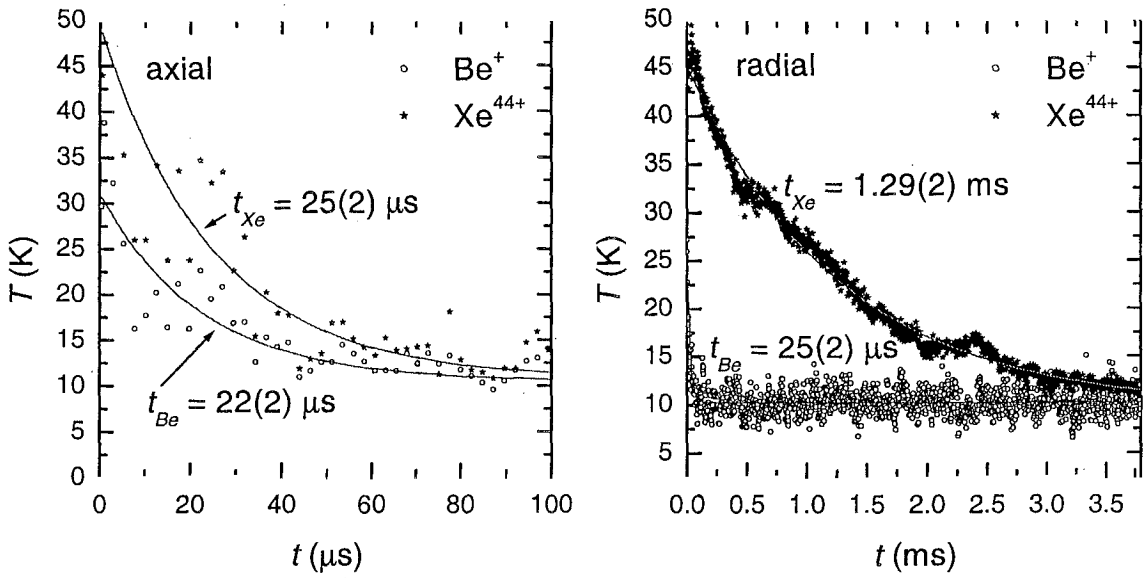

Figure 6.1: Cooling of a simulated, mixed ion cloud consisting of Be^+ and Xe^{44+}. The development of the axial and radial temperatures T over time t is shown, if only the radial motion of the Be ions is cooled. Only the radial temperature of the Xe ions shows a rather slow cool-off. The reason for this might be that the radial motion of Xe is, at 10 K, about to decouple from the axial motion. [57]

Be^+ ions is cooled. However, above 100 mK, the coupling between the radial and the axial motion in Be^+ is rather good and the two cooling mechanisms are equivalent.

The fact that the axial temperature of the Xe ions follows the Be temperature to as low as 50 mK proves that the two ion species are still coupled at low temperatures, despite their centrifugal separation due to the different mass to charge ratio.

6.3.2 Ordering

To evaluate possible ordered structures, the simulation is stopped at various temperatures and the ion positions are analyzed. In Figure (6.2) histograms of the distance of each ion from the trap center for each species is shown as a function of temperature. Since Xe^{44+} is stronger coupled than Be^+ at the same temperature, it already shows a radial structure in the displayed histogram (higher number of particles at 18 μm and 43 μm). Be^+, at 100 K, is still mixed with the Xe ions but the separation becomes

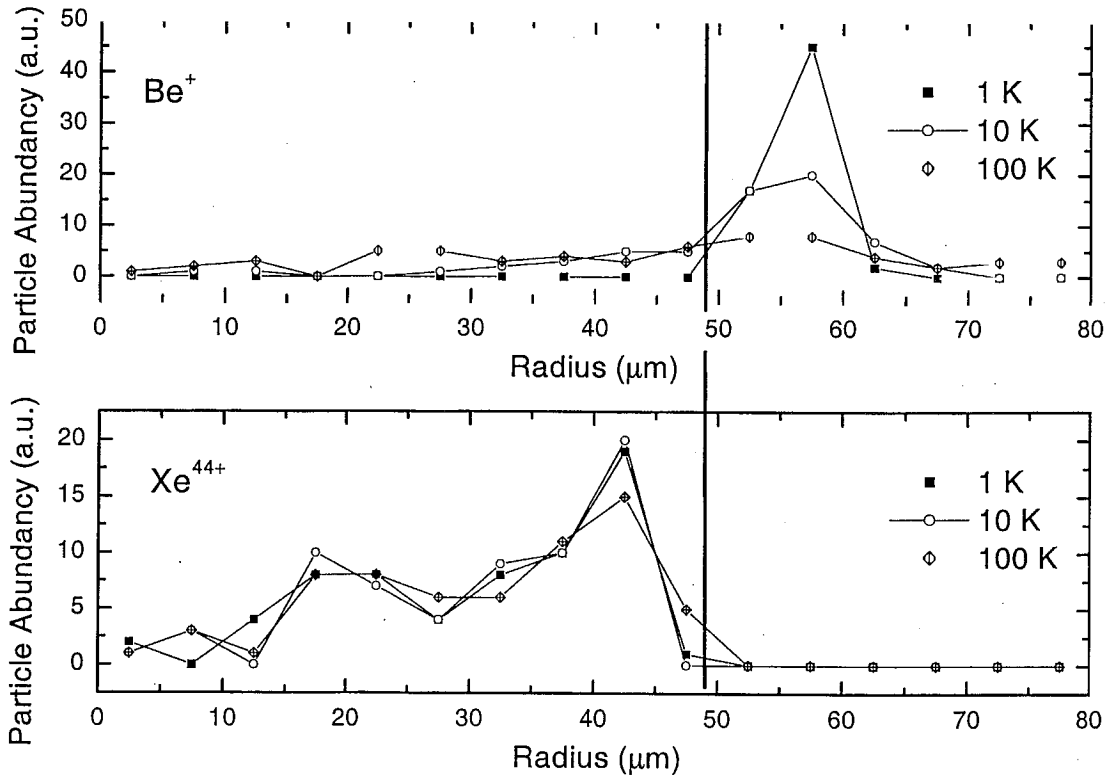

Figure 6.2: Centrifugal separation of a simulated cloud in a Penning trap, consisting of Be^{+} and Xe^{44+}. A histogram of the distance of each ion from the trap center is shown as a function of temperature. As the temperature drops, the separation becomes more distinct. Complete separation can be seen for a temperature of 1 K.

clearer as the temperature drops. At 1 K the separation is complete and the two clouds do not overlap. All the Xe ions are confined in a cylinder-shaped volume with a radius of 50 μm.

A different simulation with a similar cloud is used to display the actual positions of the ions: The x-z-projection (side view) and the x-y-projection (top view) of Xe ions possibly shows an ordered structure. In Figure (6.3) these projections of a 50 K Xe^{44+} cloud are shown but they show no specific ordering. However in Figure (6.4) the cloud is at 10 K and a beginning of layering can be seen in the side view projection and in the top view a concentric structure starts building. In Figure (6.5) the cloud is at 50 mK and the layering can easily be seen, but the concentric structure is still

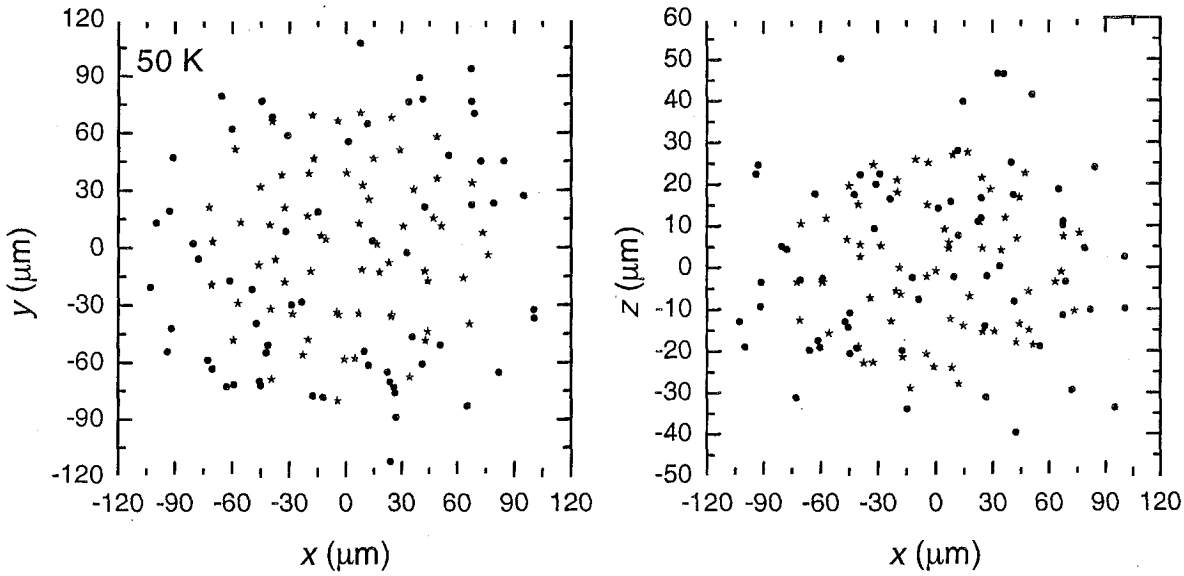

Figure 6.3: Top view (x-y) projection and side view (x-z) projection of a mixed ion cloud consisting of 64 Be^+ (circles) and 64 Xe^{44+} (stars) ions at a temperature of 50 K. No particular structure can be seen.

not very apparent. To make the degree of ordering more apparent, certain groups of ions are marked with a different symbol: ions from the second layer from the bottom and from the top layer are displayed as hollow pentagons and have the same symbols in the side view projection. With this marking it is apparent that the layers are actually circles of different radii at different z-coordinates. The Be ions do not form any specific structure. Their Γ is only in the order of 1. In the Xe cloud a density can be calculated using the dimensions of the cloud and the ion number. In this specific case the density was calculated to be $8.8 \cdot 10^{13} \frac{1}{m^3}$. With such a density Xe^{44+} is expected to crystallize at about 13 K and at 1 K, the Coulomb coupling parameter was $\Gamma = 2300$.

A more distinct ordering is observed if a one component cloud of 128 Xe ions is cooled. The obtained side view and top view projections are shown in Figure (6.6) for a temperature of 1 K. The concentric radial structure is now very pronounced. The cloud is not structured in five layers but only three. The reason for the different

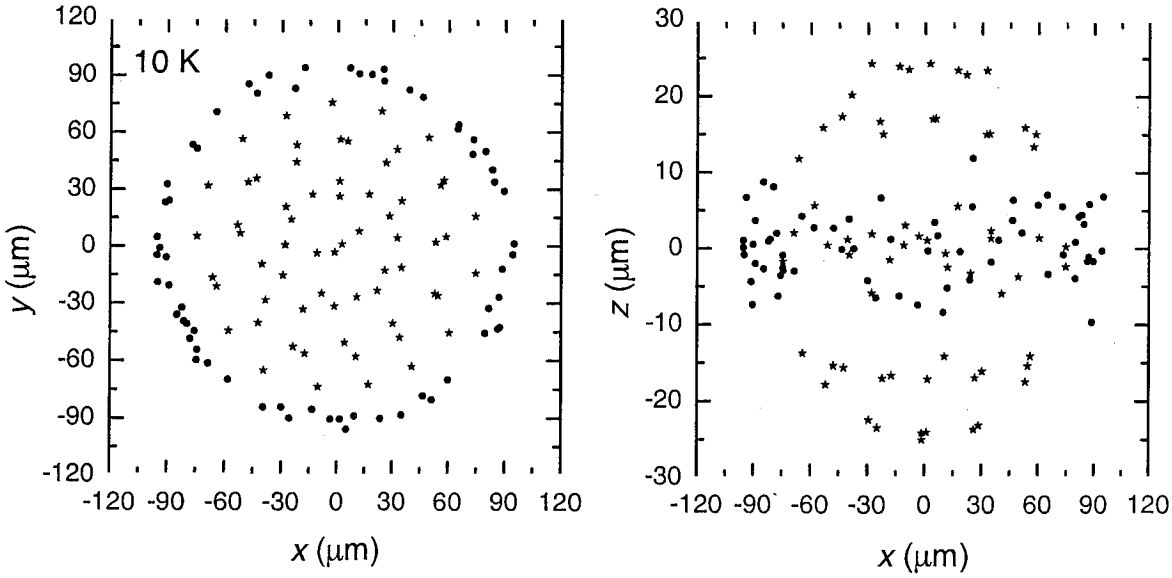

Figure 6.4: Top view (x-y) projection and side view (x-z) projection of a mixed ion cloud consisting of 64 Be^+ (circles) and 64 Xe^{44+} (stars) ions at a temperature of 10 K. The Xe cloud shows a layering in the side view and a slight concentric structure in the top view.

layering is that the trapping conditions are slightly different and the two clouds have different parameters. The density is calculated to be $4.3 \cdot 10^{13} \frac{1}{m^3}$ and the Coulomb coupling parameter derived from that is $\Gamma = 1800$. Due to slightly different trap parameters and different cloud rotation frequencies, the density is by about a factor of 2 smaller than in the first cloud. In this example the degree of ordering is remarkable. The top and the bottom layers are marked with different symbols to indicate, in the top view, the layer in which the ions are. In the top view the ion positions on each of the inner concentric circles are occupied alternatingly by ions from the bottom and top layers.

In Figure (6.7) a higher density cloud at 1.5 K is shown. The density is calculated to $2.5 \cdot 10^{14} \frac{1}{m^3}$ and the Coulomb coupling parameter is $\Gamma = 2200$. The density is about 80% of the maximum Brillouin density for this ion species and this magnetic field. Since the ion cloud is not flat anymore, a structure is not easily seen in the top view. To make it clear that there is radial ordering, the top and side view of only the

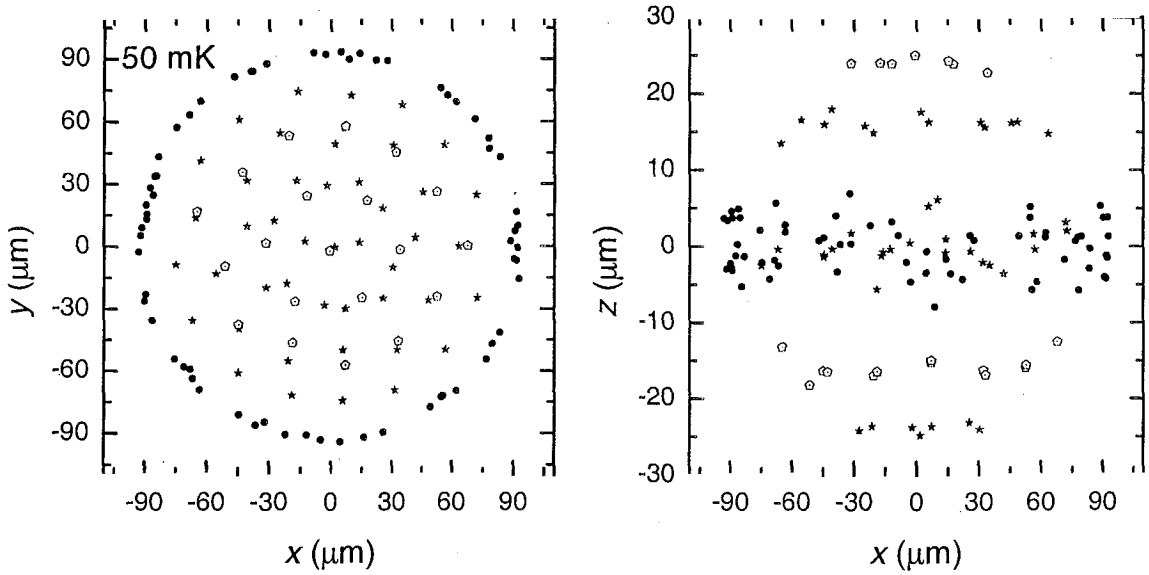

Figure 6.5: Top view (x-y) projection and side view (x-z) projection of a mixed ion cloud consisting of 64 Be^+ (circles) and 64 Xe^{44+} (stars) ions at a temperature of 50 mK. The Xe cloud shows a more distinct layering in the side view. The eye is guided by displaying certain layers of the Xe cloud with different symbols to see the concentric structure in the top view.

center part of the same cloud is shown in Figure (6.8). In the top view the concentric ring structure is now clearly visible.

If temperatures of the Xenon ions of 1 K are achieved in Retrap, such cloud formations can be expected. The rather poor ordering in the mixed cloud example can be understood by taking into account the boundary conditions for the HCIs inside a hollow cylinder formed by the Be ions. The electric potential acting on the Xe ions varies on the boundaries, since there are so few Be ions. If the cloud consisted of more ions a smoother electric potential boundary would result for the Xe ions. In the real experiment there are actually 2–3 orders of magnitude more Be^+ ions in the trap. However, to simulate such systems with the computing power currently available is infeasible, but smooth boundary conditions can be simulated by omitting the Be ions altogether.

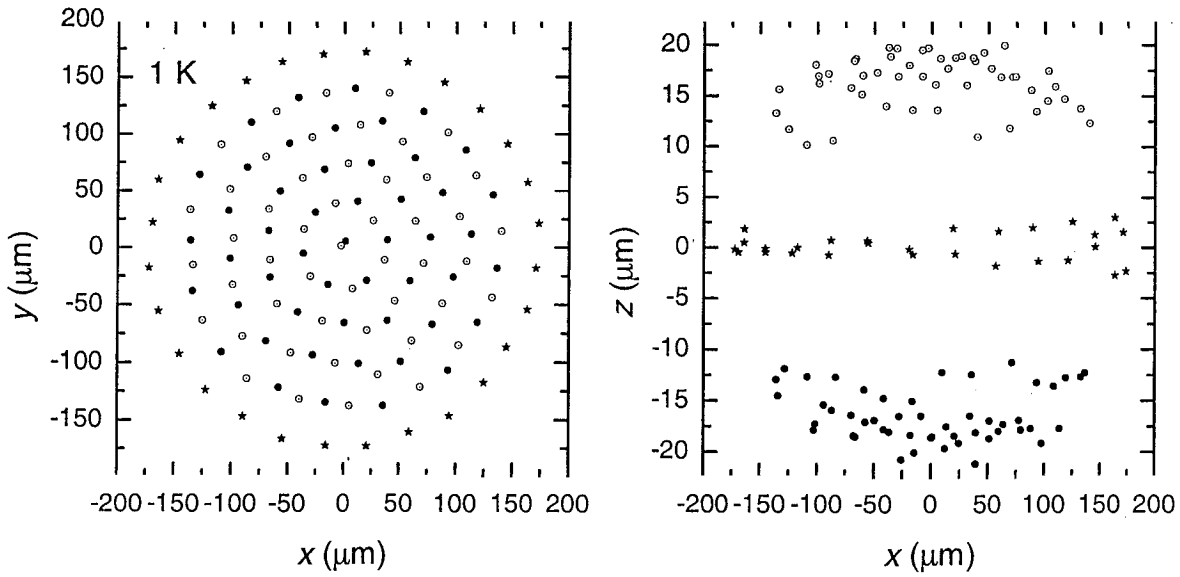

Figure 6.6: Side view (x-z) projection and top view (x-y) projection of an ion cloud consisting of 128 Xe^{44+} ions at a temperature of 1 K. The cloud shows remarkable ordering in both projections. To mark the affiliation of the ions to the different layers different symbols are used.

6.3.3 Background Heating

In the previous simulations a thermally perfectly isolated trap was assumed. In the real experiment however there are heat sources, which could be the thermal noise of power supplies or any electric noise which is broadcasted and not perfectly shielded by the enclosure. In several simulations a heat source was turned on and it's power P_H was varied. The heating acted only on the axial motion of the HCIs while the Be^+ ions were kept at the desired temperature T_B. The Xe temperature will start rising initially and then level off at a temperature T_H, where the heat input from the heat source matches the heat transferred to the Be ions [see Equation (6.13)].

The cloud shown in Figure (6.5) is used as a starting point for simulations. In Figure (6.9) the results of several simulation runs with different heating powers P_H are shown. The Be^+ ions were kept at $T_B = 1$ K and the heating power P_H was varied from 500 $\frac{\text{K}}{\text{particle·s}}$ to $6 \cdot 10^4$ $\frac{\text{K}}{\text{particle·s}}$. In this range a linear dependency of the

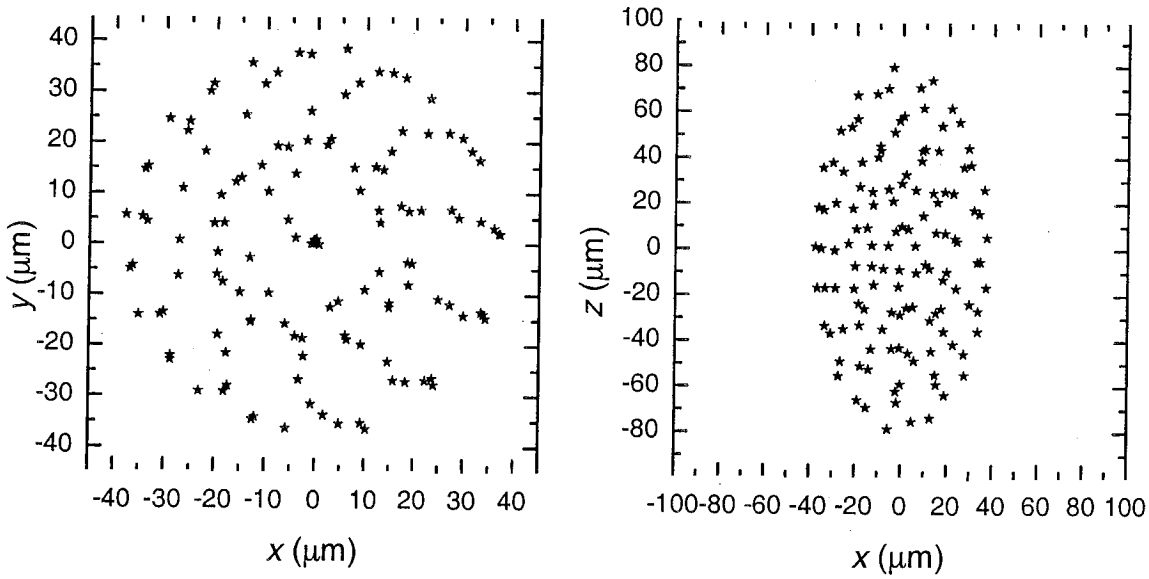

Figure 6.7: Side view (x-z) projection and top view (x-y) projection of an ion cloud consisting of 128 Xe^{44+} ions at a temperature of 1.5 K at a density of $0.7 \cdot n_B$. The higher density of this cloud can be seen from the different aspect ratio of this cloud. Although the coupling parameter is about 3200, a distinct ordering cannot be seen.

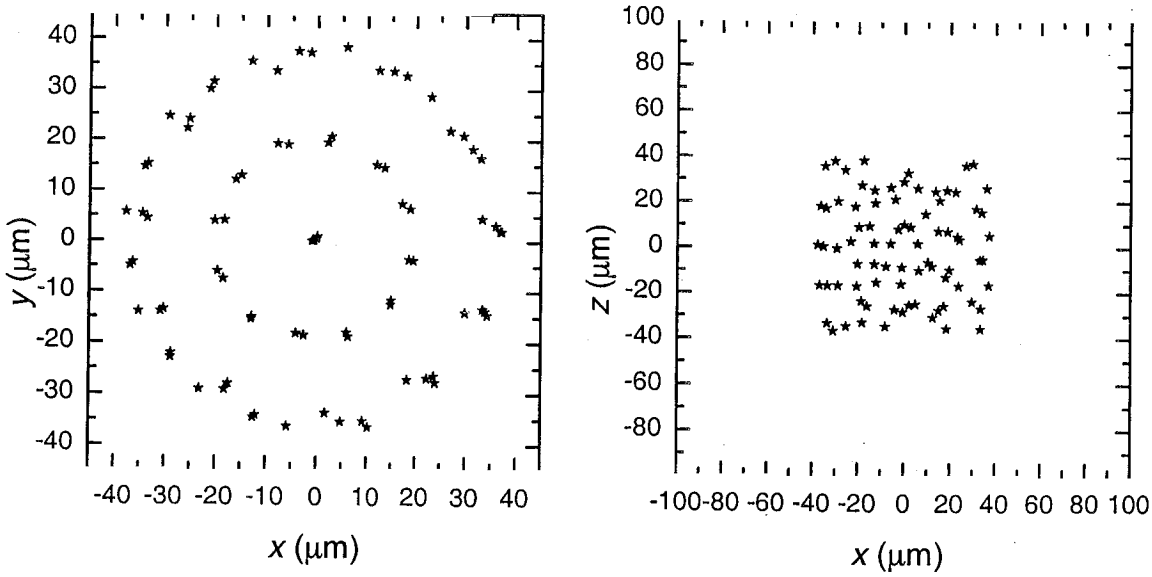

Figure 6.8: Same cloud as in Figure (6.7) is displayed in side and top view projection. Only particles with $|z| < 40\mu$m are shown. The cloud now shows a good radial ordering.

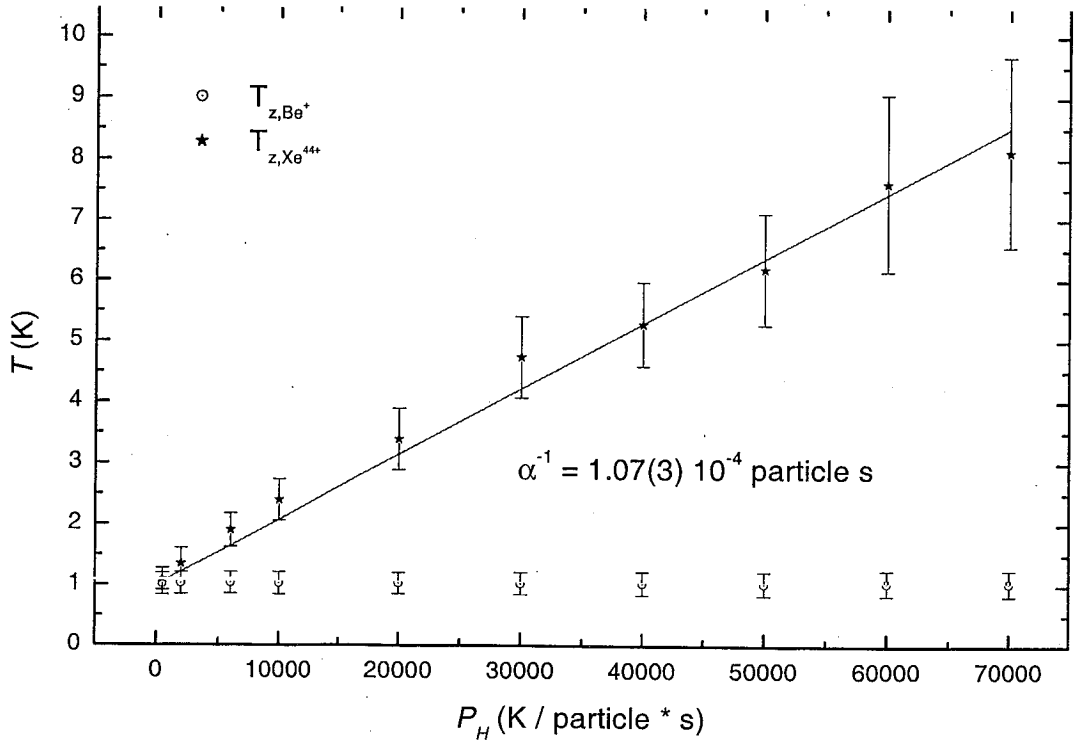

Figure 6.9: Final Xe temperature T as a function of heating power. The axial temperature of the Be^+ ions is kept constant at 1 K and the axial motion of the Xe ions is heated with a constant power P_H. The radial Be temperature is also at 1 K and the radial Xe temperature is at about 8 K. The slope of a linear fit is noted in the graph.

final Xe temperature from the heating power P_H is a good approximation. A slope of $\frac{1}{\alpha} = 1.1 \cdot 10^{-4}\,\text{particle} \cdot \text{s}$ is calculated. From the experiment the heating power is estimated to be about $10^3 \frac{\text{K}}{\text{particle} \cdot \text{s}}$. With this coupling and the experimentally determined heating rate a temperature of 1.11 K is expected for the Xe^{44+} ions.

7 Conclusion

The aim of this work was to show the feasibility of producing highly charged ions in a strongly coupled regime by confining them in a Penning trap and cooling their motion. The benefit of studies with such strongly coupled systems is that mixtures of different ion species can be investigated, while having a very similar mass to charge ratio. This is important since ion species with different mass to charge ratios centrifugally separate at low temperatures in such a trap and mixtures can no longer be studied. An additional advantage is that the temperature of plasmas consisting of ions with higher charge states does not have to be as low as in singly charged ion plasmas. The Coulomb coupling parameter scales with q^2, as seen in Equation (3.1).

In Chapter (5) trap loading techniques were described and experiments showing that two or more species can be trapped in the same trap at the same time were demonstrated. The species were typically Be^+ and Xe^{44+}, however, more Xe and Be charge states were produced due to collisions with the residual gas and also due to not yet understood charge exchange mechanisms. The presence of Be^+ ions enabled a powerful laser cooling technique. Due to the strong coupling to the Be ions, Xe ions could be cooled by collisions with the cold Be^+ plasma.

The temperature of Xe ions could not be measured directly due to a lack of suitable transitions, but Be^+ temperatures were measured to as low as 100(100) mK [Figure (5.29)]. The big error bars on the temperature measurements is due to the relatively unstable conditions of the lasers. In absence of all heating mechanisms, the Xe temperature would eventually reach the same temperature as the Be^+ plasma. However, there are heating mechanisms, like trap imperfections and electro-magnetic radiation, which increases the temperature of the Xe ions until the energy transfer from the heat sources to the Xe matches the energy transfer from the Xe ions to the Be ions.

By measuring the temperature of a one component Be^+ cloud as a function of detuning Δ, and comparing the data to theory an estimate for the cooling power

when the cloud was in equilibrium was possible. Since the cooling power has to match the heating power in equilibrium, an estimate for the heating power was obtained. The heating power was determined to be in the order of $1000\,\frac{\mathrm{K}}{\mathrm{particles}}$.

With this experimentally determined heating power it was possible to determine the equilibrium temperature of the Xe^{44+} ions in a mixture with Be^{+} ions at 1 K. Molecular dynamics simulations were performed where Xe ions were heated with different powers. The analysis of the results revealed that the Xe ions were barely heated, resulting in a temperature of $T_{Xe} = 1.1$ K. This is an insignificant increase and a Xe temperature matching the Be temperature can be assumed in the real experiment.

With temperatures of 1 K and measured densities [see Table (5.2) and Table (5.1)], large Coulomb coupling parameters for Xe ions are obtained. A few examples of calculated Coulomb coupling parameters are given in Table (7.1).

Table 7.1: Achieved Coulomb coupling parameters for Be^{+}, Be^{2+}, and several highly charged ion species in Retrap. The values for the densities n were taken from Table (5.1) (a) and from Table (5.2) (b) and the temperature was assumed to be 1 K.

Source	Ion	n	Γ
		$\frac{1}{\mathrm{m}^3}$	
a	Be^{+},	$1.33(7) \cdot 10^{15}$	2.96(6)
a	Xe^{13+}	$2.00(1) \cdot 10^{14}$	266(1)
a	Xe^{32+}	$3.8(5) \cdot 10^{13}$	925(40)
a	Xe^{44+}	$4.5(3) \cdot 10^{13}$	1850(50)
b	Be^{+}	$1.0(2) \cdot 10^{15}$	2.7(2)
b	Be^{2+}	$2.5(2) \cdot 10^{14}$	6.8(2)
b	Xe^{34+}	$6.4(3) \cdot 10^{12}$	577(9)

It can be seen that Coulomb coupling parameters of more than 200 can be achieved readily by using highly charged ions. The low charge state ions are, despite their higher densities, still in the liquid regime of the strongly coupled plasma. Since the phase transition is expected to happen at around $\Gamma = 172$ the highly charged ions are certainly in the solid regime. However it was not possible to directly detect a crystalline phase of the highly charged ions. To visualize possible structures in the Xe plasma, molecular dynamics simulations were used. The results of such simulations are found in Chapter (6) and ordered structures can be seen.

References

[1] F. M. Penning, Physica **3**, 873 (1936).

[2] H. Dehmelt, Am. J. Phys. **58**, 17 (1989).

[3] R. C. Davidson, *Theory of Nonneutral Plasmas* (Benjamin, Reading, MA, 1974).

[4] J. H. Malmberg and T. M. O'Neil, Phys. Rev. Lett. **39**, 1333 (1977).

[5] W. Neuhauser, M. Hohenstatt, P. E. Toschek, and H. Dehmelt, Phys. Rev. A **22**, 1137 (1980).

[6] D. J. Wineland *et al.*, Phys. Rev. Lett. **59**, 2935 (1987).

[7] F. Diedrich *et al.*, Phys. Rev. Lett. **59**, 2931 (1987).

[8] in *Non-Neutral Plasma Physics III*, edited by J. J. Bollinger, R. L. Spencer, and R. C. Davidson (AIP, Melville, New York, 1999), Vol. 498.

[9] C. F. Driscoll and K. S. Fine, Phys. Fluids B **2**, 1359 (1990).

[10] E. M. Hollmann, F. Anderegg, and C. F. Driscoll, in *Non-Neutral PlasmaPhysics III, AIP CP 498*, edited by J. J. Bollinger, R. L. Spencer, and R. C. Davidson (AIP, Melville, New York, 1999), pp. 223–232.

[11] J. J. Bollinger *et al.*, Phys. Rev. A **48**, 525 (1993).

[12] M. Steck *et al.*, Phys. Rev. Lett. **77**, 3803 (1996).

[13] J. J. Bollinger and D. J. Wineland, Phys. Rev. Lett. **53**, 348 (1984).

[14] X. H. Zheng and J. C. Earnshaw, Phys. Rev. Lett. **75**, 4214 (1995).

[15] J. H. Chu and L. I, Phys. Rev. Lett. **72**, 4009 (1994).

[16] C. A. Murray and D. H. V. Winkle, Phys. Rev. Lett. **58**, 1200 (1987).

[17] B. A. Hammel *et al.*, Phys. Rev. Lett. **70**, 1263 (1993).

[18] D. C. Barnes, T. B. Mitchell, and M. M. Schauer, Phys. Plasmas **4**, 1745 (1997).

[19] ATHENA Collaboration, *Antihydrogen Production and Precision Experiments*, CERN, 1996, SPSLC 96-47/P-302.

[20] ASACUSA Collaboration, *ASACUSA Collaboration Proposal*, CERN, 1997, SPSC 97-19/P-307.

[21] ATRAP Collaboration, *The Production and Study of Cold Antihydrogen*, CERN, 1997, SPSC 97-8/P-306.

[22] M. A. Levine *et al.*, Phys. Scr. **T22**, 157 (1988).

[23] D. H. G. Schneider, J. Steiger, T. Schenkel, and J. R. C. López-Urrutia, in *Physics at the Electron Beam Ion Trap*, Vol. 26 of *Atoms and Plasmas* (Springer-Verlag, Berlin, Heidelberg, New York, 1999), Chap. 2, pp. 30–59.

[24] E. D. Donets, Nucl. Instr. and Meth. in Phys. Res. B **B9**, 522 (1985).

[25] M. B. Schneider *et al.*, in *Proceedings of the International Symposium on Electron Beam Ion Sources and Their Applications*, edited by A. Hershcovitch (AIP Press, New York, 1989), p. 158.

[26] D. Schneider *et al.*, Phys. Rev. A **44**, 3119 (1991).

[27] T. Schenkel, A. V. Hamza, A. V. Barnes, and D. H. Schneider, Progress in Surface Science **61**, 23 (1999).

[28] B. R. Beck *et al.*, Phys. Rev. Lett. **77**, 1735 (1996).

[29] J. Steiger *et al.*, Phys. Rev. A .

[30] G. Weinberg *et al.*, Phys. Rev. A .

[31] D. Vogel, Technical Report No. UCRL-ID-104990, Lawrence Livermore National Laboratory, Livermore, CA (unpublished).

[32] I. G. Brown, J. E. Galvin, B. F. Gavin, and R. A. MacGill, Rev. Sci. Instrum. **57**, 1069 (1987).

[33] B. Wolf, in *Handbook of Ion Sources* (CRC Press, Boca Raton, New York, London Tokyo, 1995), Chap. 2.

[34] S. R. Elliott and R. E. Marrs, Nucl. Instr. and Meth. in Phys. Res. B **V100**, 529 (1995).

[35] R. E. Marrs, D. H. Schneider, and J. W. McDonald, Rev. Sci. Instrum. **69**, 204 (1998).

[36] J. Steiger *et al.*, Annual Report UCRL-ID-132345, Lawrence Livermore National Laboratory (unpublished).

[37] H. C. Corben and P. Stehle, *Classical Mechanics*, 2^{nd} ed. (John Wiley and Sons, New York, 1975).

[38] M. Born, *Vorlesungen über Atommechanik* (Julius Springer, Berlin, 1925), reprinted by Springer-Verlag 1976.

[39] L. S. Brown and G. Gabrielse, Rev. Mod. Phys. **58**, 233 (1986).

[40] J. J. Bollinger, D. J. Wineland, W. M. Itano, and J. S. Wells, in *Laser Spectroscopy VI*, edited by H. Weber and W. Luthy (Springer-Verlag, Berlin, Heidelberg, New York, 1983), pp. 168–172.

[41] T. M. O'Neil, Physics Today 24 (1999).

[42] M. H. *et al.*, Astrophys. J. **434**, 624 (1994).

[43] M. Nantel *et al.*, Phys. Rev. Lett. **80**, 4442 (1998).

[44] A. N. Mostovych, K. J. Kearney, J. A. Stamper, and A. J. Schmitt, Phys. Rev. Lett. **66**, 612 (1991).

[45] G. R. Bennett *et al.*, Phys. Rev. E **50**, 3935 (1994).

[46] S. Pfalzner and P. Gibbon, Phys. Rev. E **57**, 4698 (1998).

[47] C. Murray and R. Wenk, in *Strongly Coupled Plasma Physics*, edited by H. M. Van Horn and S. Ichimaru (University of Rochester Press, Rochester, NY, 1993), pp. 367–376.

[48] A. Homann, A. Melzer, and A. Piel, Physikalische Blätter **52**, 1227 (1996).

[49] R. C. Davidson, *Physics of Noneutral Plasmas*, *Frontiers in Physics* (Addison-Wesley Publishing Company, Redwood City, CA, 1990).

[50] T. M. O'Neil, Phys. Fluids **24**, 1447 (1981).

[51] D. Dubin and T. O'Neil, Rev. Mod. Phys. **71**, 87 (1999).

[52] D. J. Larson *et al.*, Phys. Rev. Lett. **57**, 70 (1986).

[53] H. Imajo *et al.*, Phys. Rev. A **55**, 1276 (1997).

[54] M. Winter, WebElements2000, *The Periodic Table On The WWW*, 1999, http://www.webelements.com.

[55] W. M. Itano and D. Wineland, Phys. Rev. A **25**, 35 (1982).

[56] D. J. Wineland, W. M. Itano, J. C. Bergquist, and R. G. Hulet, Phys. Rev. A **36**, 2220 (1987).

[57] T. M. O'Neil and P. G. Hjorth, Phys. Fluids **28**, 3241 (1985).

[58] L. Spitzer Jr., *Physics of Fully Ionized Gases*, 2^{nd} rev. ed. (Interscience Publishers, New York, London, 1962).

[59] S. Chandrasekhar, in *Priciples of Stellar Dynamics* (University of Chicago Press, Chicago, 1942), Chap. 2 and Section 5.6.

[60] S. Chandrasekhar, Astrophys. J. **97**, 255 (1943).

[61] C. Ruehlicke, Ph.D. thesis, Universität Bielefeld, 1998.

[62] M. Kretzschmar, Z. Naturforsch. **45A**, 965 (1990).

[63] J. W. McDonald, D. Schneider, M. Clark, and D. Dewitt, Phys. Rev. Lett. **68**, 2297 (1992).

[64] F. Aumayr *et al.*, Phys. Rev. Lett. **71**, 1943 (1993).

[65] H. Kurz *et al.*, Phys. Rev. A **49**, 4693 (1994).

[66] J. W. McDonald, Ph.D. thesis, Western Michigan University, Kalamazoo, MI, 1998.

[67] T. Baba and I. Waki, in *Quantum Coherence and Decoherence*, edited by K. Fujikawa and Y. Ono (Elsevier Science B.V., Amsterdam, Netherlands, 1996), pp. 53–56.

[68] E. Salzborn, priv. comm., 1999.

[69] L. R. Brewer *et al.*, Phys. Rev. A **38**, 859 (1988).

[70] S. A. Prasad and T. M. O'Neil, Phys. Fluids **22**, 278 (1979).

Acknowledgments

During the time I was doing the research at the Lawrence Livermore National Laboratory (LLNL) I had the possibility to meet many kind, smart and interesting people. The wonderful experience of going to a foreign country and getting to know a different culture and language was particularly enriched by these individuals. Therefore I would like to thank all of the people who contributed to my personal and professional education during this time.

Particularly, I would like to thank Prof. Dr. Helmut Jäger, who made it possible for me to start this project, by agreeing to supervise my research from a distant location. His trust and support helped me to tackle many problems in science as well as in dealing with the university bureaucracy. Thanks to him and Theo Neger, who found the time to give me a chance to get the necessary academic credentials, I qualify for the final thesis defense. I would also like to thank Prof. Dr. Ferdinand Schürrer for agreeing to be my *Zweitprüfer*.

The first months in this country were the hardest, and I would like to thank Klaus Widmann and his wife Evelyn for hosting me and introducing me to many different aspects of living in, and enjoying, the United States. I particularly owe Klaus my gratitude, since his effort in creating a LaTeX style saved me many days of work and preserved a lot of my hair.

At the beginning of my assignment at LLNL I was overwhelmed with the complexity of the experimental apparatus with which I was confronted. But the constant effort of Bret Beck and Joachim Steiger to explain the same things over and over to me, enabled me to understand and use the system to the point where I could actually lead the experiment myself. Their help did not stop when they left the group. They kept supporting me with valuable suggestions, proof reading papers and even running computer simulations. Without their help, this work would not have been possible in this form. Joe Holder, who joined the group later, was an indispensable coworker.

Without him, the running of the beam times would not have been possible. I am thankful to him for the many long days and nights he assisted me with his extensive knowledge, patience, and work ethic. Joe also played a key role in running the molecular dynamics simulations. I am grateful to Hugh DeWitt, who not only expanded my knowledge about stellar plasmas, their past and their future, but could also tell interesting and entertaining stories about his revolutionary professional past. Many thanks to Joe McDonald and Dieter Schneider, who were always, and at any time, accessible to tune EBIT to its peak performance and provided us on the side with the latest jokes. Thanks to Jack Glassman for his never ending patience in tuning the dye lasers. In the daily operations of an experiment of this size, one soon realizes that without the proper technical staff an experiment is destined to fail. I had the opportunity to work with excellent people like Dan Nelson, Phil Dantonio and Ed Magee and I would like to thank them for their patience with my all too often urgent requests. I would also like to thank Ken Visbeck and Jeff van Lue for their help.

The excellent environment in this large group was created by many people. Vince Decaux was never shy to comment on anything and he thereby kept all of us entertained. His arguments with José Ramon Crespo, who used his never ending energy resources to build new devices as well as to debate endlessly, were unforgettable. I would like to thank Christiane Rühlicke and Greg Brown for the wonderful time we shared a house together. My office mates, Alan Barnes and Steve Utter, I thank for their company and many educational discussions. Such discussions, either physics-related or otherwise, with the people at EBIT like George Weinberg, Peter Seelig, Mike Newman, Thomas Schenkel, Mirko Hattass, Guillaume Machicoane, Thomas Niedermaier and Alexis Schach von Wittenau made the laboratory life between stainless steel, electronics racks, vacuum pumps, and nuts and bolts much more colorful and rewarding.

Thanks also to Ross Marrs, who I had the honor to work with for a brief period of time and Peter Beiersdorfer, who always found the time to consult me about physics-

related as well as physics-unrelated topics. I would like to credit the cooperation of the surface group, especially Alex Hamza, who shared their time on the experiment with us. I also would like to express my gratitude to David Church, who taught me a special lesson about trust.

During my years at LLNL the EBIT group was supported by a plethora of professional administrative people. These included Jo Ann Harris, Emma Harris, Kellie Vincent, Nancy Kliment, Darlene Klein, Ileana Dobie, and especially Diane Rae, Linda Allen, Candace Lewis, and Donna Vercelli. These women worked hard to make things run smoothly and also created an entertaining and delightful atmosphere within the lab. Special thanks to Nancy Fleshman who maneuvered me through the most arduous and complicated paths of the INS. And again I have to praise Dieter Schneider who, as a group leader, kept the spirit high and led the program to success. I particularly appreciate his trust and encouragement, which motivated all of us to give our best.

In the final stage of this work I naturally had more contact with the University in order to comply with all the rules for completing my dissertation. This is an awkward task since there is a 6000 mile geographic distance and a 9 hour time difference between the University offices and my office. Luckily, I could count on Jürgen Flieser, who was always willing to help me in every aspect of dealing with the officials at the University. Jürgen played a crucial role in the final steps of this project. I thank him very much for his time, patience, effort and friendship.

I would like to express my gratitude to my parents who always supported me morally and at times even financially in my decision to tackle this academic hurdle. And last, but certainly not least I would like to thank my soon-to-be-wife, Anne, for putting up with all the missed time with her and for being with me through all the hard times. Her encouraging attitude helped me to get to where I am now.

Lukas Gruber Livermore, March 31st 2000